Electronic properties of zinc oxide and related materials grown by molecular-beam epitaxy

Maddison Coke

A thesis presented for the degree of

Doctor of Philosophy

Department of Electronic and Electrical Engineering

University College London

UK

2016

I, Maddison Coke, confirm that the work presented here in this thesis is my own. Where information has been derived from other sources I can confirm that this has been indicated in the thesis

Acknowledgements

No person is an island, and this is never more true when embarking on a PhD for over 4 years. My friends and colleagues both inside and outside UCL have been integral in me accomplishing this work. First and foremost, I would like to acknowledge my supervisor, Professor Paul Warburton. He has always been an open supervisor, enabling much independent research and problem solving along the way while still being an invaluable source of knowledge and guidance. He has helped me establish myself as a scientist but also allow my independence flourish both in my studies and my public engagement activities that have run happily along side them.

There are many colleagues I have had the pleasure to work with at my time in UCL, but those whom have worked in the MBE lab will always be the ones whom have seen me at my best and worst, and together we have managed to keep the MBE system working. There are many days we have spent in the lab venting and problem solving the latest issue with our system, affectionately called "Martha". Of these James Sagar has supported me above and beyond I could possibly hope for from any post doc, his support came from both our friendship and mutual respect. He helped me believe not only in my work but myself. His departure from the office and lab left a large gap, but even now he has helped me with with public engagement activities and the numerous drafts of this thesis. The new addition to the lab while I was a PhD came in the form of Oscar Kennedy. A source of humor and daily catch ups, he never dismissed any of my new ideas for growth and was always a source of new ideas himself. His knack for coding has inspired me to learn myself and to never stop learning. Our special language for describing the MBE I know will live on. I would also like to thank Dr Marina Panfilova, for my swift introduction to MBE back when I had just started out on this adventure, James Aldous for bringing music to the lab and his huge wealth of knowledge and Ivan Isakov for his unusual humor he brought to the lab as well as his breadth of knowledge in all things.

I would like to thank my colleagues and friends, with whom I shared desks, labs, clean room suits but more importantly also houses, conferences, parties and fields: Dr Nick Constantino, Nuno Braz, Dr Chris Nash, Tim Wootton, Dr Jon Fenton, Dr Johnathan Burnett,

Marie-Laure Hicks and Daniel Payne. I would like to thank Dr Ed Romans, whose intelligence and thought was always prevalent in discussions but will mainly remember him for loitering around Paul's office and handing out free chocolate which very much helps when writing up a thesis.

I am thankful to all the people and collaborators that helped me with experiments: Steve Etienne, Mike Creswell, Vijayalakshmi Krishnan and Suguo Huo from LCN clean-room as well as Dr Steve Firth, Steve Hudziak and Dr Richard Thorogate from UCL.

Life doing a PhD is not all about work and I have had many people who have kept me going outside the lab; with motivation talks (and drinks) as well as long chats about how much of a challenge working with Martha is. Caroline Candy has been a housemate and dear friend whom has put up with much moaning over the years but has always stuck by me, and Sheena Cowell who has told me many tales of her own PhD experience to keep me going in the rougher patches.

Finally I would like to thank my parents. They have never stopped believing in me, or supporting me through my many years of pursuing a scientific career. They have loved and encouraged me throughout and for that I will always be forever grateful, and to my girlfriend Stacey, who has had to put up with me at my most despairing moments but has always put a smile on my face and kept me going, cooked wonderful food and reminded me that there's more to life than science.

For you all;

Thank you.

Abstract

Thin film heterostructures have been at the heart of advances in electronics. The use of material interfaces with confined electron spaces is one of the key areas of research in thin film deposition

An example of such a thin film system is ZnMgO/ZnO where confined electron spaces occur at the interface between these two materials. The nature of the electron confinement depends upon the nature of the interface. Abrupt interfaces between ZnMgO and ZnO are strained due to lattice mismatch. This strain is relaxed if there is a gradual incorporation of Mg during growth, resulting in a diffuse interface. This strain relaxation is however accompanied by reduced confinement and enhanced Mg-ion scattering of the confined electrons at the interface. Here we experimentally study the electronic transport properties of the diffuse heteroepitaxial interface between single-crystal ZnO and ZnMgO films grown by molecular-beam epitaxy (MBE). The spatial extent of the interface region is controlled during growth by varying the zinc flux. We show that, as the spatial extent of the graded interface is reduced, the enhancement of electron mobility due to electron confinement more than compensates for any suppression of mobility due to increased strain.

In order to better understand the relationship between the material composition of the interface and the electronic properties of the confined electron space, variations in gradient of Mg are investigated. We use the angular dependence of the magnetoresistance to confirm the two dimensional nature of the space. We also looked at the electron scattering times and the associated effective mass. Both classical and quantum scattering times are consistent with the dominating effect being alloy scattering.

Zn/ZnO/Zn heterostructures are a system of interest for application as Josephson junctions. We present initial studies into the superconductivity of MBE deposited zinc and subsequent morphological studies.

Contents

List of Figures

Chapter 1

Introduction

"Things don't have to change the world to be important." Steve Jobs, 1996

1.1 Background

The discovery of the two-dimensional electron gas (2DEG) and its applications have shaped the scientific environment we work in: from when it was first discovered in Bell Laboratories in 1979 [1] to having now become an integral part of many semiconductor electronic devices, most notably through the widespread use of the high electron mobility transistor (HEMT). With transistors providing the building block for all computational logic, it is easy to see the implications of changing the properties of these components. Compared to traditional Si transistors, the HEMT provide components which have a high gain allowing for use as amplifiers; low noise due to low variation in the current and high switching speeds due to low concentrations of minority carriers. With this being the case HEMTs are much better suited to modern day applications such high efficiency power amplifiers for 4G/5G [2].

Aside from large implications of the applications of the 2DEG, it has also been a gateway to a variety of interesting physics. Most notably there have been two Nobel Prizes awarded for work done on the phenomenon discovered in 2DEGs; Klaus von Klitzing in 1985, "for the discovery of the quantized Hall effect" [3] and Robert B. Laughlin, Horst L. Strmer and Daniel C. Tsui in 1998, "for their discovery of a new form of quantum fluid with fractionally

charged excitations" [4]. The functionality of the HEMT comes from the high mobility of electrons at the interface. This vastly exceeds those in the undoped semiconductor with mobilities as high as 3 x 10^7 $cm^2V^{-1}s^{-1}$ [5].

2DEGs achieve such high mobilities due to the ease of charge carrier transfer. Carriers are introduced to the semiconductor by ionised dopants which act as scattering centres and decrease the mobility of the semiconductor. By confining electrons to a two dimensional plane away from dopants, the electrons see fewer ionised donors and therefore do not experience the associated scattering and drop in mobility.

Optimizing the properties of the 2DEG and understanding its fundamental properties is key to future applications, both fundamental and technological. The early work on 2DEGs, and indeed a lot of current work, is based on AlGaAs/GaAs modulation doped heterostructures. This has provided a fundamental study of the 2DEG system but many new material systems which have fundamentally different properties, have also demonstrated 2DEGs such as AlGaN/GaN, lanthanum aluminate ($LaAlO_3$)/ strontium titanate ($SrTiO_3$) (LAO/STO) and ZnO/ZnMgO.

Whilst AlGaAs/GaAs remains the benchmark 2DEG to which all others are compared, these new families of 2DEGs are starting to compete with AlGaAs/GaAs in terms of mobility, notably with the ZnO based 2DEG now achieving 1 x 10^6 cm^2 $V^{-1}s^{-1}$ [6], new quantum phenomena such as odd denominator fractional quantum Hall states being observed [7] and new device fabrication possibilities, such as device geometries being written by an AFM tip [8].

From these possible new materials, ZnO is a material with a large range of possibilities, whose properties will be discussed in the next section. These new properties could allow topological quantum computing and spintronic applications owing to its low spin orbit coupling, which allows for long spin coherence times [9].

Despite the rapid emergence of very high mobility 2DEGs based on ZnO, there is little work understanding some of the limitations which may present themselves in devices based on this 2DEG. Firstly, all of the record breaking mobility films are grown on Tokyo Denpa substrates which are no longer available. Tokyo Denpa substrates were seen to have the lowest

levels of impurities incorporated during hydrothermal growth due to their seeding process. Other commercially grown bulk ZnO substrates are available but these have been seen to not be of the same standard. Another area where there has been seen to be some ambiguity is concerning the concentration profiles of the dopants in the films. Concentration profiles for these films are also not always presented and are in fact known to show a graded system. There is little understanding of how the gradient of doping incorporation affects these physical properties. The effect of impurities in these less-pure substrates and the nature of interfaces are both important to understand in order to optimize future 2DEGs for all the interesting applications mentioned above. These are both topics I will address in this dissertation.

In order to grow ZnMgO by MBE (molecular beam epitaxy), and therefore the 2DEGs as described above, it is necessary to have an elemental Zn source in the MBE chamber. Zn is a low temperature superconductor, so there is also the possibility to grow trilayer Josephson junctions. A relevant comparison for a Zn/ZnO/Zn junction is the well-established shadow-evaporated Al/AlO_x/Al junction. These are formed by oxidizing the surface of an aluminum film and evaporating another layer of aluminum on top of it to form an Al/AlO_x/Al stack. The random oxidation of the Al can introduce two level systems (TLS) into the device which can limit the low-power low-temperature operation of quantum circuits based upon such junctions [10]. Additionally the insulating barrier of AlO_x leads to low values of the critical current densities in such junctions.

A Zn/ZnO/Zn junction with an epitaxially grown layer of ZnO and high elemental purity Zn could overcome some of these issues. The highly crystalline epitaxial ZnO could be grown to introduce fewer TLS whilst the semiconducting ZnO barrier may allow for higher critical currents.

1.2 Materials

As previously mentioned, ZnO/ZnMgO thin films are a new material system that has been used to observe 2DEG properties. This work is structured around ZnO and its associated materials focusing on ZnO/ZnMgO interfaces for the formation of a 2DEG but also

on Zn/ZnO/Zn junctions for the formation of Josephson junctions.

If we first consider the undoped semiconductor ZnO, a wide bandgap semiconductor, which renders it transparent to visible light. Consequently transistors with a ZnO component do not degrade after exposure to light in the way that transistors of other material systems are prone to. Since ZnO is a transparent semiconductor with optoelectronic, piezoelectric and conceivably spintronic applications, possible device applications are plentiful, especially when integrated with a 2DEG electronic system. It has a wide direct band gap (3.37 eV at room temperature) and a high exciton binding energy (67 meV) [11], which is three times larger than that of GaN. Another benefit of ZnO is that both zinc and oxygen are earth abundant materials and are non-toxic.

There is also the possibility of tailoring electronic, magnetic and optical properties via alloying, doping, forming hetero-structures and quantum wells, and nano-engineering [12]. Tailoring of this type is required to make a number of important devices such as laser diodes [13], solar detectors [14], spintronic devices [15] and, most importantly, thin film field effect transistors for use in transparent electronics [16].

The band gap of ZnO can be tuned by the incorporation of a ternary element. Three elements are predominately used for this kind of band-gap tailoring; Mg, V and Cd. Adding V or Mg broadens the band gap, while the addition of Cd narrows it [17]. An advantage of using Mg is that it has an ionic radius similar to that of Zn (Mg $^{2+}$ being 72 pm and Zn $^{2+}$ being 74 pm), so minimal strain at the interface is induced [18]. In contrast band-gap tailoring in III/V semiconductors often requires the use of elements, which are both toxic and rare in comparison with Mg, and have larger associated lattice mismatches with the lower band-gap material.

There are some important advantages with regards to commercial production of ZnO compared to other semiconductors with similar properties. Monocrystalline ZnO substrates are readily available with wafers having a diameter of up to 50 mm. Moreover, because of the differences in wafer growth processes, it is believed that the wafer production of ZnO will increase faster than that of GaN and other potential candidates, especially for UV applications [19]. The most common substrate for heteroepitaxy is sapphire, despite its large lattice

mismatch with ZnO (17%), due to its reproducibility, purity and cost. Although this work makes use of ZnO substrates, this does give possibilities for future scale-up work. ZnO can be deposited at low temperatures (below 1000 °C) with molecular beam epitaxy [20], RF sputtering [21], chemical vapor deposition (CVD) [22] and pulsed laser deposition (PLD) [23]. The ionic nature of ZnO makes it possible to use both wet and dry etching in the device fabrication process [24] .

1.3 Structure of the thesis

The experimental work presented in this thesis is broken down into two main growths in the molecular beam epitaxy chamber: ZnMgO on ZnO, and Zn/ZnO/Zn trilayers.

Chapter 2 provides the scientific background and current literature for the growth of confined electronic spaces, with focus on the ZnMgO/ZnO interface. Chapter 3 concentrates on the background of current low temperature superconducting Josephson junctions.

Chapter 4 gives an account of the methods used in this work: experimental techniques for both the growth and electronic measurements.

The experimental results and analysis are presented in chapters 5 to 7.

Chapter 5 describes the initial ZnMgO growth on ZnO, with a focus on the substrate preparation and its importance, as well as the parameter space used to define the growth of the ZnMgO. Growth parameters including temperature, Mg flux and zinc flux are included.

Chapter 6 looks at films grown with variations of zinc flux which create a graded ZnMgO and focuses on the low temperature electronic measurements. It then focuses on the derived characteristics of the confined spaces such as effective mass and various scattering times.

Chapter 7 briefly describes our attempts at creating a Zn/ZnO/Zn Josephson junction with the optimization of the zinc superconducting layer under, ZnO growth and device fabrication.

The final chapter, Chapter 8, summarizes the work, presents conclusions and outlines future work that is needed for the development of the interfaces studied in the present work, and for the continuation of the Zn/ZnO/Zn work to electronic measurements.

Chapter 2

Theory of Confined Electron Spaces

Confined electron spaces such as 2DEGs and three dimensional electron slabs (3DESs) vary significantly from their bulk counterparts. In bulk materials the carrier transport is through the whole of the bulk material. In order to create confined electron spaces in planar semiconductors it is necessary to create thin films with high purity and low defect levels. Crystalline thin films can have many improved properties compared to polycrystalline films or bulk material due to improved crystalline quality and purity. These films and other such nanostructures have only been realized due to improvements in deposition techniques [25]. These advantages have allowed devices to have longer lifetimes and better overall performance. These improvements along with the use of the confined electron space allows for better overall devices.

Confined electron spaces are realized by controlling the conduction band in a semiconductor. Through the use of band gap engineering it is possible to influence the position of electrons. By forming heterostructures, where two or more different materials are grown on top of each other, the bands of the material can be controlled resulting in regions where electrons accumulate and quantum wells are observed. By creating a quantum well the transport is quantized, and increased mobilities are seen. There are many such systems where this can be observed, a selection of which will be examined in this chapter. The initial discovery of the 2DEG in Si metal-oxide-semiconductor (MOS) systems is looked at first, followed by GaAlAs/GaAs systems, where by carefully controlling the doping the confinement can be controlled. Finally we consider at ZnO/ZnMgO interfaces which are the focus of this

dissertation and the 3DES which can be formed in polar materials.

2.1 Discovery and Development of Confined Electron Spaces

The discovery of the 2DEG and its further optimization as well as development has stemmed from its use in field effect transistors (FET). The formation of a 2DEG is integral to the workings of the FET. Controlling and confining the conduction path with electric fields, conduction can be, in effect, turned on or off depending on the applied stimulus. In both extrinsic 2DEGs (those observed only under an external electric field) and intrinsic 2DEGs (those formed by an internal electric field across the interface), the reduced dimensions can lead to increased mobilities due to the 2D density of states (DOS). New quantum phenomena may also be observed. Each new material discussed has its own internal properties which lead to different phenomena which will be discussed in turn, from the first identification of 2DEG in Si MOS to oxides where the primary material system of this dissertation (ZnMgO/ZnO) will be discussed.

2.1.1 Extrinsic Two Dimensional Electron Gases

The formation of the 2DEG in the Si MOSFET (metal-oxide-semiconductor FET) was first observed with p-type Si as the three dimensional semiconductor, SiO_2 as the insulator and a metal top gate. Its band structure with no external field is shown in figure 2.1 (a). Si, with a diamond-like configuration, acts as an insulator at room temperature, with p or n type doping required for semiconductor characteristics. The p-type Si used in the MOSFET gives rise to hole carriers in the valence band.

The functionality of the Si MOSFET comes from the application of a gate voltage as seen in figure 2.1 (b). An applied gate voltage bends the conduction band down below the Fermi energy in the Si located below the gate contact, creating a 2D region with electrons present. A deeper explanation of the formation of the 2DEG is given later with respect to intrinsic 2DEGs. The great advantage of the Si MOSFET is that the density of charge carriers is tunable with the application of the gate voltage. However due to the nature of the negative

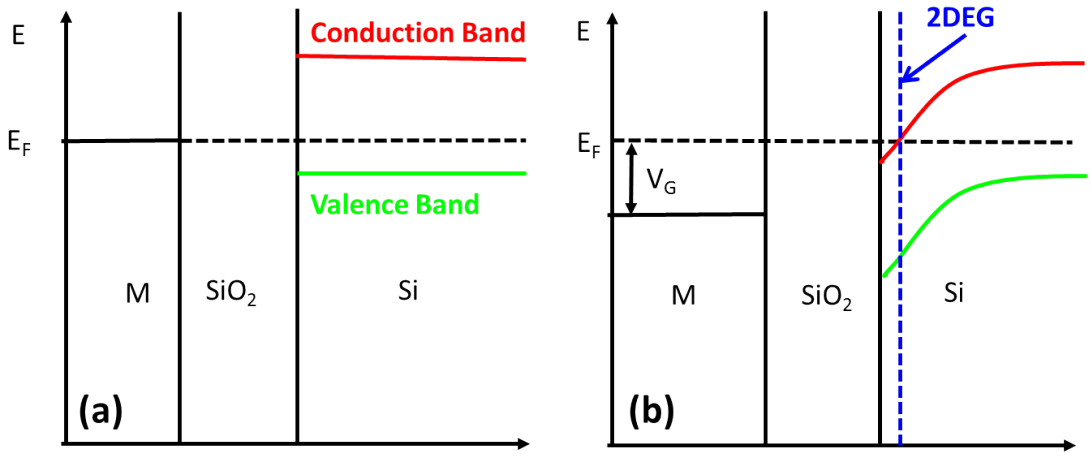

Figure 2.1: The energy levels of a Si MOS under (a) no gate potential and (b) a positive gate potential and the subsequent formation of the inversion layer. The conduction band is given in red and the valence band in green in both cases.

charge accumulation in the depletion layer there is a high degree of scattering within this layer. This scattering means that the observation of the 2DEG at low carrier concentrations is hindered.

2.1.2 Intrinsic Two Dimensional Electron Gases

The formation of the intrinsic 2DEG varies from that of the extrinsic 2DEG as its formation is dictated at the point of growth and originates from the difference in band gaps at the interface of two materials. One problem with semiconducting thin films is that to have a large number of charge carriers requires large amounts of doping. This doping increases the scattering from the ionized dopants and subsequent defects associated with them. This increase in scattering reduces the mobility. One solution is to confine the electrons to an undoped region.

Formation of 2DEGs

In a 2DEG the solution to the need for an increased dopant concentration for increased charge carrier concentrations is solved in part through the use of more than one material.

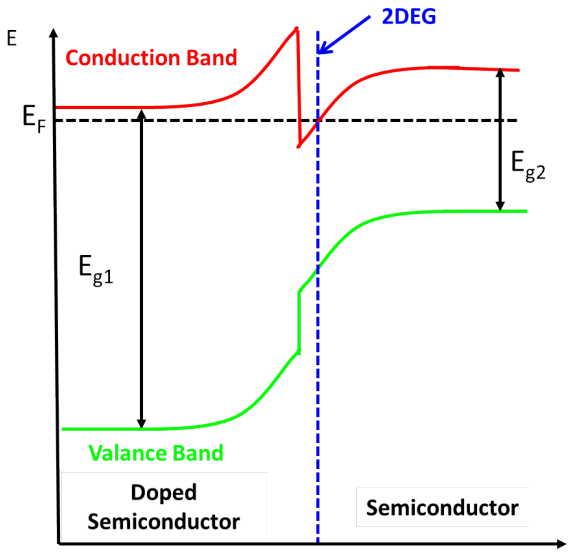

Figure 2.2: Band energy diagram for an intrinsic 2DEG showing the band bending occurring in the conduction band and the valence band. The Fermi energy is marked to show the conduction band bending to below this value and the location of the 2DEG is marked.

One material is a heavily doped semiconductor which exhibits the increase in charge carriers associated with this doping. This is coupled with an undoped semiconductor with a reduced number of charger carriers but with reduced scattering and therefore will exhibit higher mobilities.

The formation of the 2DEG relies on electrons being readily transferred between the two materials so that the high mobility of the undoped semiconductor and the high charger carrier density of the doped semiconductor can both be utilized. This relies on the pinning of the Fermi energy within the band gap of both the semiconductor, E_{g2}, and doped semiconductor, E_{g1}, to be different points within the energy gap to facilitate this movement of charge carriers. If these two materials are in ideal contact the system is forced to equilibrate by charge carriers moving to compensate for the discontinuity in the Fermi energy. The location of the Fermi energies are shown in figure 2.2. It is seen that their relative pinning is different in relation to the conduction band.

The effect of this is that the charge carriers due to donors in the doped semiconductor

flow into the undoped semiconductor causing a build up of negative charge in the undoped semiconductor and an associated positive charge in the doped semiconductor until equilibrium is reached. The undoped semiconductor now has an associated accumulation of electrons and the bands bend to accommodate this. The conduction band bends towards and below the Fermi energy. This causes the spontaneous formation of the 2DEG.

With the electrons in a confined space they act like a particle in a box. A particle in a box separated by a finite length acts as a quantum system and the energy of the particle becomes quantized, forming the energy levels of the electron in the 2DEG.

At low temperatures all levels up to the Fermi energy will be occupied by electrons. If the energy separation between the highest occupied level and the lowest unoccupied level exceeds k_BT then there will be no unoccupied states for electrons to thermally scatter into. It is the combination of this reduced thermal scattering with the limited impurity scattering which gives intrinsic 2DEGs their very high mobility.

Developments with GaAs/AlGaAs

GaAs/GaAlAs is an intrinsic 2DEG system that has been extensively studied since its discovery. It is one of the most characterized 2DEGs and sets much of the background for other material systems demonstrating confined electron spaces. The formation of GaAlAs is key to the formation of the 2DEG. The Al sits on the Ga sites and widens the band gap, and reduces the lattice constant. The change in the band gap can be controlled by the Al concentration. The GaAs/GaAlAs interface needs to be atomically abrupt to benefit from the difference in band energies which creates band bending which forms the 2DEG. The band bending arises from the difference of the pinning of the Fermi energy with respect to the band gaps of both the GaAs and the GaAlAs. In an equilibrium state, the flow of charge carriers compensates for this difference and band bending occurs. Although the 2DEG is spontaneous at the point of growth, other groups have been able to further manipulated it with the addition of gate electrodes to the 2DEG. The band diagram looks similar to that in figure 2.2, with GaAs being the undoped semiconductor and the GaAlAs being the doped semiconductor.

The difference between the GaAs/AlGaAs and the Si MOSFET is that the 2DEG is now

located in a material with no charged donors. This reduces the random potential caused by charged donors and as a result there is less electronic scattering. This allows, theoretically, for much higher mobilities to be achieved than in Si. Although, in reality, the electron densities observed are similar to that of the Si MOSFET.

There can be further improvements to this system by band gap engineering. The band gap of the GaAs layer is reduced by the addition of In [26]. This increases the band offset with the AlGaAs, increasing in the amount of charge that can be transferred. There are many advantages of this simple addition of In to the GaAs layer including lower effective masses and higher mobilities, larger energy separations between the conduction band minima and a reduction in real-space transfer due to large band offset [27] [28] [29]. One issue arising from the In incorporation in the system is an increase in lattice parameter which can have a large effect on the properties due to the lattice matching issues during the growth. This can lead to tetragonal distortions from the relaxation of the strained film. The strain within the film produces an increase in band energy and breaks the degeneracy of the energy bands. There is a critical thickness where the strain is relieved and misfit dislocations arise relaxing the film and returning the band energies to that of before. These dislocations degrade the performance of the devices. The critical thickness can simply be controlled by varying the In concentration [30]. Although high levels of In would be required for optimum electronic properties [30], the physical strain and therefore a very small critical thickness would make it unworkable. As a compromise the average In concentration is 15% which gives a well depth of 20 nm which gives high confined state energies and slightly reduced charge transfer.

Mobilities as high as 3 x $10^7 cm^2/Vs$ [31] have been achieved and have revealed a plethora of exotic phenomena at low temperatures including but not limited to, fractional quantum Hall physics in the second Landau level, various exotic fractional fillings, spin-qubits and two-dimensional hole systems [32] [33] [34].

Progression to oxides

To improve the quality of the 2DEG i.e. to achieve higher mobilities and to observe new phenomena, improvements in two main areas are required. The first is the crystalline quality

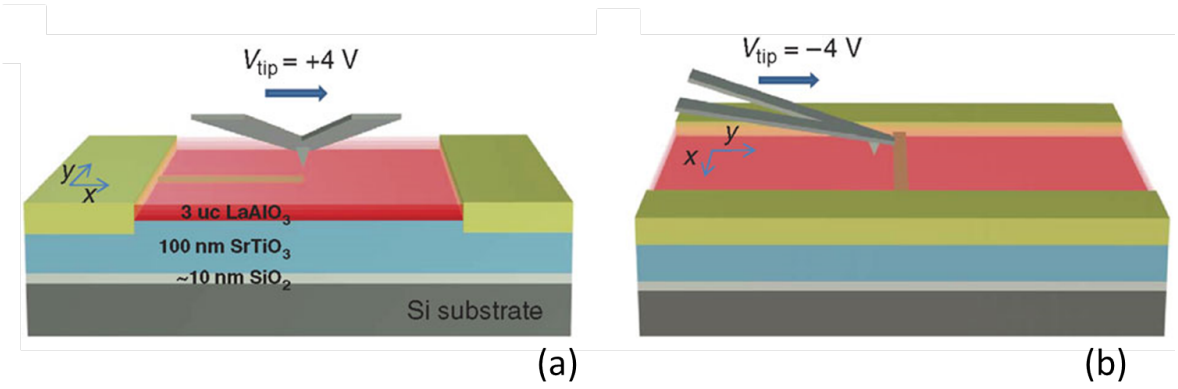

Figure 2.3: Schematic showing the (a) "write" and (b) "read" capabilities of LAO/STO 2DEG interfaces. Scan direction of the charged AFM tip in humid atmosphere shown as a blue arrow, conductive channel shown as a green line. Figure taken directly from reference [8].

of the interfaces. This is in constant need of improvement as the prerequisite for the formation of the 2DEG is that there is an atomically smooth interface in which the electrons are confined. The second issue is the utilization of materials that better satisfy the criteria for a 2DEG. A 2DEG, similar to that seen at the GaAs/AlGaAs, was also observed between two oxide insulators, $LaAlO_3$(LAO) and $SrTiO_3$(STO) [35].

LAO/STO differs from previous 2DEG in that no external field or impurity doping is necessary for the formation of the 2DEG. $LaAlO_3$ and $SrTiO_3$ compounds are well-known band insulating oxides with perovskite ABO_3 structure [36]. 2DEGs at such an oxide interface can have a large range of properties which can be utilized and studied. These properties arise due to correlations resulting from electron- electron interactions or electron- lattice interactions [37]. These interactions are characteristic of oxide materials [38]. This differs from previous theories that are based on non-interacting electrons moving in an effective potential determined by an averaged background electronic charge- these models are no longer applicable to this oxide system.

These correlations lead to a large range of properties including thermoelectricity [39] superconductivity [40] and piezoelectric responses [41]. Strong electron-electron correlations

may also lead to the observation of the fractional quantum Hall effect, although in the LAO/STO case the low mobility of the doped carriers and their high concentration have hindered the successful demonstration of this [42]. Compared to previous 2DEGs there is a narrower spatial distribution of electrons at this interface (approximately 2 nm). This enables the fabrication of nanoscale electronic devices and 2D motion is better approximated [43]. This does, however, mean that there is a greater dependence on the interface morphology, which has to be controlled during growth. The mobility of the 2DEG is strongly dependent on the number of unit cells of STO grown, varying in the literature but mostly observed from 5 unit cells of STO deposited [44]. Such control is difficult to obtain and requires the use of very low growth rates. With such growth rates, truly atomic layer deposition is observed and the effects of the surface are reduced. One such property of having the 2DEG close to the surface is the ability to "write" the conduction channels with a charged AFM tip in a humid atmosphere. Here the mobility of the interface is affected by the addition and removal of dissociated H_2O molecules [8]. The schematic of such a device is given in figure 2.3.

The exact mechanism of 2DEG formation differs from GaAs/GaAlAs and has been under much dispute. There are three hypotheses: the "electronic reconstruction" scenario (the ideal picture explaining the formation of a 2DEG in the case of perfectly stoichiometric LAO and STO layers) [45]; extrinsic mechanisms (i.e. that the entire physics is attributed to extrinsic doping of the STO layers next to the interface, associated with possible cationic disorder and/or oxygen vacancies); finally, more recently, several theoretical approaches appeared in the literature suggesting that the polar instability [46], which is the essential ingredient in the "electronic reconstruction" scenario, is the driving force for stabilization of the system that could take place by formation of specific defects at the interface and at the surface. All of these have their positives and negatives; a detailed analysis goes beyond the scope of this work.

LAO/STO 2DEGs have low-temperature electron mobilities up to the range of 10^4 $\mathrm{cm}^2 V^{-1} s^{-1}$ [35] [37] [47], being limited by scattering from crystal defects.

Recent developments in ZnMgO/ZnO interfaces

This dissertation will focus on the interface between ZnO and ZnMgO. ZnMgO/ZnO is another oxide interface which has capabilities for the formation of a 2DEG. The ZnMgO/ZnO 2DEG mirrors that of GaAlAs/GaAs, with the intrinsic formation of a 2DEG; but instead of doping causing the formation of the 2DEG, it is caused by a change in polarisation. There are some advantages over other systems, including a larger effective mass, small spin-orbit coupling and even-denominator fractional quantum Hall effect. There is a lower lattice mismatch for the same conduction band offset compared to other systems such as GaAs/AlGaAs [48]. There is a greater availability of native substrates, which are set to increase in quality, and there is a wider range of wet-chemical processing available compared to GaN [49]. However, there are still problems with obtaining high quality, reproducible substrates commercially compared to GaAs. This problem has been touched upon in the previous chapter. With variations in quality of ZnO substrates on a company-to-company and batch-to-batch basis there is little consistency. The effects of these lower quality substrates (with the higher quality substrates from Tokyo Denpa no longer available) have not been fully characterized. This dissertation hopes to identify some of the effects of these lower quality substrates and to further understand how it affects the scattering processes involved, which is important to understand in order to optimize future 2DEGs.

ZnO is one of the most prominent materials in the metal oxide family [20]. The wurzite ZnO structure is a Zn centered octahedron, with the Zn atom skewed off center, therefore removing the center of inversion and the symmetry it brings. The unit cell of ZnO is seen in figure 2.4. Without this symmetry, there is a spontaneous electric polarization along the [0001] axis which aids the spontaneous formation of a 2DEG at the ZnO/ZnMgO interface [50].

The ease of band gap engineering is also of great advantage. The addition of ternary elements such as Mg onto Zn sites can vary the band gap and polarization without causing a large lattice mismatch between films. Charge carriers in ZnO have a large effective mass due to it being ionic [51] and electrons being strongly correlated.

The correlation of the electrons is governed by the Coulombic interaction which forms the

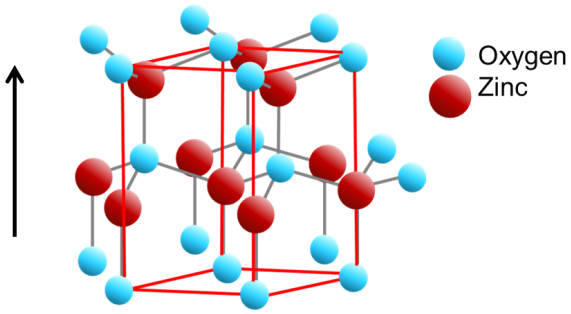

Figure 2.4: Wurtzite crystal structure of ZnO, with [0001] Zn polar face facing the direction of the arrow and the [000-1] O polar face on the bottom of the structure. On the Zn polar face the Zn atoms have unsaturated dangling bonds. Unit cell is noted through red lines.

basis for the fractional quantum Hall effect which can be observed at the interface, as will be discussed later. In these 2DEG systems the Coulomb interaction dominates the physics in magnetic fields. In low magnetic fields, the interacting charge carriers can be treated with the Fermi liquid theory as noninteracting quasiparticles with renormalized effective mass and Landé g factor. Another advantage of ZnO to other 2DEG systems is that the Fermi surface is a sphere [52]. This gives it the advantage of not having multiple anisotropic Fermi surfaces which would complicate the assignment of various phenomena. This, coupled with the large effective mass makes ZnO it an ideal candidate for investigations into the quantum Hall effect.

There is no doubt that the leaders in the deposition of ZnMgO/ZnO are the Tsukazaki and Kawasaki groups and those whom have worked closely with them. From their initial observation of the fractional Hall effect [53] to current publications, they lead the field in both fundamentals of materials deposition [6] to observation of quantum effects [54]. They have evaluated the importance of surface preparation and shown the importance of buffer ZnO layers in increasing the mobility at the ZnMgO/ZnO interface. The importance of the pre-growth conditions is non-trivial as they have exhibited gains of two orders of magnitude in the low temperature mobility in the implementation of them. This work on substrate preparation also acts as a starting point for my own work in chapter 5.1. The mobilities observed by them currently exceed 10^6 cm^2 V^{-1}s^{-1} [6].

Optimization of the system is still on-going but results so far have indicated that a signif-

icant band offset can be created with minimal Mg incorporation, with Mg concentrations of less than 1% producing large mobilities [55]. At 1 % Mg incorporation there is little lattice mismatch and the crystalline quality of the 2DEG allows for high mobility. There has also been much work done on the calibration of Mg content at low concentrations [56] which is needed when dealing with such small concentrations of Mg.

As previously stated ZnO, being ionic, has a large effective mass. As the fractional quantum Hall effect originates from multi-body interactions, the larger effective mass makes these fractional states more pronounced than in other 2DEG systems. Electron correlations in ZnMgO heterostructures have been studied at low magnetic field with there being a 60% increase in the electron mass compared to ZnO. There has also been work on both even- and odd- denominator fractional Hall effect. Here the Landau level (fully described later in chapter 2.2.1) is not fully filled but a fractional state is observed. The origins of the odd and even fillings are different. At high magnetic field a filling factor ν equal to 1/2 has been observed with the composite fermion mass being similar to the ZnO effective mass, which is in stark contrast to the GaAs values [57]. There has also been investigation into the origins of the $\nu = 1/3$ state and lower with the discovery of the magnetic-field insulating phase which has been attributed to the disorder-induced quantum Hall insulator or Wigner solid [7].

All of this work further characterizes the ZnO/ZnMgO system, allowing for better understanding but also better device applications. ZnMgO/ZnO 2DEGs have natural advantages for application in a number of fields. The small spin-orbit coupling in ZnO due to its ionic nature means that the spin coherence length may be significantly larger then that of AlGaAs structures for spintropic devices.

Other groups have also been looking at alternative deposition techniques including MOCVD and changing substrates to the more widely available and reproducible sapphire [58] [59] [60] as well as ascertaining the exact band structure [61] [62].

Although there has been much work into the fundamentals of the ZnO/ZnMgO system, actual applications of the system, compared to GaAs/GaAlAs, have so far been limited. The importance of this still relatively young system should however not be diminished. Publications on the fundamental science of these states has increased over the years. An improved

understanding of the system may pave the way for applications such as high mobility transistors and gatemon-type qubits.

2.1.3 Three Dimensional Electron Slabs

Confined electrons have also been observed at graded interface systems as distinct from the abrupt interfaces that have been discussed previously [63]. These are called three dimensional electron slabs (3DES). One advantage of the graded system is a more diffuse carrier concentration in the conduction channel. This leads to a reduction in non-equilibrium polar optical phonons which could limit high-field velocity of carriers at high carrier concentrations [63]. It is also postulated that the reduction of charge carrier density will further increase electron correlation effects, resulting in enhancements of electron mass and spin susceptibility [64]. Despite the promise of diffuse electrons at graded interfaces, high mobilities have not yet been realized. These 3DES are realized when there is a change in the polarization of the material over a graded interface and have been shown in ZnO/ZnMgO graded interfaces. Although such an interface has been realized, the possible implications of degree of confinement and variations in this length scale have not been investigated. This is one issue which this dissertation hopes to address.

The way in which it is formed and where it is located is different from the 2DEG and it only occurs in polar materials. By grading the composition of the material between the binary semiconductor and the ternary semiconductor over a finite distance, the positive polarization sheet becomes a bulk three-dimensional polarization background charge. The charge profile is given by the divergence of the polarization. Considering only changes along the growth direction (z), the charge density is given by $N_D^{Pol}(z) = \nabla \ . \ P = \delta P(z)/\delta z$. This charge profile will depend on the nature of the grading. If the concentration ternary component varies linearly then the charge profile is constant and is given by:

$$N_D^{Pol}(z) = [P(z_0) - P(0)]/z_0, \tag{2.1}$$

where $P(z_0)$ is the polarization (spontaneous and piezoelectric) at the interface z=z_0.

Under compressive strain, the spontaneous and piezoelectric polarization in the ternary

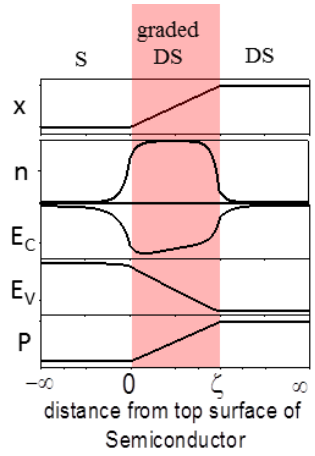

Figure 2.5: Schematic diagrams showing the fractional dopant concentration, x, carrier density, n, conduction band edge, E_C, valence band edge, E_V, and charge polarization, P, across a linearly-graded interface of finite width between semiconductor and doped semiconductor. Note that in reality the magnitude of the change in E_V exceeds that of E_C by one or two orders of magnitude so that the spatial variation of the bandgap essentially follows that of E_V.

semiconductor should be considered, but in the completely relaxed substrate only spontaneous polarization should be taken into account. To demonstrate this, consider the unit cell of the ternary semiconductor, and assume it contains a change in dipole due to the spatial separation of the electron clouds and the nuclei. The dipoles in the sheets of each unit cell neutralize each other in the bulk semiconductor. However, the strength of the dipole changes with increasing ternary component composition, breaking the local neutrality. We then divide the ternary semiconductor into N units with a linear change in ternary component composition from 0 to x_0. The unit number N is equal to d/c where d is the thickness of the graded area and c is the length of the unit cell. The ternary component composition for the i-th unit cell is $\frac{N-i}{N-1}x_0$ and the unbalanced bound sheet charge is equal to $\pm P^i_{SP+PE}/q$ at the upper (+) and lower (-) surfaces and where P^i_{SP+PE} is the polarization of the i-th cell due to spontaneous and piezoelectric polarization and q is the electronic charge. Due to the gradient of the polarization discontinuity $\Delta P < 0$, the unbalanced net bound charges are positive with a sheet density of $(P^i_{SP+PE} - P^{i+1}_{SP+PE})/q$ at the interface between unit cells i and i+1.

As a result the bound positive polarization charges are spread through the linearly graded layer with a volume density of $N_{D\pi} = \nabla P = \sigma_\pi/dq$ [65], where σ_π is the sheet conductivity. This fixed positive background attracts free carriers from remote donor-like states to satisfy Poissons equation and maintain charge neutrality. The end result of the charge rearrangement makes the polarization bulk charge act as a local donor with a zero activation energy. As there are charge carriers without donors this removes ionized impurity scattering and could result in higher mobilities.

This is demonstrated in figure 2.5. Here the change in polarization dominates and the charge carriers are seen to be located in the ternary semiconductor, not the binary semiconductor as seen in 2DEGs. Figure 2.5 also shows the effect on the band energies. The width of such a 3DES can be of order 100 nm but the exact size depends on the materials and degree of ternary component incorporated.

2.2 Electronic States in 2DEG

2.2.1 Energy Levels in ZnO Magnetic Field

Confining of the electrons in the 2DEG and 3DES is key to unlocking many new areas of science. These phenomenon become evident due to the carriers being confined to a space that is comparable to or smaller than the de Broglie wavelength of the charge carrier. In this 2D space the electron is confined in a box. We can solve the time independent Schrodinger equation for a particle in a box to determine the quantization of energy levels. We take the potential, U(z), in the time-independent Schrodinger equation, to be zero inside a one-dimensional box of width a and infinite outside the box. For a particle inside the box a free particle wavefunction is appropriate. This ultimately gives, for a carrier confined to this infinitely deep well, a quantized energy, given by:

$$E_M = \frac{\pi^2 \hbar^2 M^2}{2m^* a^2}, \tag{2.2}$$

where m^* is the effective mass of the carriers, a is the dimensions of the box and M is a positive integer number defining the quantum number of that given energy level.

Moving to a 1D space where the carrier is constricted in the (x, y) plane, the total energy is given by:

$$E = E_M + \frac{p_x^2 + p_y^2}{2m^*}, \tag{2.3}$$

where p_x and p_y are the momenta of their respective directions.

For charge carriers to be quantized there are a number of other constraints; splitting of the energy levels must be larger than the thermal energy of the system ($k_B T$) so that no thermal fluctuations between levels can occur.

Effects of scattering must also be taken into account. Scattering in the system can occur due to phonons, impurities, defects and many other sources. For a given scattering time, τ_s, the Heisenberg uncertainty principle states that the uncertainty of an energy level becomes $\Delta E \geq \hbar/2\tau_s$. The separation of neighboring energy levels must be greater than this uncertainty. The mobility is related to the scattering lifetime by:

$$\mu = \frac{e\tau_s}{m^*}. \tag{2.4}$$

Therefore to observe quantum phenomena the system must exhibit low temperature high mobility, and high surface quality.

2.2.2 Applied Magnetic Field

Due to the confined dimensionality in these electronic systems, we must consider two components of an applied magnetic field, parallel or perpendicular to the direction of the current flow. The component that is parallel to the confined electron space will not change the characteristic features of the energy spectrum but will change the component of the effective mass perpendicular to the applied field.

When the magnetic field is applied perpendicular to the electric field this will alter the energy spectrum dramatically. For this situation it is assumed there is no in plane field component for simplicity. Due to this there is no change in the z-direction (perpendicular to the direction of the flow of current) and therefore no change in the quantisation energy levels which are dictated by the quantum well potential. The Schrödinger equation of spin-less, non interacting, massive electrons in 2D space, takes the form:

$$-\frac{\hbar^2}{2m^*}\left[\left(-i\frac{\partial}{\partial x} - \frac{eB}{\hbar}\right)^2 - \frac{\partial^2}{\partial_y^2}\right] \cdot \psi(x,y) = E_\perp \cdot \psi(x,y), \tag{2.5}$$

The vector potential is:

$$A_x = -yB, A_y = 0, \tag{2.6}$$

where B is the magnetic field applied in the z-direction. Assuming the waveform:

$$\psi(x,y) = e^{ip_x x/\hbar}\chi(y), \tag{2.7}$$

we can now express the motion of this electron as the following:

$$-\frac{\hbar^2}{2m^*}\chi'' + \frac{m^*\omega_c^2(y-y_0)^2}{2}\chi = E_\perp\chi, \tag{2.8}$$

where y_0 is the central position of the oscillator, given by:

$$y_0 = -\left(\frac{1}{eB}\right) p_x. \tag{2.9}$$

The magnetic length, l_0, which physically manifests itself as the length of the electron trajectory where the electron gains a phase factor comparable with 2π from the magnetic field, is given by:

$$l_0 = \sqrt{\hbar/eB} = \sqrt{\hbar/\omega_c m*}, \tag{2.10}$$

where $\omega_c = eB/m^*$is the cyclotron frequency. These two equations can then be combined to give an expression for the ground state oscillator:

$$y_0 = -l_0^2 \left(\frac{p_x}{\hbar}\right). \tag{2.11}$$

Now we can define the total energy, from equation 2.3, as:

$$E = E_M + \hbar\omega_c(N + 1/2), \tag{2.12}$$

where N is a positive integer, giving $\hbar\omega_c(N + 1/2)$ as eigenvalues of $E_\perp$. These eigenvalues are known as Landau Levels. With these levels being filled by electrons it is important to take into account the spin effects which give new energy levels separated by Zeeman splitting energy:

$$E = E_M + \hbar\omega_c(N + 1/2) \mp \frac{1}{2}\mu_B g B \tag{2.13}$$

where μ_B is the Bohr magneton and g is the electron g-factor. The plus sign(+) corresponds to the down spin state of the electron where as the minus (-) to the up state. Taking all this into consideration one would expect that in an ideal case there is a sizable quantization: the Landau levels are separated by cyclotron spacings of $\hbar\omega_c$, which are subsequently split by the Zeeman energy given by $\mu_B g B$.

Now consider where the Fermi level falls. This is typically lower then the overall magnitude of the quantized energy levels at low temperatures, therefore only the lowest energy level will

be filled so $E_M = E_1$. When considering a model with non-zero field applied in the z-direction, while the direction of motion is in the $x-y$ plane, the characteristics of the motion are described by the momentum component of the direction of travel, p_x and the discrete values of N denote the Landau level. Due to the energy only being dictated by N and the direction of spin, the Landau levels are degenerate over the momentum and oscillator position. It can be shown that Landau level degeneracy can be expressed as $L_x L_y \times 1/2\pi l_0^2$ where L_x and L_y are the dimensions of the confined electron space in the x and y directions giving the degeneracy per unit area as $2\pi l_0^2$ [66].

Now the density of states, n_{DS}, can be given by:

$$n_{DS} = \frac{eB}{h}, \tag{2.14}$$

for the previously stated magnetic length l_0. Once filled these Landau levels are defined by a filling factor v,

$$v = \frac{n}{n_{DS}}, \tag{2.15}$$

where n is the charge carrier density. This implies that the filling factor is inversely proportional to the applied magnetic field. Therefore from equation 2.5 and multiplying it by the corresponding degeneracy factor one can find the density of states for that degenerate electron system.

2.2.3 Hall Effect

To understand fully the Hall effect it is useful to refer back to the Drude model, a model originally used to model electron conduction in metals based on the kinetic theory of gases and the following assumptions:

- the independent electron approximation: there are no electron-electron interactions between collisions
- the free electron approximation: there are no electron-ion interactions
- the collisions between electrons and ions are instantaneous, uncorrelated events which will result in an abrupt change in electron velocity

- the probability of an electron having a collision in any given time interval, dt, is dt/τ where τ is independent of position and momentum
- only collisions are responsible for the electrons achieving thermal equilibrium with their surroundings

Given all these approximations the resistivity ρ can be defined by:

$$E = \rho j, \tag{2.16}$$

where E is the electric field and j is the current density, which is subsequently defined as:

$$j = -nev, \tag{2.17}$$

where v is the average velocity of the electron and is given by:

$$v = -\frac{eE\tau}{m}. \tag{2.18}$$

A combination of equations 2.17 and 2.18 gives the expression for current density as:

$$j = \sigma_0 E, \tag{2.19}$$

where σ_0 is the conductivity given by:

$$\sigma_0 = \frac{ne^2\tau}{m}. \tag{2.20}$$

Given these definitions, we can now add a magnetic field to the system. In a magnetic field the electrons motion is classically described by:

$$m\frac{\partial \overrightarrow{v}}{\partial t} + \frac{m\overrightarrow{v}}{\tau} = -e(\overrightarrow{E} + \overrightarrow{v} \times \overrightarrow{B}). \tag{2.21}$$

Here the inclusion of τ takes into account the electron scattering as previously mentioned. If the magnetic field is perpendicular to the direction of travel i.e. $\overrightarrow{E} = E\widehat{x}$ and $\overrightarrow{B} = B\widehat{z}$, by invoking the steady state approximation [67] then the matrix form of the previous equation becomes:

$$\begin{pmatrix} \frac{m}{\tau} & eB & 0 \\ -eB & \frac{m}{\tau} & 0 \\ 0 & 0 & \frac{m}{\tau}(1+\omega_c^2\tau^2) \end{pmatrix} \begin{pmatrix} v_x \\ v_y \\ v_z \end{pmatrix} = -e \begin{pmatrix} E \\ 0 \\ 0 \end{pmatrix}. \tag{2.22}$$

The conductivity is given by:

$$\sigma = ne^2A^{-1}, \tag{2.23}$$

where A is the 3 x 3 matrix in the equation 2.22. Hence:

$$\sigma = \frac{\sigma_0}{1+\omega_c^2\tau^2} \begin{pmatrix} 1 & \omega_c\tau & 0 \\ \omega_c\tau & 1 & 0 \\ 0 & 0 & 1+\omega_c^2\tau^2 \end{pmatrix}, \tag{2.24}$$

where ω_c = eB/m is the cyclotron frequency. It can be seen that as there is no force along the z direction the conductivity in this direction is equal to σ_0. When considering the plane of conduction σ_{xy} , the applied field now does have a significant effect on the conductivity, so:

$$\sigma_{xy} = -\sigma_{yx} = \frac{\omega_c\tau\sigma_0}{1+\omega_c^2\tau^2}. \tag{2.25}$$

As there is now a y component of the conductivity, there is an associated voltage, known as the Hall voltage. The effect of there being a voltage perpendicular to both the current and the magnetic field is known as the Hall effect. The Hall voltage can be useful in calculating the number of charge carriers as well as observing other quantum phenomena such as the integer and fractional quantum Hall effect.

Integer Quantum Hall effect

The integer quantum Hall effect is the observation of plateaus in the Hall resistance as a function of magnetic or electric field. These are independent of the device geometry. They were first observed by von Klitzing *et al.* by measuring transverse voltages at a constant magnetic field against a sweeping gate voltage. Their results are seen in figure 2.6. By

changing the gate voltage (the electric field) the Fermi energy can be changed and hence the number of charge carriers.

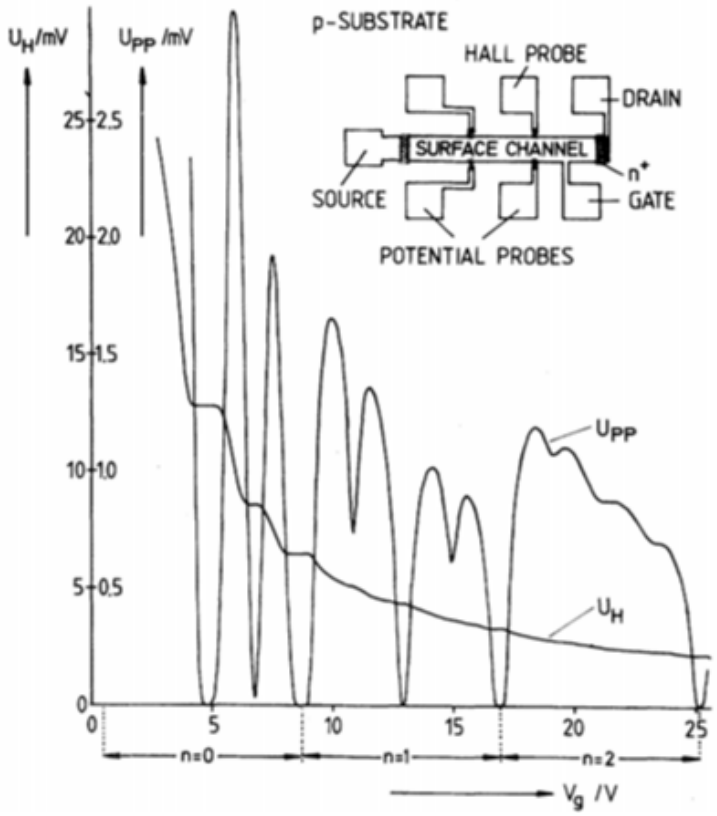

Figure 2.6: The first observation of the quantum Hall effect, labeled U_H. The measurement was taken at 1.5 K at a constant magnetic field of 18 T and a source drain current of 1 μA while sweeping the gate voltage. The inset shows the device design from the top view. Figure taken from [3].

As previously mentioned, a similar effect can be induced by varying the magnetic field. If we consider the case of B=0, the 2D density of states has a constant value as a function of energy. Once a magnetic field in the z-direction is applied the separation of the Landau levels increases and the Landau levels move relative to the Fermi energy, as seen in figure 2.7. Although in the ideal state the Landau levels would have zero width, in real systems this is not achieved due to scattering events. Therefore, there is overlap between neighboring

Landau levels at low magnetic fields. As the magnetic field increases the Landau levels increase in separation reducing the amount of overlap. As this happens Landau levels are pushed through the Fermi energy and electronic properties of the material depend on the location of the Fermi energy in a given Landau level.

Therefore the quantization is observable at higher magnetic fields.

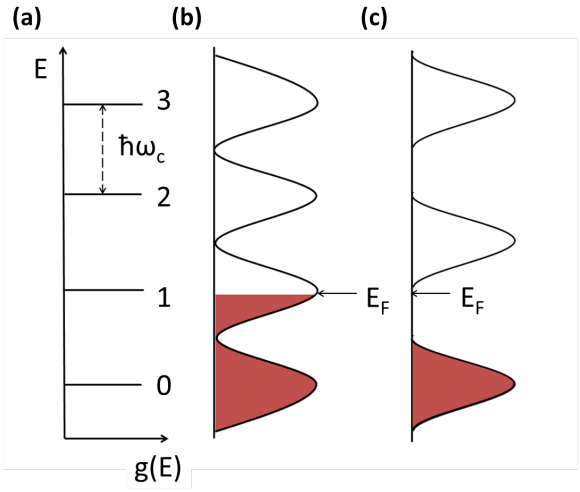

Figure 2.7: The Landau level density of states in ideal conditions, i.e. zero scattering events (a) and in the presence of broadening due to scattering (b) and (c). The shaded portions indicate states filled with electrons. A low magnetic field is applied in (b) and a higher magnetic field applied in (c)

To show the origin of the plateaus as seen in figure 2.6, we take the example of the Fermi energy lying in between two states, similar to that seen in figure 2.7 (c). In accordance with the Pauli exclusion principle, electrons inside each Landau level are forbidden to scatter to other states within the Landau level. Therefore scattering interactions are also forbidden. This is where the perturbation of the states close to the edge of the confined space have an effect. These edge states bend upwards allowing for transport when E_F is in between the Landau levels. They act as a ballistic one-dimensional conductor giving rise to zero resistance in the x-direction. This is observed as Shubnikov de Haas (SdH) oscillations which were discovered before the associated plateaus in the Hall resistance at Bell laboratories [1].

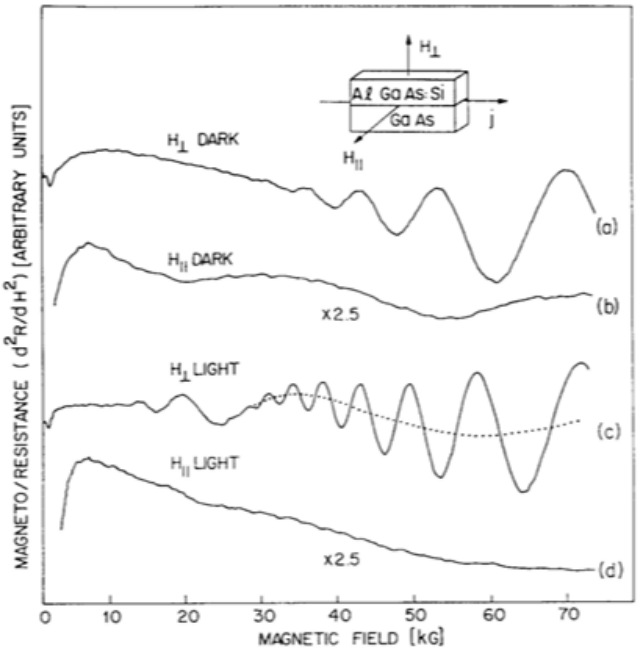

Figure 2.8: The first observation of SdH oscillations, showing the magnetoresistance at a GaAs-AlGaAs:Si interface with field perpendicular or parallel to the 2DEG as indicated. The "light" refers to the sample being in light for 100 secs providing excitation of charge carriers. Figure taken from [1].

In a classically strong field the conductance in the x direction is given by:

$$\sigma_{xx} = \frac{e^2 n}{m^* \omega_c^2 \tau}, \tag{2.26}$$

and the Hall conductivity is given by:

$$\sigma_{xy} = \frac{e^2 n}{m^* \omega_c}. \tag{2.27}$$

Again taking B as the field to get the Fermi energy to lie in between Landau levels or between levels split by Zeeman splitting, the Hall resistance now only depends on e, h and v_N (the Landau filling factor, N), and is quantized in integer multiples of e^2/h.

As mentioned before, this quantization in the longitudinal resistance gives rise to SdH oscillations. At high enough magnetic fields, where the Landau levels are separated by a significant energy, the density of states becomes a discrete function of $1/B$. At lower magnetic fields, where the separation is not complete, the density of states becomes a continuous periodic function with the same periodicity as these SdH oscillations.

The amplitude of the oscillatory component of the longitudinal resistance, can be expressed as [68]:

$$\Delta R_{xx} = R_0 \frac{X_T}{sinh X_T} exp(-\pi/\omega_c \tau) cos\left(2\pi \frac{E_F - E_N}{\hbar \omega_c} - \phi\right), \tag{2.28}$$

where R_0 is the zero field resistance, E_N is the energy of the energy of the Nth sub band and X_T is given by:

$$X_T = \frac{2\pi^2 k_B T}{\hbar \omega_c}, \tag{2.29}$$

which introduces temperature dependence to the oscillations. This can be reduced to:

$$\Delta R_{xx} = A e^{-\alpha/B} cos(2\pi F/B), \tag{2.30}$$

where A is the amplitude of the oscillation as $B \to \infty$, α is a damping factor and F the frequency of the oscillation in units of magnetic field. As the frequency of the oscillation is a function of the carrier concentration, the density of charge carriers of the 2DES can be

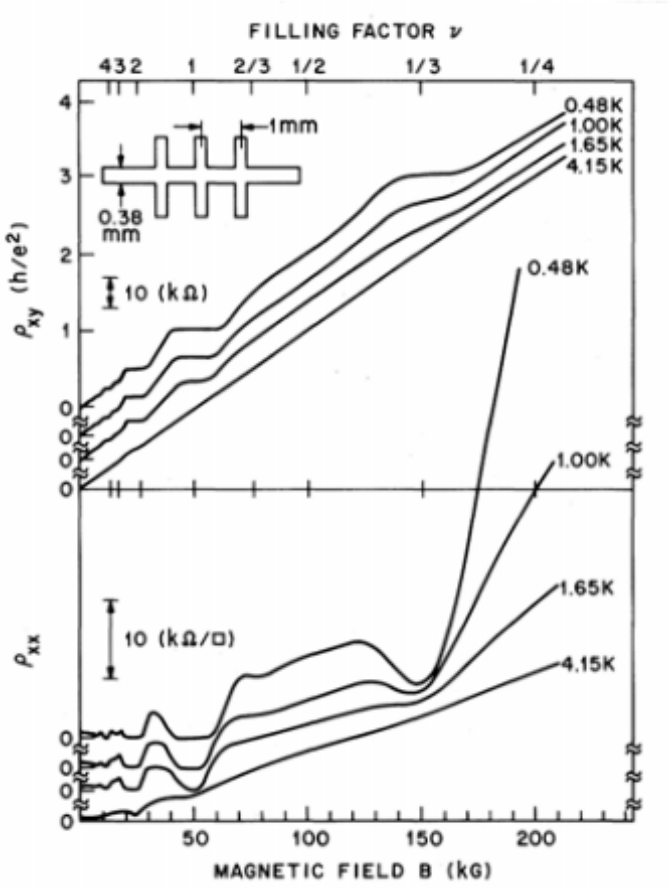

Figure 2.9: The first observation of quantized Hall voltage with fractional filling factors of $v = 1/3$. The inset shows the hall bar geometry of the devices with both longitudinal, ρ_{xx} and hall, ρ_{xy}, resistivities shown. Figure taken from [69].

extracted. From the temperature dependence of the oscillations the effective mass can be extrapolated and from the 1/B dependence the scattering time τ can be calculated. Evaluating these parameters gives insight into the material system.

Fractional Quantum Hall Effect

If we now move to even higher magnetic fields, there comes a point where the Landau levels are separated and shifted so that the filling factor, ν is less than 1. For this to be achieved high quality films with limited scattering are necessary as well as measurement at high magnetic

fields and low temperatures. At these high fields the magnetic length becomes very small and therefore the electron-electron interaction is no longer negligible, nor is the effect of the motion of the charge carriers in field.

For these states for $v < 1$, termed the fractional quantum Hall effect [69], there is the characteristic vanishing of R_{xx} and quantisation of R_{xy}, as seen before, but now at fractional filling factors. Due to the electron interactions no longer being negligible the origin of the fractional quantum Hall effect is intrinsically a many body, incompressible quantum liquid and is often described by the Laughlin wavefunction [70]. Further background of the fractional quantum Hall effect is beyond the scope of this dissertation.

Chapter 3

Theory and Background of Josephson Junctions

3.1 Superconductors

The fundamentals of superconductivity are first needed to fully understand Josephson junctions. The field of superconductivity was created by the ability to liquefy helium in 1908, therefore opening up a whole new area of low temperature physics that had not been previously explored. This was followed closely by the discover of superconductivity in 1911 by Kamerlingh Onnes [71]. For a material to be considered superconducting it must have zero resistance below a critical temperature and be able to expel a magnetic field. The appearance of the zero resistance is the easiest to measure. The temperature at which the resistance goes to zero and perfect conductivity is observed is called the critical temperature T_c.

The second property (the ability to expel a magnetic field) is less trivial to measure. It is observed for temperatures lower then T_c. This effect is known as the Meissner effect and was first discovered in 1933 [72]. The magnetic field is screened from the bulk of the superconductor by screening currents flowing on the surface of the superconductor. The screening current allows the magnetic field to penetrate the superconductor to a small length inside the superconductor, this is known as the penetration length. Screening currents can

only screen a magnetic field up to a certain critical field H_c. Above H_c the magnetic field will destroy the superconducting state and the material will return to the normal state. Current also has this ability to return the material to the normal state. The critical current density, J_c is the maximum current density that a superconductor can withstand in the superconducting state. The supercurrent density is a material property [73].

Superconductivity occurs when the charge carriers inside a material form pairs resulting in a condensate with a lower energy than the uncoupled electrons. A microscopic theory of superconductivity, the BCS theory, formalized this concept [74]. From coupled electrons the theory was developed to introduce the concept of coherence length for the superconducting wave function. The coherence length is the length inside which any change to the electron wave function at one point will propagate to the other electrons within that given coherence length. Although BCS was based around coupled electrons it wasn't complete until Cooper [75] postulated a mechanism for the pairs, which have spatial extent of the order of the coherence length. Electrons with equal and opposite momentum and spin form these Cooper pairs at temperatures below T_c. The overall momentum of the pair is therefore zero and represents the lowest energy state. Then in the superconducting state at T=0 K all the Cooper pairs are in this lower energy state. This is seperated from the excited state by an energy gap $\Delta(T)$ which is given by:

$$2\Delta(0) = 3.52kT_c, \tag{3.1}$$

where k is Boltzman constant. At non-zero temperatures some of these Cooper pairs break from their coupling and quasiparticles are generated. These quasiparticles have both electron and hole like character. With increased temperatures the quasiparticles are excited across the energy gap as given by equation 3.1. This leaves fewer pairs to be involved in the superconductivity and at $T = T_c$ the number of Cooper pairs is zero.

3.1.1 Types of superconductor

There are two types of superconductor although only one type, Type I, is investigated in this body of work. The most common type of classification is how the material responds to an

applied external magnetic field. The response is defined by the Ginzburg-Landau parameter [76], κ which is defined by:

$$\kappa = \lambda/\xi, \tag{3.2}$$

The superconducting electron density, n_s increases from zero at the boundary of the superconductor to a constant value inside the superconductor and the length scale given by the coherence length, ξ. The magnetic field B decays exponentially to zero inside the super conductor with a length scale of λ. Superconductors are classified by κ; type I with $\kappa < 1/\sqrt{2}$ and type II $\kappa > 1/\sqrt{2}$

Type I Superconductors

In a type I superconductor, the coherence length is larger than the penetration depth. Any applied magnetic field up to the critical magnetic field B_c is therefore not able to disturb the coherence of the Cooper pairs. Once the applied field value is above B_c the coherence of the Cooper pairs is destroyed and the superconductor returns to the normal state. Zinc, which we will be investigating in this work, is a Type I superconductor.

Type II Superconductors

In a type II superconductor the penetration depth is larger than the coherence length. In this case the external magnetic field penetrates inside the superconductor deeper than the coherence length. Type II superconductors screen out all the applied magnetic field up to a lower critical field, B_{c1}. A magnetic field greater the B_{c1} enters the superconductor in the form of vortices or flux lines. Each vortex contains a quantized amount of magnetic flux which is screened by the circulating currents inside the superconductor. This quantity is known as the flux quantum, Φ_0. Superconductivity persists until the field applied exceeds the upper critical field, $B_{c1} > B_{c2}$

3.2 Josephson Junction

A Josephson junction consists of a thin insulator sandwiched by two superconductors, leading to an overlap of the wave functions of the two superconductors. The initial prediction [77] was soon experimentally observed [78] [79]. Cooper pairs in the superconductors tunnel through a thin insulating region which is classically forbidden. The current through the junction is a sine function of the difference, ϕ, between the phases of the two superconducting wavefunctions. The current-phase relation is given by

$$I = I_c sin(\phi) \tag{3.3}$$

where I_c is the Josephson critical current and is the maximum current where superconducting behaviour can be observed at a given temperature and field. The phase difference across junction is related to the voltage across it. This is governed by the ac Josephson effect given by

$$V = \frac{\hbar}{2e}\frac{d\phi}{dt} \tag{3.4}$$

Overall the critical current is a measure of the coupling strength of the two superconductors. The energy depends on the dimensions of the insulating material as well as the properties of the material itself. The Josephson coupling energy of the junction is given by

$$E_J = \frac{\hbar I_C}{2e} \tag{3.5}$$

Where I_c is inversely proportional to the normal state resistance, R_n. Therefore $I_c(T)R_n$ has a fixed value which depends on material properties and temperatures and not the dimensions of the junction itself. I_cR_n is a measure of ideality of the junction. The temperature dependence of I_c is given by

$$I_c(T)R_n = \frac{\pi\Delta(T)}{2e} tanh(\frac{\Delta(T)}{2k_BT}) \tag{3.6}$$

Therefore at T=0 $I_cR_n = \pi\Delta(0)/2e$. The critical current and conductance tunnel decrease exponentially with increasing barrier thickness.

3.3 Material Background of Josephson junctions

The weak link between the two superconducting materials is the basis for all Josephson junctions. There are numerous ways of forming such weak links have been explored for both metallic low-temperature superconductors (LTS) and oxide high-temperature superconductors (HTS). These include metal or semiconductor links, grain boundaries, very narrow constrictions, damaged regions, and, most prominently, insulating tunnel barriers. To date it has not been possible to demonstrate a tunnel junction in the technologically interesting high-temperature superconductors, but tunnel junctions play a prominent role in LTS electronics. For this reason, and due to the fact that tunnel junctions offer the best observation of many of the important characteristics of Josephson junctions, we will focus most of our analysis on these devices. Applications of Josephson junctions are wide reaching. One area is quantum computing where Josephson junctions provide a good candidate for the construction of quantum bits (qubits). The system is attractive because the low dissipation inherent to superconductors makes it possible in principle to achieve long coherence times.

The most widespread LTS Josephson junction is the Al/AlO_x/Al junction due to the ease of oxidation and control. A common technique for fabricating such junctions is double-angle shadow evapouration [80]. This has been the most successful fabrication approach to date for making long-lived, high-coherence superconducting quantum bits [81]. An alternative technique for tunnel junction fabrication involves the selective etching of whole-wafer superconductor/insulator/superconductor (SIS) trilayers [82]. Spectroscopic measurements on qubits fabricated in this manner have shown that epitaxial Al_2O_3 tunnel barriers have fewer two-level fluctuators, a known source of decoherence, than diffused, amorphous oxides [83].

Josephson junctions made entirely of refractory materials, such as Nb and NbN, are expected to be applied to high speed digital and analog circuits. In these applications Josephson junctions must be stable and thermally cyclable, have large gaps, high junction quality, and tolerate relatively high process temperature [84].

Much effort has gone into the improvement of the quality of refractory junctions, especially to reduce the leakage current in the sub-gap voltage region. The breakthrough was made

by Kroger and co-workers [85]. They fabricated junctions using a method known as SNAP (selective niobium anodization process), in which a trilayer comprising of a base electrode, an insulating barrier, and a counter electrode was made on a whole silicon wafer without breaking the vacuum during deposition, combining the patterning process with anodization [86]. SNEP (selective niobium etching process) was developed by Gurvitch et al. [87] They formed the junction pattern by using reactive ion etching instead of anodization. They reported the characteristics of a junction with a Nb/ Al-AlO_x -Al/Nb structure. The junction characteristics were much better than those of Nb/Si-Si:H- Si/Nb junctions. Gurvitch et al. obtained I-V characteristics with a small leakage current. This was due to the use of a very thin Al layer, as thin as 5 nm. The Nb/ Al- AlO_x -Al/Nb junction was further improved by Morohashi et al [88]. They used the self-aligned insulation deposition technology developed by Shoji et al. and showed that Al under the counter electrode was not necessary [89]. They also proposed a new fabrication technology for Nb- Al-AlO_x-Nb junctions, which was named the self aligned contact (SAC) process.

There has been no published work on Zn/ZnO/Zn junctions. They may solve some of the problems that LTS junctions have been facing. The semiconducting ZnO barrier may allow for higher critical currents, whilst having the zinc MBE grown would give the film highly crystallinity, possibly leading to fewer TLS.

Chapter 4

Experimental Methods

4.1 Substrate Preparation

ZnO was hydrothermally grown by SurfaceNet GmbH and Zn-faced (0001) polished. Substrates were 10 mm x 10 mm x 0.5 mm. The substrates have a maximum miss-cut angle of 0.5°ensuring growth on a flat polished Zn face of ZnO. A 300 nm Ti layer was sputtered onto the reverse of the ZnO substrate (unpolished face) to enhance thermal absorption from a radiative heater during growth. Samples were prepared for growth with a 30 second etch in 7:200 HCL:DI water. Substrates were subsequently cleaned in acetone, 2-propanol and deionized water.

4.2 Molecular Beam Epitaxy (MBE)

Molecular beam epitaxy is one of the most widely used vacuum deposition techniques owing to its ability for atomic layer deposition under ultra-high vacuum, giving rise to high purity epitaxial films. A schematic and picture of the SVTA MBE chamber is given in figure 4.1. With the use of a cryo pump and an ion pump the chamber used in this work can achieve a base pressure 10^{-11} Torr without liquid nitrogen cooling. Liquid nitrogen is used when the machine is in use as a heat dump for both the cells and the substrate heater and a cold trap for excess material during deposition. Within the chamber the substrate is positioned

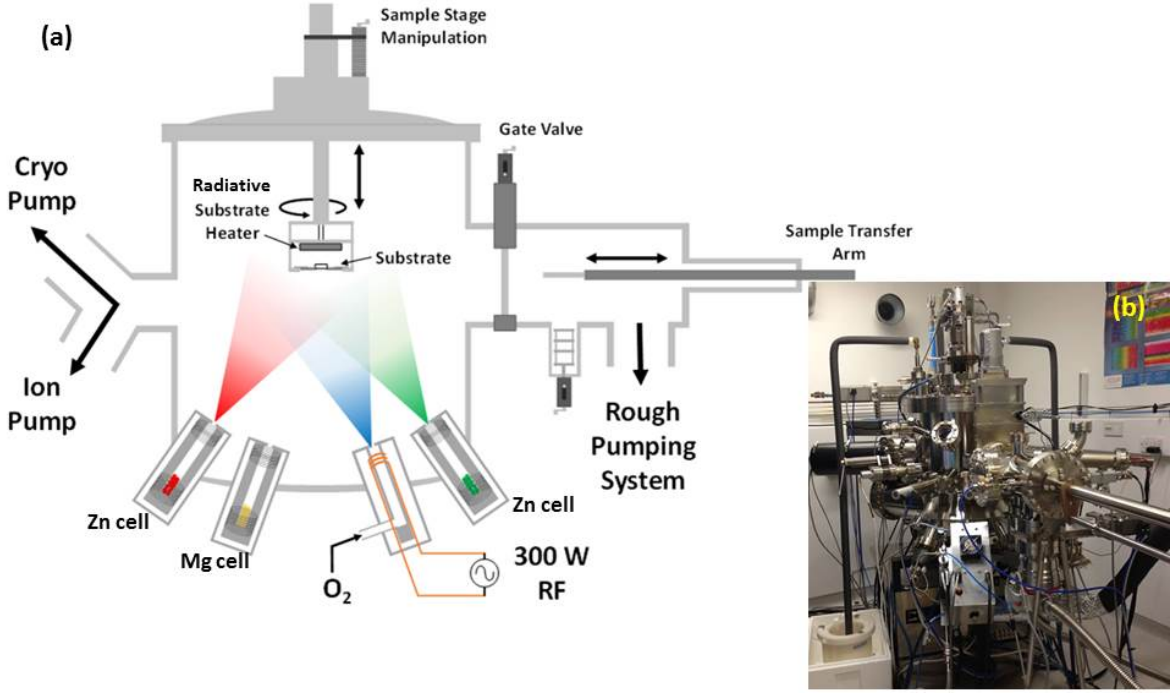

Figure 4.1: (a) Schematic of SVTA MBE system used for this study and (b) photograph of MBE with transfer arm towards the viewer.

at the incident point of the elemental beams. The source material are extremely pure of 5N (99.999%) or higher upon introduction to the chamber. In ultra high vacuum conditions the mean free path of the elemental fluxes introduced is much larger than the dimensions of the chamber. There is no inter beam mixing before the substrate unless the beam fluxes chosen are too large (above 10^{-4} Torr). Inter-beam mixing can hinder the growth of thin films through increased agglomeration of particles before they reach the substrate. The substrate is heated as required and rotated (2 rpm) to facilitate single crystal growth by ensuring uniform flux across the whole surface of the substrate.

4.2.1 Ultra-high vacuum formation

In the system shown in figure 4.1 , the two main pumps used to maintain the ultra-high vacuum are a cryo-pump and an ion pump. Both pumps utilize gas entrapment to create the vacuum. The cryo-pump uses compressed helium at 14 K to cool the cold head cylinder.

Gases with high boiling points condense on the cold head cylinder and are removed from the system. This method reduces with efficacy over time due to the saturation of the cold head by absorbed gases. Therefore regeneration, where the cryo-pump is isolated from the chamber, heated and residual gas pumped off via a scroll pump, is carried out every month to maintain the vacuum in the chamber. The ion pump is used for gases with lower boiling points that cannot be entrapped by the cryo-pump. It works by ionizing the residual gas which is then confined by the cathode of the pump. At the cathode they are either burned off or react removing them from the system. Due to this method of pumping, the ion pump is isolated from the chamber during growth due to the large pressures of oxygen degrading and reducing the lifetime of the cathode, and only the cryo-pump is used. Along with the active pumping, a liquid nitrogen cooling shield is used to condense residual gases on the walls of the chamber during growth. Both pumps are functional up to 10^{-4} Torr and interlocks protecting them are in place.

To initially achieve ultra high vacuum, the chamber must first be rough pumped before the cryo or ion pump may be used, as they cannot be used at ambient pressure. Rough vacuum is achieved using a scroll pump and a turbo pump down to a pressure of 10^{-7} Torr. Both work on mechanically removing air through rotating parts. These two pumps are also used on the load lock. The load lock is the only part of the chamber to be vented when loading samples. From here the samples are transferred from the load lock into the main chamber so that the main chamber is always under high vacuum.

4.2.2 Knudsen effusion cells

The zinc (6N) and magnesium (5.5N) is delivered via Knudsen effusion cells. These are sources where solid elemental materials are heated to produce an elemental beam. The beam equivalent pressure (BEP), the measurable flux, is controlled by the temperature of the cells. These pressures are quantified by a retractable Granville Phillips nude Bayard-Alpert ionization gauge. The dependence of the BEP on the temperature of the cell varies depending on a variety of factors within the cell itself such as the level of filling and condensation on the aperture. Therefore a calibration is needed every time the vacuum is broken, and BEP

is measured before every growth. During growth the cells are dual filament heated, with the tip filament being 50 °C higher in temperature to help prevent condensation on the aperture and create an even beam flux. Pneumatic shutters are used for fast switching of elemental beams.

4.2.3 Plasma formation

Oxygen (5.5N) is activated and supplied as plasma. A radio frequency (RF) plasma is used to create activated oxygen in the form of free radicals. Plasma within the chamber can be sustained for oxygen flow rates of 0.5 sccm to 3 sccm but ignition, via the burst method, can only occur at 2 sccm or higher due to stability reasons. The plasma is created using a standard capacitively-coupled plasma source (SVTA) which operates at 13.56 MHz. 300 Watts RF energy is supplied to the cell through a water cooled copper coil. A pyrolytic boron nitride tube with chargeable aperture is centred between the coils. Oxygen is introduced into the pyrolytic boron nitride tube with a leak value. The leak value can be used to vary the flow of oxygen into the chamber.

The plasma source is operated in high brightness mode, i.e. high power (300 W) and low pressures. Being in this mode provides the highest possible dislocation efficiencies and provides lower ion energy. In low brightness mode the energy of the particles is much higher as it is a capacitivly coupled plasma. With a higher energies the plasma becomes destructive and there is the possibility of damage to the surface of the substrate rather than the desired reaction with the other elemental beams.

A residual gas analyzer quadrupole mass spectrometer was used to monitor the gas injection into the chamber. After stabilising the plasma source for 15 mins the pressure of the H_2, N_2, CO_2, NO and Ar gases are reduced. The pressure of the H_2, H_2O, CO, are still significant enough to be measured via this method, but are all below 3 orders of magnitude lower than the pressure of the oxygen. Although small, the concentration of the H_2 is high enough for the plasma to have a pink glow when observed through the viewing port.

4.2.4 Substrate heating

The sample is heated by a radiative spiral heater. A thermocouple, used to measure the temperature of the sample, is situated above the heater, the same distance from the heater as the sample is held. This does not take into account the variations of the thermal gradient through the substrate to the surface of the substrate. The thermocouple is programed to maintain the temperature to within 1% of working temperature. Fluctuations in the temperature are measured in real time via a pyrometer and are observed to be 2 °C during the growth, although these can only be observed above 400 °C (below this threshold there is not a sufficient thermal radiation for an accurate reading on the pyrometer). The square substrate is held in a 2 inch circular molybdenum holder. Other iterations of the sample holder are discussed in the next chapter. The edges of the substrate which are in contact with the holder and are shielded by the holder are seen to have a different temperature to those in the middle of the substrate. This gives rise to a 1-2 mm region at the edge of the substrate where the film has a very different morphology to the center and is unusable.

4.2.5 Reflective high energy electron diffraction (RHEED)

Reflective high energy electron diffraction provides a powerful *in situ* technique for monitoring film growth. A focused electron beam of energy 15 kV is incident on the sample at 3 degrees grazing incidence and diffracts onto a fluorescent screen which is captured via CCD camera. Due to the small angle of the electron beam and the strength of the electron interaction with the surface the penetration is only on the order of 10 nm, so highly surface-sensitive data can be collected. The crystallographic orientation of the sample, the reconstruction of the surface and the structure of the crystal as it grows can be obtained by looking at the RHEED. These in turn can be assigned to processes occurring on the sample from de-sorption of the oxide to variations in atomic layer growth of the thin film. The crystallographic orientation can be assigned from the spacing in the streaks seen in the RHEED. These streaks can take two forms. These are streaky lines indicating an interaction with a smooth film or dotty streaks indicating a degree of roughness during growth due to reflections off islands during growth.

The atomic arrangement can also be observed. This varies from bulk growth due the

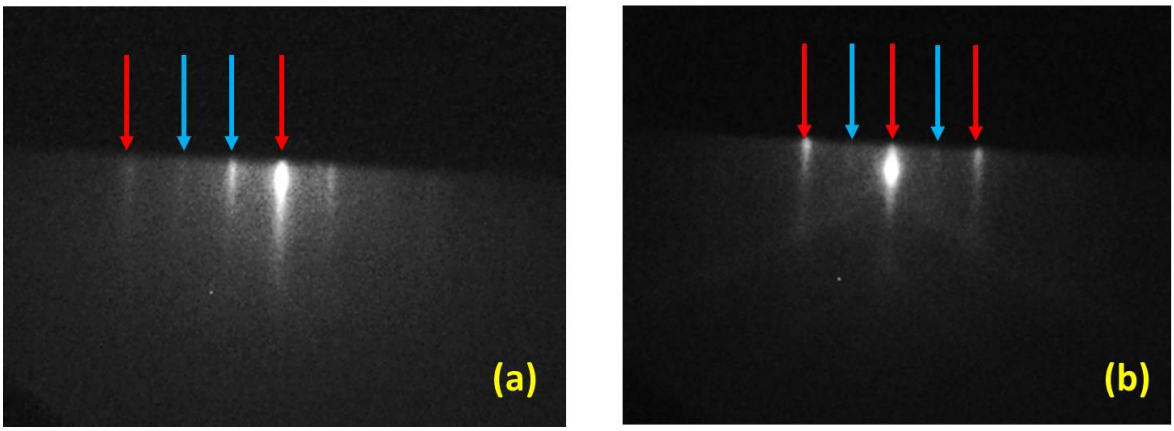

Figure 4.2: (a) RHEED with x 3 reconstruction and (b) x 2 reconstruction on the surface of ZnO at faces 30 deg relative to each other. Sample heated to 500 °C. Red arrows show the deflection from the ZnO [0001] surfaces in different orientations, blue arrows show the reconstruction observed.

presence of dangling bonds in a vacuum during growth. The new arrangement on the surface of the film leads to surface reconstruction. This changes the periodicity of the films surface. The driving force for this interaction is the reduction of the surface free energy. These dangling bonds are subsequently, from unsaturated surface atoms are therefore removed by the addition of bonds between adjacent atoms in a dynamic process. So for reconstruction x2, where the lines are observes with 1 / 2 the periodicity then the expected periodicity on the surface is twice that of what is expected. In figure 4.2 the reconstruction lines can be observed in the film, here x3 reconstruction. Reconstruction is a sign of highly ordered surface and therefore high levels of crystallinity as this high level of periodicity can only be achieved in these conditions.

4.3 Growth Dynamics

4.3.1 Thin film growth dynamics

The environment at the surface of the substrate dictates much of the growth dynamics of the thin film. There are many competing process which affect not only the growth but also the

crystallinity and roughness of the thin film grown. Taking a simplistic view of the growth dynamics we can start growth by looking at the incoming flux j, the sticking coefficient with rate r_a and the diffusion of the atoms on the surface and the de-absorption of atoms from the substrate as r_d. With this description the growth rate R_{growth}, is given by the number of atoms n_{tf} that have adhered to the surface per unit time:

$$R_{growth} = \frac{dn_{tf}}{dt} = r_a n_{free}, \tag{4.1}$$

where n_{free} is the number of particles diffusing on the surface. The rate of change of the number of free atoms will depend on the incoming flux and the adsorption and desorption of free atoms:

$$\frac{dn_{free}}{dt} = -r_a n_{free} - r_d n_{free} + j. \tag{4.2}$$

If we consider dynamic equilibrium in the system the number of free atoms on the surface should be consistent:

$$\frac{dn_{free}}{dt} = 0, \tag{4.3}$$

$$j = r_a n_{free} + r_d n_{free}, \tag{4.4}$$

$$R_{growth} = \frac{r_{aj}}{r_a + r_d} = \frac{j}{1 + r_d/r_a} r_a n_{free}. \tag{4.5}$$

The rate of absorption and desorption are represented by:

$$r_{a,d} = v_{a,d} exp\left(-\frac{\Delta E_{d,a}}{k_B T}\right), \tag{4.6}$$

where Δ E are the activation energies of the process and $v_{d,a}$ are the frequency factors. Combining equation (4.6) with equations (4.3) - (4.5) we get:

$$R_{growth} = \frac{j}{1 + (v_a/v_d).exp\frac{-\Delta E_d - \Delta E_a}{k_B T}}. \tag{4.7}$$

This formula can be used to obtain the growth parameters such as the ratio of desorption and absorption factors v_d/v_a and the difference in activation energies in these two competing processes.

These growth dynamics can lead to three types of growth in an epitaxial regime. The first is Volmer-Weber (VW) growth, where the adatom-adatom interactions are stronger

than those of the adatom with the surface, leading to the formation of three-dimensional adatom clusters or islands. Growth of these clusters will cause rough multi-layer films to grow on the substrate surface. Secondly there is Frank-van der Merwe (FM) growth where adatoms attach preferentially to surface sites resulting in atomically smooth, fully formed layers. This layer-by-layer growth is two-dimensional, indicating that complete films form prior to growth of subsequent layers. Lastly Stranski-Krastanov growth is an intermediary process characterized by both 2D layer and 3D island growth. Transition from the layer-by-layer to island-based growth occurs at a critical layer thickness which is highly dependent on the chemical and physical properties, such as surface energies and lattice parameters, of the substrate and film.

Determining the mechanism by which a thin film grows requires consideration of the chemical potentials of the first few deposited layers. Although we expect that there should little change in the chemical potential when we move to the ZnMgO layer on the ZnO, there is a difference which affects the growth dynamics.

As the wetting layer thickens, the associated strain energy increases rapidly. In order to relieve the strain, island formation can occur in either a dislocated or coherent fashion. In dislocated islands, strain relief arises by forming interfacial misfit dislocations. The reduction in strain energy accommodated by introducing a dislocation is generally greater than the concomitant cost of increased surface energy associated with creating the clusters. The thickness of the wetting layer at which island nucleation initiates, is strongly dependent on the lattice mismatch between the film and substrate, with a greater mismatch leading to smaller critical thicknesses.

4.3.2 Ternary compound growth

Our investigations involve the ternary compound $Zn_{1-x}Mg_xO$. Due to the ZnO and MgO having different crystal structures, hexagonal wurtzite and cubic rock-salt respectively, the simplistic view of Vegards law (empirical law that states that the lattice parameter of a solid solution of two constituents is approximately equal to the relative mixtures of the two constituents' lattice parameters at the same temperature) cannot be used. Instead an

empirical view of the inclusion of the Mg into the structure needs to be taken. Here the literature is taken as a basis. However, each thin film deposition environment may have a variation in the fitting given. There are also variations dependent upon the analytical technique used to analyze this composition, which also must be taken into consideration. In our system we are studying the dependence of the incorporation rates on the ratios between the material fluxes impinging onto the substrate. The material flux is proportional to:

$$J_{(P,Mg)} \propto P_{BEP}/\eta.\sqrt{\frac{T}{M}}, \tag{4.8}$$

where P_{BEP} is the beam equivalent pressure of the Mg, T is the source temperature, M the molecular mass and η is the ionisation coefficient relative to that of N_2. It is given by $\eta = [(0.4Z/14) + 0.6]$, where Z is the atomic number. One of the best ways to determine the composition of the ZnMgO, for ease, accuracy and range of Mg concentrations it holds for, is to measure the energy gap and lattice parameters. Recently Kozuka et al. [56] have measured Mg content using Rutherford Back Scattering, Secondary Mass Spectrometry, XRD, PL and XPS in the range $0.004 < x < 0.4$ and whose results are given in figure 4.3. This has given the most comprehensive analysis over a broad range of compositions using a range of techniques for comparison as well as consideration as to which techniques are best suited to different ranges of magnesium concentration. They have given the following fittings for lattice parameter and band gap energies:

$$\Delta c(\mathring{A}) = -0.069 x_{Mg}, \tag{4.9}$$

$$\Delta E(eV) = 2.2 x_{Mg}. \tag{4.10}$$

These conditions give good agreement with our own as we are also using ZnO substrates.

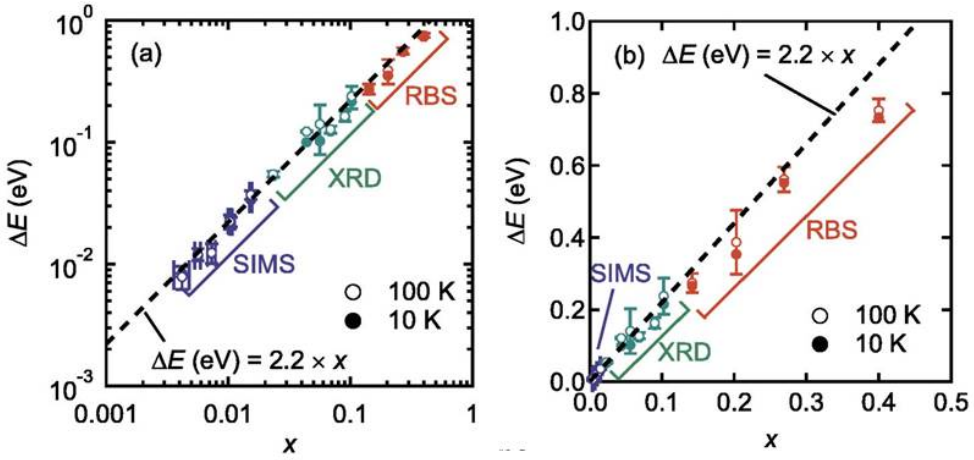

Figure 4.3: (a) Log-log and (b) linear plots of the energy difference (Δ E) between localized emission from Mg_x $Zn_{1-x}O$ films and free exciton emission from ZnO as a function of x at 100 K (empty circles) and 10 K (filled circles) . The free exciton energy of ZnO is 3.377 eV at 10 K and 3.368 eV at 100 K. The dashed lines are the fitting for the data below x=0.015 at 100 K. The error bars in x indicate the full width at half maximum of the spread of the concentrations observed for a film of constant Mg concentration, while those in ΔE are the full width at half maximum of localized exciton peaks at 100 K.Graphs taken from [56].

4.4 Structural Characterization

4.4.1 Atomic Force Microscopy

The surface, although playing little to no involvement in the band bending at the buried interface can indicate the quality of the film and thus of the interface. Through atomic force microscopy (AFM) topological maps were obtained with Nanosurf NanoAFM with field of view 10 μm. This gave the best signal to noise ratio for the feature size we were observing. The AFM was used in non-contact tapping mode, with the cantilever oscillating at its resonant frequency. When it is brought near to the surface of film the van der Waals forces dampen the oscillations. This in turn is fed back to the AFM and the cantilever moves to accommodate this. This displacement is measured and gives rise to a topological map. Data processing of the topological map is line mean fitted, where the mean of each line is subtracted on a line by line basis. Roughnesss are given by the root mean square of the specified area and should only be compared to samples of the same size.

4.4.2 X-ray Diffraction

X-ray diffraction is used to determine the lattice parameters of the samples which can in turn allow us to calculate the Mg concentration, but also probes the crystalline quality of the sample. X-ray diffraction measures the lattice parameter of the sample based on Braggs law:

$$2dsin\theta = n\lambda, \tag{4.11}$$

where n is an integer value, λ is the X-ray wavelength, 2θ is the angle between the incident and diffracted X-ray and is shown in the schematic in figure 4.4 and d is the inter plane spacing. For determination of the d spacing a coupled scan is used. The scan gives the intensity of the diffracted signal versus 2θ, but ω is also changes in relation to 2θ so that $\omega = 1/2 * 2\theta +$ offset, this relationship and specified angles is explicity shown in figure 4.4. For a perfectly aligned sample this can be shortened to $2\theta = \omega$ but non idealities due to the sample as well as the holder often add an inherent offset. This $2\theta/\omega$ scan gives a series of peaks in relation to the diffraction planes. Knowing the crystalline structure of the sample

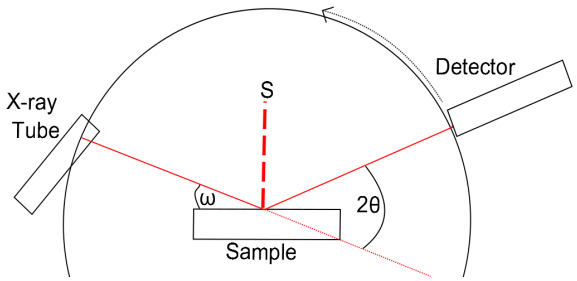

Figure 4.4: Schematic of XRD setup showing the incident ω and refracted 2θ angles relative to the beam and detector.

these peaks can be assigned to various planes depending on the parameters used during the experiment. It is seen that these peaks appear in sets where the Miller indices (hkil) are related by a scaling factor e.g. if peak (0002) is observed then (0004) and (0006) will also be observed. Some peaks are forbidden due to interaction from the reflected X-rays which cause destructive interference with other reflections. Forbidden peaks within the hexagonal geometry are h+ 2k=3n for odd l.

Once the planes are determined, an omega scan or rocking curve can be performed on a particular lattice spacing. This is used to study the crystalline quality of the overall film as well as the concentration of dislocations and defects. As there is a small lattice mismatch between the ZnO and the ZnMgO there is expected to be some induced strain which can be analyzed using this rocking curve analysis. The full width half maximum (FWHM) of the omega scan is used as a qualitative measure of the crystallinity. High resolution XRD measurements were carried out on a Rigaku Smartlab using a Ge(002) x 4 bounce analyzer. This lead the greatest precision to intensity range with a resolution of 5 arcseconds. The Bragg Brentano geometry was used for a convergent beam for greater accuracy. Cu-K alpha (λ= 1.54056A) radiation was used in these experiments.

4.4.3 X-ray Photoelectron Spectroscopy

X-ray photoelectron spectrometry (XPS) is a highly sensitive method of quantitatively observing the chemical composition of a surface to an accuracy of approximately 0.5%. Being

highly surface sensitive, with a penetration of under 3 nm, when coupled with sputtering it can also be used to give composition depth profiles of thin films. The spectra are obtained by irradiating the sample with a 400 μ m diameter beam of X-rays while concurrently measuring the kinetic energy and number of electrons that are ejected from the surface. The energy spectrum of the ejected electrons, usually plotted as the number of electrons detected vs the binding energy of the electrons detected, is a combination of the overall environment which includes the transmission characteristics of the spectrometer, energy loss processes within the sample and resonance structures that distort the electronic states of the material under analysis. There are three main types of observable peaks in the spectrum; photoelectric peaks, Auger peaks and satellite peaks. The energy of a photoelectric peak is a combination of the characteristic binding energy of the molecular component as defined by its environment and the energy of the incident X-ray. These lines are used to determine most of the chemical information of the sample and are what make XPS such a powerful technique. Due to the kinetic energy of the electrons detected being given by the relative energy of the photon energy of the X-ray source, the photoelectric peaks do not change in relation to binding energy when the source is changed. The photoelectric peaks can be assigned to specific orbitals with the atom i.e. s,p,d or f as well as being an indicator for the environment of the atom.

An Auger peak only relies on the chemical environment and the state of the molecular species it is being emitted from and therefore does not depend on the X-ray source and the peak does not move position if the source is changed in relation to kinetic energy. They occur due to collisions involved in XPS process. Molecular states can be excited above their ionisation energy. In this state there is the possibility for excess energy being emitted via a radiative process or this energy being transferred to a further electron which is subsequently ejected; this gives rise to the Auger peak intensity.

Satellite peaks originate from when a photoelectron, when exiting an atom, may interact with another electron within the same atom. This is observable in peaks with higher binding energies near the original photoelectric peak due to the transfer of energy during the collision.

The relative integral of the peaks can show the relative compositions of the elemental components. Oxygen and carbon is not taken into account in composition calculations due

to atmospheric contributions. The peak size, shape and presence of satellites can give indications of the environments experienced. The peaks are fitted via Shirley fitting and adjusted manually before CasaXPS is used to compare integrals. When looking at relative peaks, quantitative analysis is possible due to their integrals being proportional to their concentrations. Although this is the case, there needs to be a consideration for the mean free path of the electrons which is heavily dependent on their kinetic energy. As the mean free path dictates the depth of electrons that can be detected, therefore so is the volume being investigated. Due to this variation peaks are picked as close in energy as possible to keep the analysis volume similar. There are some inbuilt compensations built into CasaXPS.

The XPS used for this work is a Thermo Scientific K-Alpha instrument which utilizes a monochromated Al-K alpha X ray source (E= 1486.6eV) and achieves ultimate spectral resolution of 0.5 eV. A flood gun is used to prevent the sample from charging during the sample irradiation. The Ar milling was carried out at 3000 eV in 40 second steps giving an average step size of 10 nm (analysis from dektak). The instrument is operated using Thermo Avantage software, which allows automated execution and data processing with instrumental offsets programmed.

4.4.4 Scanning Electron Microscopy

Scanning electron micrographs were obtained on Leo 1540 XB which is a field effect emission gun scanning electron microscope (FEG-SEM). The microscopes are equipped with secondary electron-, back-scattered- and In-Lens- detectors.

4.5 Electrical Characterisation

4.5.1 Device Fabrication

After growth, thin films are subsequently cleaned in acetone, 2-propanol and deionised (DI) water and then dehydrated for 20 mins at 200°C. The sample is masked using S1805 photoresist and Hall bar geometry are patterned. The sample is milled to a depth of 200 nm leaving the mesa un-milled. The mesa is then rewashed and dehydrated and masked in photoresists

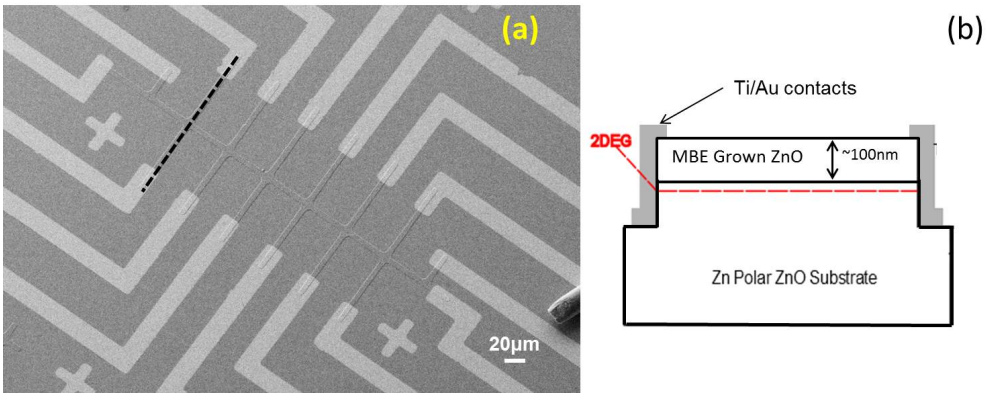

Figure 4.5: (a) SEM image of device with light contrast representing the Ti/Au contacts, and Hall bar geometry argon milled mesa in the center in similar contrast to substrate (b) schematic of cross section of device taken at dotted line on (a)

LOR10B (to ensure undercut for lift off processes) and S1805. Contacts are sputtered on Ti (8 nm) / Au (50 nm).

4.5.2 Electrical Measurements

Once the device is fabricated then resistance measurements are taken. The device is Al wire bonded to the appropriate puck and inserted into the Quntum Design Physical Poperty Measurement System (PPMS). The sample is cooled down to 2 K and 14 T longitudinal magnetic field sweeps are taken. There are possibilities for 0.35 K with a Helium 3 probe insert and magnetic field sweeps with different orientations of the device with respect to the magnetic field. The measurements are taken at 19 Hz 0.01 mA and are swept out to a maximum of 14 T.

Chapter 5

ZnMgO Growth Optimization

When depositing any thin film, the parameters that are needed to be optimised can be characterized into two categories; pre-deposition parameters involving the substrate selection and preparation, and those during the deposition involving the growth dynamics directly. This chapter will discuss both of these categories. In the first half of the chapter we will explain with the explanation of the selection of substrate and the preparation of the substrate before growth. The latter half of the chapter will give initial experimental results of growths varying temperatures, Mg fluxes and Zn fluxes, and evaluating their physical properties.

5.1 Pre-Treatment of Substrates

The substrate selection and pre-treatment are considered first. The importance of the substrate selection is non-trivial. The substrate lattice parameter relative to the ZnMgO film to be grown and the quality of the substrate, which is dictated by impurity incorporation and crystallographic defects, can heavily affect the subsequent growth of the thin film and therefore any interfaces that are held within the film itself. For the growth of ZnMgO/ZnO interfaces in this work, ZnMgO was grown directly onto Zn polar polished ZnO substrates. This minimizes the lattice mis-match between the substrate (ZnO), and the film (ZnMgO) and so creates thin films which are grown via pseudo-homoepitaxy growth dynamics [90]. Therefore the incoming flux of reactants have the same potential bonding geometries and

energies as the substrate leading to large sticking coefficients. If these were different, smaller sticking coefficients would affect the initial monolayer growth leading to rougher morphologies and inherent strain [91].

It has been shown that the preliminary *in-situ* growth of a ZnO buffer layer followed by ZnMgO can increase the mobility of the confined electrons at the interface, and therefore increase the observed mobilities [53]. This has been attributed to improvements in the crystalline quality of the ZnO at the interface. It is however important to optimize the ZnO buffer layer growth as well as the ZnMgO growth to observe such enhancements. Optimizing the ZnO growth is non trivial due to the difficulties in structural characterizations resulting from the minimal difference from the ZnO substrate - any observable differences are engulfed by the large intensity of the substrate ZnO characteristics. Therefore our work has been done with as-purchased ZnO, with pre-growth treatments, to optimize the ZnMgO fully, reducing the parameter space to be investigated. This will give us a greater understanding of the ternary component growth dynamics allowing us to fully optimize this system without any ZnO buffer layer growth.

The polarity of the ZnO was chosen to further enhance the formation of the confined electron space at the interface. It has been shown that the polarity of the ZnO can heavily effect the confined electron space [92]. C-plane ZnO is the most energetically stable plane [93], allowing for more uniform and consistent preparation of the substrate but also for subsequent device fabrication at later stages. ZnO is polar in the c-plane and can be O face or Zn face, which effects the electron accumulation at the interface as well as band energies. The O-face is smoother [94] but has a smaller electron accumulation layer and smaller magnitude of band bending as observed in modified Thomas-Fermi approximation (MTFA) calculations when the system is under atmosphere, seen in figure 5.1. There are three times fewer charge carriers at the O-face interface compared to the Zn face. As such the use O-face ZnO would hinder the formation of confined electron spaces, with electrons no longer electrostatically drawn to the surface. This is clearly seen in figure 5.1, where although these calculations are taken for atmosphere [95] with the parameters T = 300 K, $m_e^* = 0.24\ m_e$, $e_g = 8.15$ and $E_g = 3.35$ eV, differences in electron band bending can be observed, with a deeper band bending and larger

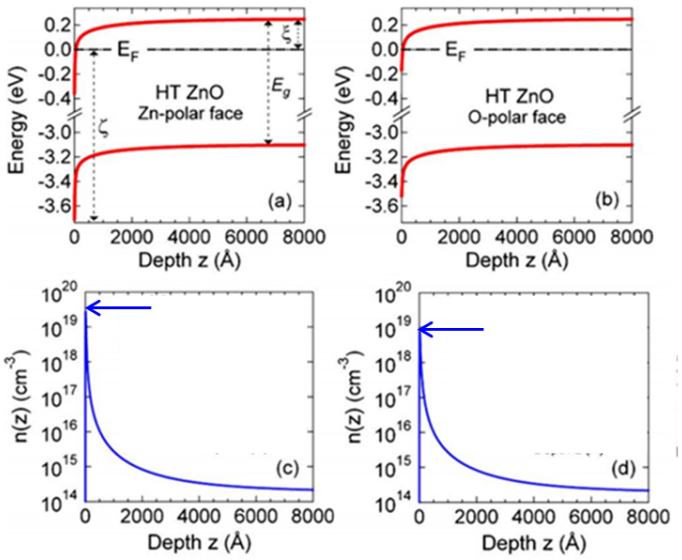

Figure 5.1: Poisson MFTA calculations of band bending and carrier concentration profiles in the electron accumulation layer in Zn polar (a and c) and O polar (b and d) for hydrothermally grown ZnO. Accumulation observed to be of the same order but three times higher for Zn faced ZnO, blue arrow used to indicate peak of accumulation. Graphs taken from [95]. Parameters for MFTA calculation given in text.

number of charge carriers for the Zn polar ZnO compared to the O polar ZnO. In normal atmospheric conditions the large electric field is compensated by surface absorbents, with a variety of mechanisms proposed[96] [97] [98]. However within the interface these charges are left uncompensated due to the difference in polarization at the ZnO/ ZnMgO interface. This leads to a large internal electric field that is desirable in the formation of confined electron spaces.

The pre-treatment of the substrate also plays a large role in the formation of confined electron spaces at the interface, especially when creating the confined electron space at the interface between the substrate and film. To ensure the growth of the thin films created are suitable for creating a confined electron space there are various prerequisites the substrate surface must satisfy. These include but are not limited to: removing all particles on the surface as well as metallic-impurity contamination; proper removal of the surface layer degraded by

surface polishing; and regulation of the surface morphology to create as close to atomically flat as possible [99].

Wet etching has provided a useful route to satisfying these requirements in other substrates such as Si wafers and RCA clean processing (Radio Corporation of America) [100] as well as other oxide substrates such as $SrTiO_3$ [101] where atomically smooth well defined substrates have been obtained before growth. This is also possible for ZnO. Due to the Zn polar face being the more stable face it is able to withstand wet etching treatment as explained via the dangling bond model [24] [102]. In this model, zinc terminated zinc oxide [0001] has a δ negative charge associated with it on the sp3 hybridized orbital. This forces the electron orbital to contract due to increased electronegativity, reducing its susceptibility to wet etching. Therefore a HCl dilution was used to pre-treat the substrate, with minimal interaction with the δ negative orbital.

Hydro-thermally grown ZnO, as used in this work, will often contain residual silica particles from the chemo-mechanical polishing. As Si is known to be a good donor in ZnO it is important to remove such impurities before growth of the ZnMgO. Highly alkaline solutions are used as standard reagents in polishing solutions. In this environment various redox reactions are know to occur with the ZnO, with the subsequent formation of $[Zn(OH_2)]$. This is known to be stable in polishing solutions (pH 10) and water (pH=7). But $[Zn(OH_2)]$ is also known to form a gel in the presence of water, [103] meaning that the Si particles are often fused to the surface and cannot be removed with aqueous solution alone. Therefore what is needed is an environment where the zeta potentials (electrokinetic potentials in colloidal solutions) for the ZnO and SiO_2 are in the same polarity to each other to prevent further particles becoming electrostatically bound to the surface. Using literature values for a positive zeta(pH$\leq$ 7 for ZnO and pH $\leq$ 4 for SiO_2 [104]) a solution of HCl (HCl : H_2O = 7:200) was formulated to give slow enough etching of the ZnO for it to be monitored to ascertain the best parameters [105].

The resulting surface morphologies for etching in this solution over different time scales were observed by AFM and are shown in figure 5.2. In figure 5.2 (a), which is the as purchased ZnO substrate, we see a number of particles on the ZnO surface. These are likely to be SiO_2

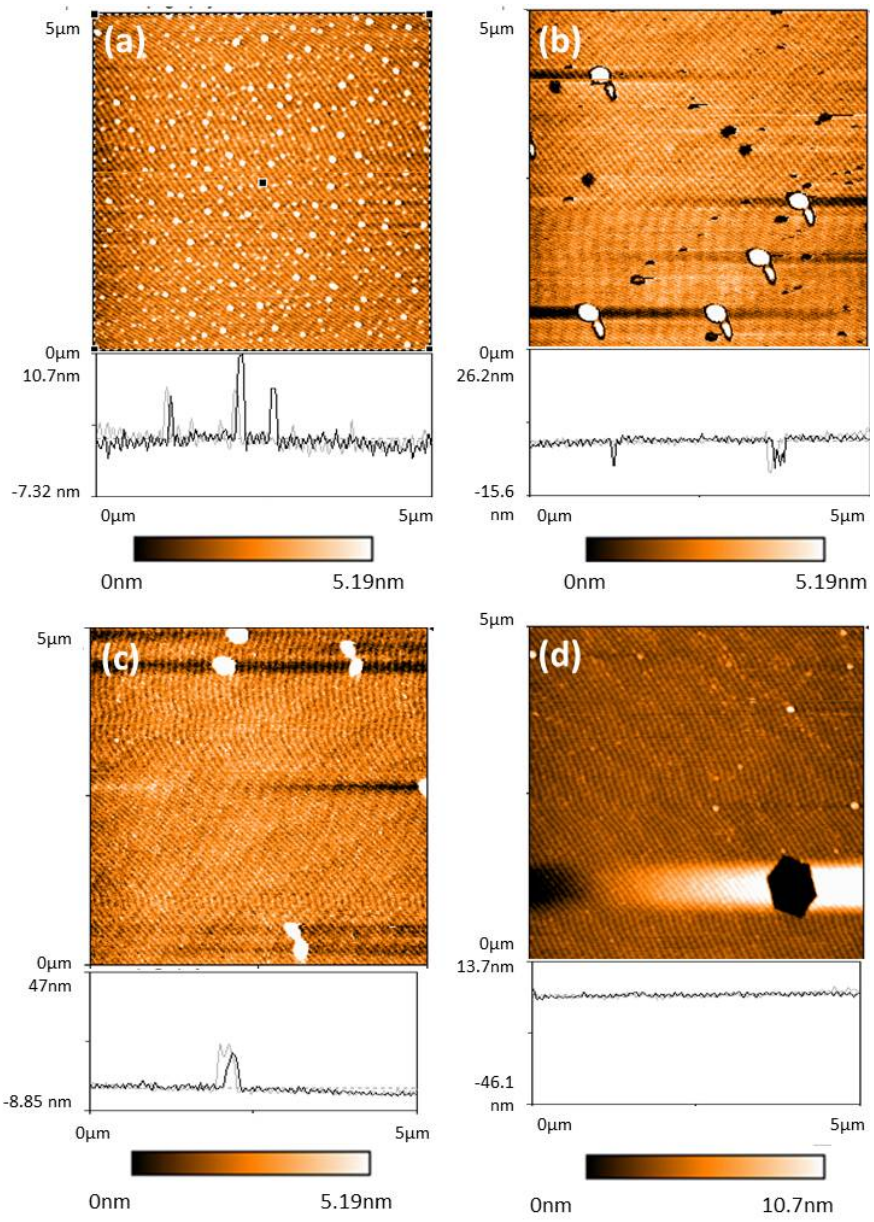

Figure 5.2: $5\mu m$ by 5 μm tapping mode AFM of ZnO substrate as received (a) and with subsequent wet etching with HCl; H_2O (7:2000) for (b) 10 seconds (c) 30 seconds (d) 60 seconds. Line scans are given for the full AFM above it. All samples were blown dry with nitrogen before imaging. Line scan taken from final scan of the AFM. 50 Hz noise observed is electrical noise, samples rotated 90 °, no rotation observed in the noise. Substrates observed to reduce in roughness from 0 to 30 seconds HCl wet etch but hexagonal pitting observed at 60 seconds.

particles arising from the electrochemical polishing. Initial etching for 10 seconds seen in figure 5.2 (b) shows a reduction of these particles. Due to the low etching rate of ZnO it is assumed that the initial pitting observed after 10 seconds was the $Zn(OH)_2$ removal with some agglomeration of the silica particles as observed in the larger particles size observed after 10 seconds. At 30 seconds, figure 5.2 (c), there appears to be terracing. Although there are still some particles remaining they are much fewer than at 0 or 10 seconds of etching. After 60 seconds there appears larger hexagonal pitting, observed in figure 5.2 (d). As already mentioned, the Zn polarity should protect the ZnO from etching, but defects in the substrate provide a route for etching to occur but at a heavily hampered rate. It has been documented that growth of Zn polar ZnO films under O rich environments can form pitting similar in geometry as the ones seen in the etchant [106]. The same principles can be applied to the etching of Zn polar ZnO as well, here also in an O environment with the lone electron pair on the oxygen in the water molecule being able to saturate the dangling bonds on the substrate providing a stabilization of the surface. But instead of growing, as seen in the literature, we are looking at preferential wet etching at the surface. With stabilization of the oxygen at the upper surface, the zinc at the corner of irregular steps are preferentially etched. Since the O termination is mobile due to the charged water molecules, the irregular step edge is stabilized so the etching propagates down to form the hexagonal pits observed here. In order to prevent large pits from forming, a 30 second etch was deemed the most appropriate for the pre-growth preparation.

There is also the possibility of heating the sample for prolonged periods of time to the growth temperature or above, to enhance surface properties. Rapid thermal annealing (RTA) allows for temperatures up to 1200° C but only for short periods of time and under atmosphere or a flow of oxygen. For temperatures below 1200°C there was a degradation of the surface as seen in the AFMs in figure 5.3 (a), at 1200°C there was a slight reduction to the surface roughness observed in figure 5.3 (b). This was not used as a base preparation due to the *ex-situ* nature of the method. This leads to the saturation of dangling bonds with contaminants from the atmosphere and also possible contamination from transfer from RTA to the MBE chamber.

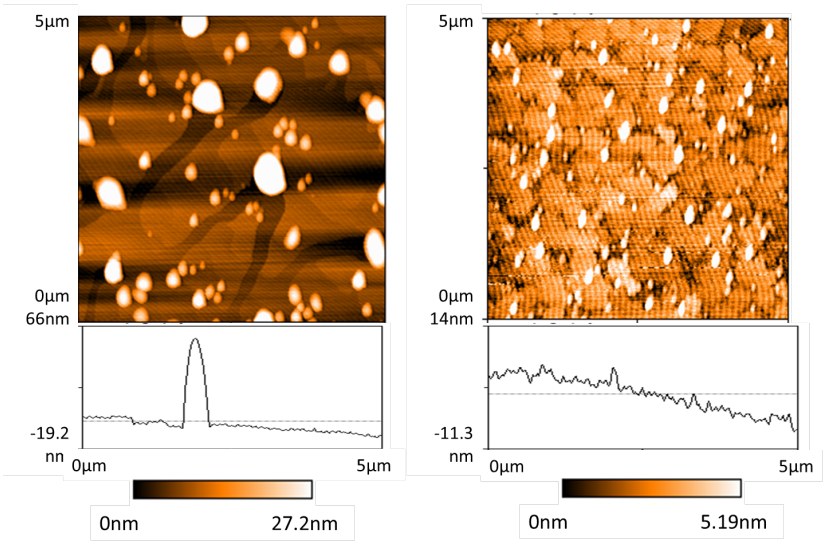

Figure 5.3: $5\mu m$ by 5 μm tapping mode AFM of the ZnO substrate post RTA at (a) 1000 °C and (b) 1200 °C. An increase in roughness is observed in (a) which is reduced in (b) but still not as smooth compared to the as received substrate. Both for 30 seconds and under a constant flow of oxygen in atmosphere. Line scan taken from final scan of the AFM

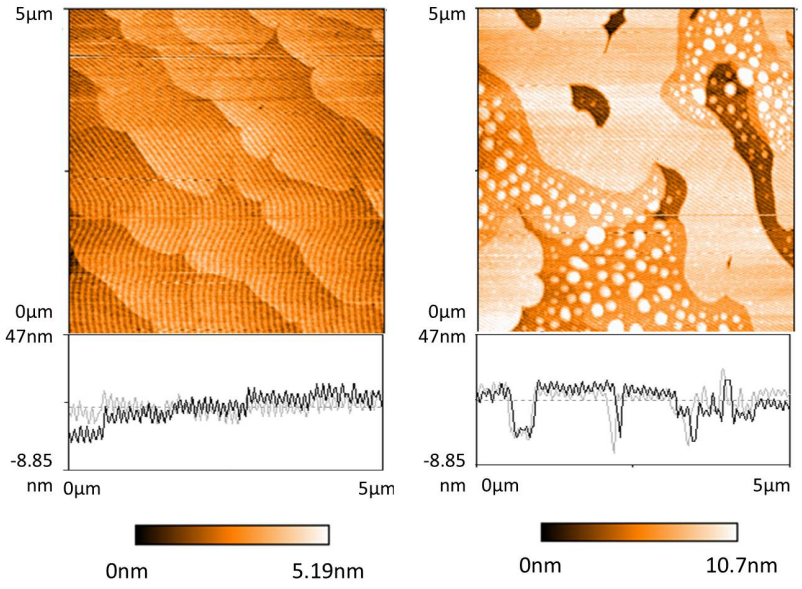

Figure 5.4: $5\mu m$ by 5 μm tapping mode AFM of the ZnO substrate as received (a) and after annealing at 900 °C under vacuum in the MBE chamber for (b) 1 hour and (c) 2 hours. Reduced roughness and terracing observed after 1 hour anneal but additional roughness is observed after 2 hours. Line scan taken from final scan of the AFM

In-situ preparation is the preferred method with the ability to relax the uncoordinated nature of the surface before growth, without compromising the crystallinity. In the MBE itself, growth temperatures of up to 900°C are possible and it can be held there for long periods of time. It was observed that between 730° C and 740°C the spectral beam spot on the RHEED increased in brightness and was more defined, as well as reconstruction being observed. This is due to the initial layer of atmospheric termination being evaporated from the sample. This is also observed through a momentary increase in pressure in the MBE chamber. Under oxygen flow the substrate is seen to increase in roughness for all temperatures. Under vacuum annealing below 800°C there was no visible change but prolonged exposure at 900°C does produce changes in the morphology of the surface, as seen in figure 5.4. In the *ex-situ* AFM it can be seen that for a substrate heated at 900°C for 1 hour there are visible terraces of 2 nm corresponding to approximately 5 unit cells of ZnO. Under thermal annealing in vacuum there is a desorption of the zinc and oxygen allowing for high surface mobility and leading to the steps observed.

With 2 hours annealing under vacuum a different morphology is observed, figure 5.4 (b). Now the surface is much rougher overall, although the islands of planar ZnO still remain with a similar roughness to the 1 hour vacuum anneal sample. With the longer anneal the substrate now follows a regime which leads to a morphology more commonly associated with Stranski Krastanov mechanism of growth but where there is a rearrangement leading to valleys of up to 50 nm. Given enough energy, the dangling bonds at the surface are able to provide an alternative pathway for migration of the atoms at the surface of the substrate, as seen in the 1 hour anneal, but with a larger degree of re-evaporation and deposition at the surface, larger morphologies are able to compete with the migration allowing for the large valley observed. This surface is not ideal for growth due to the large surface roughness.

It is also worth noting the photoluminescence (PL) after annealing. In figure 5.5, we show the PL for both annealing under a 300 W oxygen plasma delivered at 3 sccm for 45 mins (a) and under vacuum for 45 mins (b). They are in turn compared to the PL of the same substrate before the annealing process at 750 °C. The dominant peak observed here is the yellow band at about 2.2 eV. This peak is attributed to Li doping within the substrate

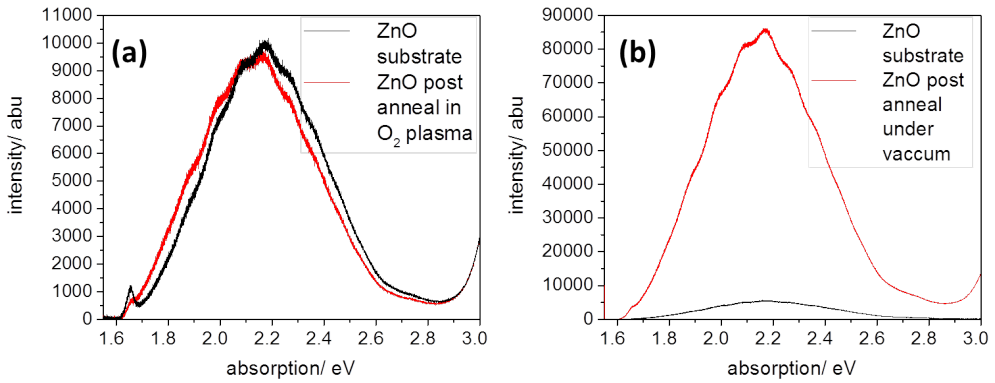

Figure 5.5: Room temperature photoluminesence spectra between 1.55 eV and 3eV (yellow band range) of ZnO substrate as received (black trace) compared with a) annealing at 750 °C under 3 sccm of oxygen plasma at 300 W and b) annealed at 750 °C under vacuum 10^{-8} Torr (both red trace), both for 45 minutes in the MBE chamber.

[107]. Li doped substrates are highly electrically resistive [108] due to the deep location of the Li acceptor level (about 0.8 eV above the valance band). The implications of this will be discussed further in chapter 6.

Under O_2 plasma it can be seen that the intensity and fine structure of the peak observed at 2.2 eV does not change in figure 5.5 (a). A different substrate, having a similar intensity of the defect peak before the anneal, shows a large increase in the intensity of the yellow band when annealed under vacuum, as shown in figure 5.5 (b). The fundamental origin of this peak are somewhat disputed but there is a growing body of work suggesting that it arises from the transitions from shallow donors to a deep acceptor with an energy level of about 0.8 eV above the top of the valence band [109] [110] and shown in the schematic in figure 5.6. With this argument it is therefore proposed that the annealing under vacuum is increasing the concentration of shallow donors at the surface of the substrate via oxygen evaporation, with the Li present acting as the deep acceptor. When annealing under oxygen plasma, there is a positive partial pressure of oxygen, therefore oxygen evaporation becomes unfavorable. Therefore the PL peak observed remains unchanged. The fine structure of the peak is caused by electron-phonon coupling with two phonon modes visable. This band has

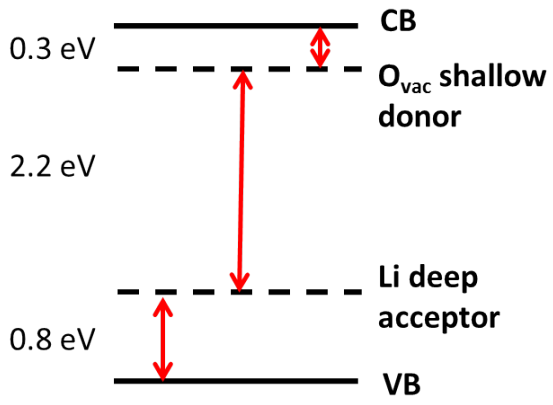

Figure 5.6: Schematic of the deep acceptor Li ions and the shallow donor oxygen vacancies in relation to the band energies of the ZnO valence band and conduction band.

been assigned to a transition from an excited state to the ground state of a CuZn acceptor [111], a common contaminant. This oxygen poor region of the ZnO would move to reduce the electron accumulation at the interface with the ZnMgO. Therefore the increase in the yellow band is seen as having a negative impact on the attempts to grow a film which demonstrates a confined electron space.

Overall the process that was deemed the best for the morphology of the subsequent films and the electrical properties was a HCl clean of the substrates and increasing the temperature to the growth temperature under vacuum before growth. This is a compromise between roughness and electron depletion at the surface.

Substrates were provided in single side polished 1 cm x 1 cm pieces. These were then mounted in a substrate holder. Throughout this work there were 4 iterations of sample holder each providing different difficulties. Initial experiments were undertaken using indium bonding to a molybdenum back plate, holder (a) in figure 5.7. This allowed for multiple samples to be loaded on a 3 inch wafer holder and also good thermal contact with the molybdenum base plate. Although the XRD and AFM show a smooth crystalline film, XPS showed that the incorporation of indium into the films was as high as 40% on the growth surface due to the low melting point of indium. Hence growth was terminated on this

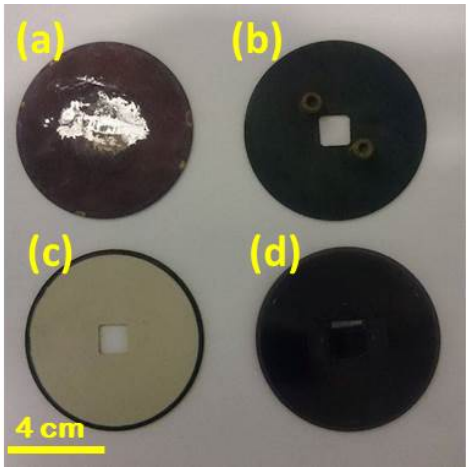

Figure 5.7: Picture of generations of holders used during this work (left to right, top to bottom) a) indium bonding b) screw attachment c) rest holder d) mounted clips

sample holder. The second iteration of the holder seen in figure 5.7 (b) removed the need for indium bonding by use of metal screws. Thermal contact was provided by 300 nm Ti backing of the sample. Although the Ti was seen to evaporate upon heating to above 500°C, the pyrometer showed no variation in the temperature and the XPS showed no measurable titanium incorporation into the films. The main problem with this sample holder was that the large screws and washers caused a thermal load on the sample causing large thermal gradients across the film resulting in a highly inhomogeneous film, reducing the amount of material that was available for device fabrication and limiting the reproducibility of the film. The third iteration, figure 5.7 (c) removed the screws and has the sample resting on the holder alone. Although this reduces the RHEED capabilities during growth due to shadowing of the RHEED electron beam, the samples are fully homogeneous allowing for larger scale device fabrication and reproducibility. This was the sample holder used for subsequent growths shown in this work. Some previous assumptions from RHEED are taken from holder 2 due to the RHEED focal point being central to the substrate. The final sample holder included small spring loaded clips to hold the sample in place, allowing for RHEED measurements, and a large molybdenum back plate for good thermal contact. Samples in chapter 7 were grown using this holder.

5.2 Growth Parameter Space

The second set of parameters which need to be optimised are those used during growth. There is a compromise during growth between the growth rate and the final roughness of the film. The roughness of the film can often be an indicator of the quality of the interface with defects creating roughness propagating through the interface and reducing the mobility of the confined electron space. If the deposition rate is lower, the impurity incorporation will be much higher, which could potentially be very detrimental to the subsequent device fabrication and electron mobilities, although the films observed at lower deposition rates are normally observed to be much smoother than those grown at a higher deposition rate. If the deposition rate is higher then there will be a larger concentration of dislocations and grain boundaries causing a larger degree of roughness but the impurity concentration will be much lower.

We can control the deposition rate by changing the incident flux of molecules and also by changing the temperature of the substrate. There is also a number of processes which may occur once a reactant is adsorbed to the substrate. The relative rates of these processes (such as surface migration, re-evaporation and deposition) are controlled by the temperature of the substrate.

Key physical properties of the films can be obtained form XRD and XPS. A full XPS spectrum is given in figure 5.8 noting the main peaks observed. From the XPS we can assign the peaks to the various elemental species present, these have been highlighted in figure 5.8 and show Mg, Zn, O and C present in the films. C is always observed due to environmental factors, and all energies are normalized against C. A Shirley background is subtracted and the Zn 2p 1/2 and Mg 1s peaks are compared in intensity to give a ratio of the peaks and therefore their relative concentrations. The environment in which the species sits can also be observed by in shift in the peak energies.

There are also capabilities to use the XPS in conjunction with *in-situ* argon milling. Here a full XPS spectrum is taken at each 10 nm milled step and the intensities of Zn and Mg compared. This gives the depth profile of the Mg concentration.

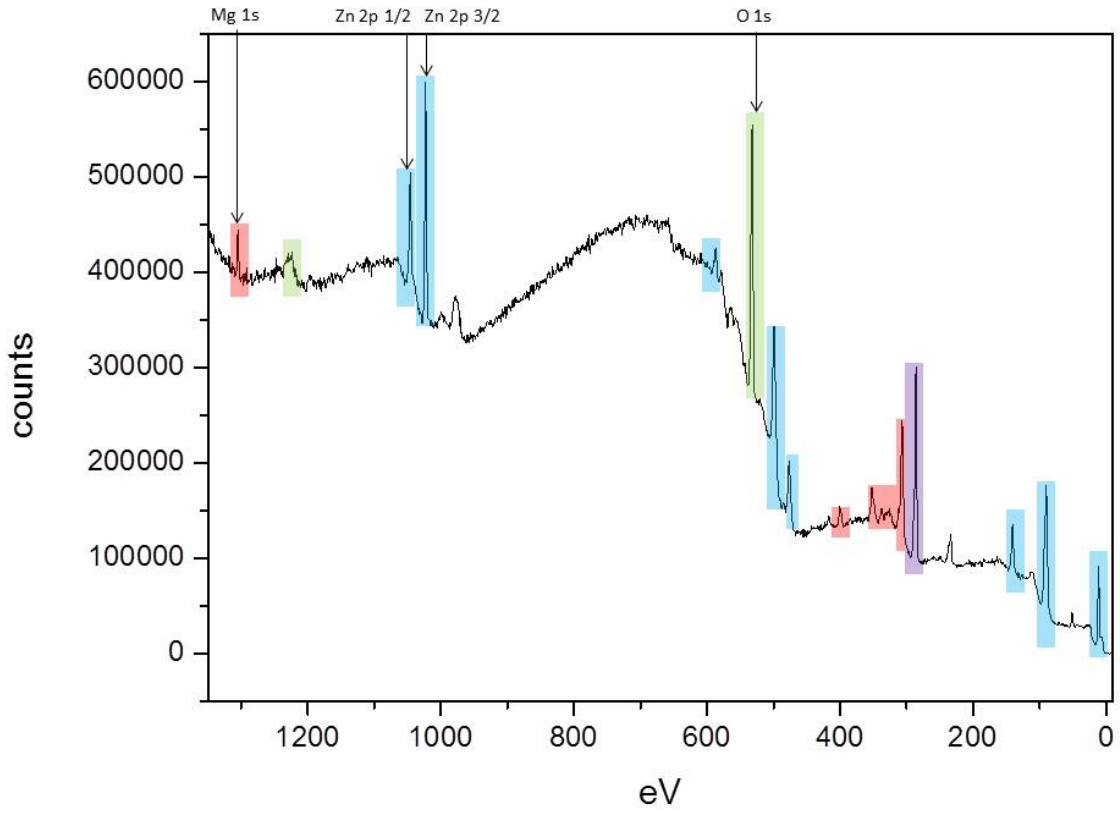

Figure 5.8: XPS full survey scan taken of ZnMgO sample grown under 3 sccm of oxygen plasma. Top surface XPS scan show a large carbon peak from atmospheric hydrocarbons on the surface indicated in purple. The color indicates the atomic species, including Auger peaks. Scan taken for 400 μ m spot size, 1 eV step size averaging 4 scans. From this survey, the Shirley background is taken and Zn and Mg peaks are compared, denoted by arrows.

The XRD full scan is shown in figure 5.9 showing clear [0002] and [0004] diffraction peaks as marked. This confirms the orientation of the supplied substrate as [0001] although the polarity can not be determined. Forbidden peaks at ZnO [0003] and [0005] are also seen in low intensities due to the two photon event therefore x-rays with half CuKα wavelength unintentionally passing through the monochromator. The inset shows the [0004] ZnO peak, [0004] ZnMgO peak at 72.5 degrees as well as thickness fringes. It can be clearly seen that the addition of Mg has increased the diffraction angle and is therefore decreasing the c lattice constant, which is what is expected in literature [112]. XRD is used to observe the lattice constants and also the crystallinity of the films grown, with subsequent omega scans used to determine the latter.

XRD and XPS will be used in the comparison of films grown with varying growth temperatures, varying Mg fluxes and varying Zn fluxes.

5.2.1 Effects of varying growth temperature

When changing temperature the balance of the competing processes of surface migration, re-evaporation and deposition, changes. This creates vastly different morphologies on the surface of the film. If the temperature is too high then the competing re-evaporation at the surface reduces the growth rate and therefore increases the probability of impurity incorporation. It also allows the system to increase the surface migration. Surface migration can be used to create a smooth interface, but on a surface with existing defects these defects can be accentuated. With a surface that has minimal defects, however, and therefore only one thermodynamic environment, this thermal energy can be used to create the most thermodynamically stable film, improving the film quality and surface structure.

Maintaining constant zinc, magnesium and oxygen BEP and varying the temperature, three films were grown each with a constant Mg concentration throughout the film, and interface of graded Mg of 40 nm thickness as ascertained by XPS with milled profile. The concentration of Mg in the film varied significantly as the temperature varied, with higher temperatures leading to higher Mg content in the film as seen in XRD measurements in figure 5.10 (a). This is due to the variation in the bond energies of the Zn-O and the Mg-O

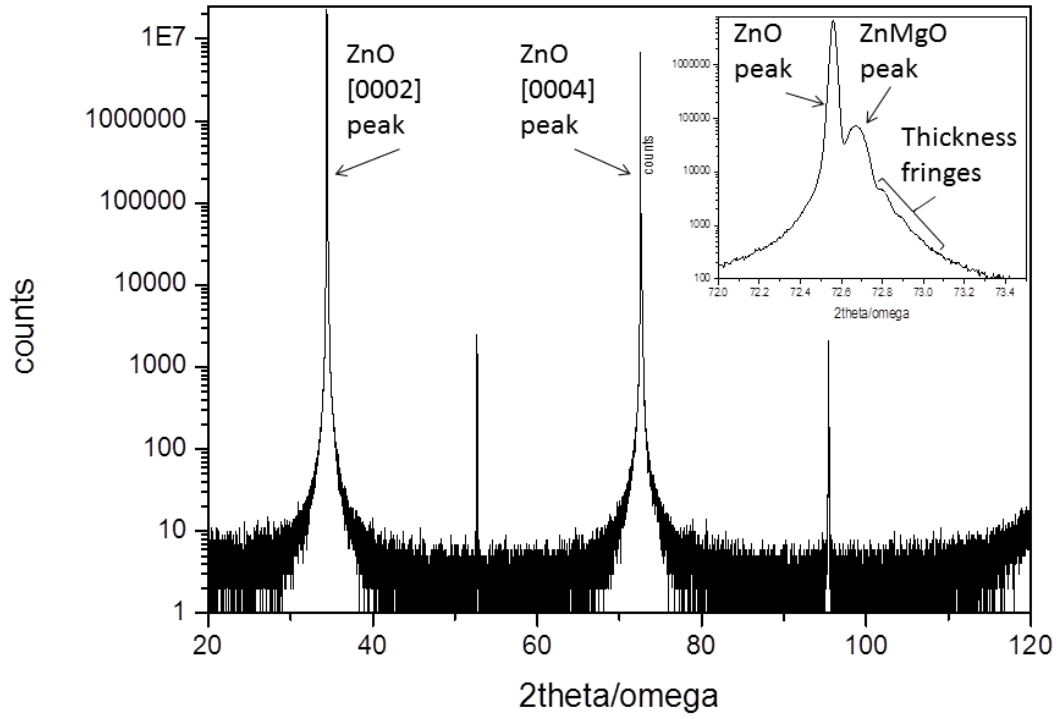

Figure 5.9: XRD of ZnMgO with steep interface. Scan from 20 to 120 degrees showing clear [0002] and [0004] peaks. Forbidden peaks at ZnO [0003] and [0005] also seen in low intensities due to half CuKα wavelength unintentionally pasing through monochromator. Inset shows [0004] ZnO peak, ZnMgO peak at 72.5 degrees as well as thickness fringes. No MgO peak is observed which would be seen at 78.6 degrees for the MgO [222] diffraction peak.

being 284.1 kJ/mol and 393.7 kJ/mol respectively at 298 K [113]. This difference leads to preferential re-evaporation of the Zn compared to the Mg. This moves towards an increase in the observed Mg concentration throughout the film as observed in XRD, with no segregation of MgO as indicated by the lack of any MgO peak in the XRD, figure 5.9. The effects are two fold from the increase in Mg. Firstly it leads to more local defects due to the variation in size of the Mg compared to the Zn therefore creating a strained lattice. It also leads to an increased degree of band bending, and changes in polarization increasing the confinement of electrons.

As previously discussed, the crystalline quality is also affected by the change in temperature. This is observed through the long range order observed in the XRD spectra. When looking solely at the [0004] peak the variations of different temperatures can be seen in figure 5.10 (b). Both the ZnO substrate peak at 72.5 degrees (which is only taken to the growth temperature with no pre- or post-anneal) and the ZnMgO peak at approximately 72.6 degrees can be seen. The substrate peak width can be seen to decrease in full width half maximum (FWHM) as the temperature increases. At 500°C the FWHM is 200 arcsecs compared to only 94 arcsecs in the 750 °C sample. This is due to the relaxation of the substrate at the increased temperature. As the substrates are mechanically polished there is some inherent strain associated with the surface due to mechanical damage. With this increase in temperature this damage is repaired through surface evaporation and surface migration. This overall relaxation and repair of the surface damage leads to a vast difference in the type of morphology we can observe at the interface and subsequent film, with the substrate now acting as a much better template for the subsequent film grown.

Another difference observed is the lack of thickness fringes on the lower temperature sample. This indicates the reduction in the long range order in the sample and therefore a reduction in the crystalline quality of the ZnMgO. This can be indicative of more impurities in the film and more defects which are detrimental to the film quality. The ZnMgO peak itself is also greatly different. At the lower temperatures it is indistinguishable from the ZnO [0004] peak. This peak was used to observe the separation due to the increased separation compared to the [0002] refraction. Since it is lower Mg content it is expected to be at a lower

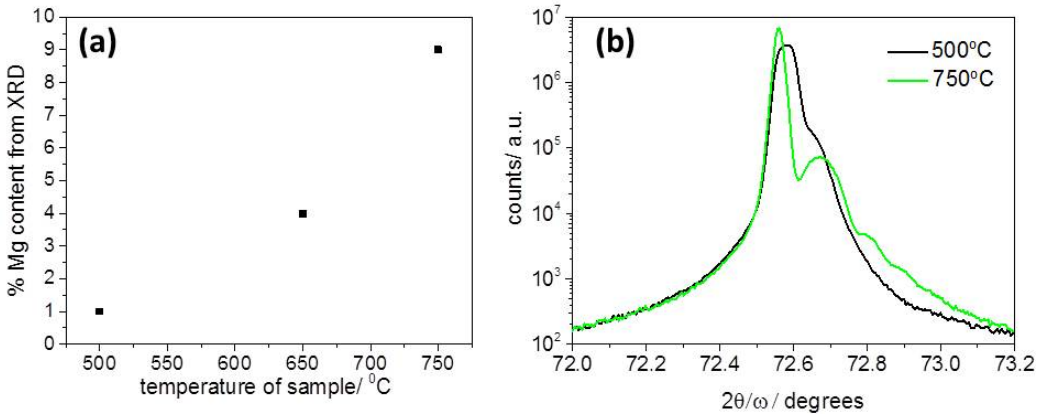

Figure 5.10: a) Mg concentration as determined by surface XRD, as growth temperature increases the % Mg is also seen to increase and b) the XRD in the (0004) direction shown at 750°C (green trace) and 500°C (black trace). Both showing ZnO (0004) peak and ZnMgO (0004) peak.

refracted angle so this is not un-expected. If the ZnMgO peak is fitted using Pseudo-Voigt Fitting, the FWHM for the sample grown at 500 °C is 340 arcsec compare with only 295 arcsec for the sample grown at 750 °C. This 15% increase in the FWHM indicates a much more crystalline film when grown at higher temperatures. This leads to lower temperatures being unsuitable for the growth of ZnMgO thin films for the observation of confined electrons.

5.2.2 Effects of varying Mg concentration

As mentioned above, the incoming beam flux is also used to determine the composition of the thin films, supplying the reactants. The Mg beam equivalent pressure is another way in which the composition of the film can be controlled.

Mg concentration remains an important variable as it dictates the degree of band bending at the ZnO and ZnMgO interface, which leads to the confinement of charge carriers which will be observed later. If there is too little Mg in the ZnMgO film, there will not be a large enough offset between the band gaps to confine the electrons and no mobility increase will be observed. There is also the fact that the screening of charged impurity scattering becomes less effective as the density of charge carriers decreases which reduces the mobility as well.

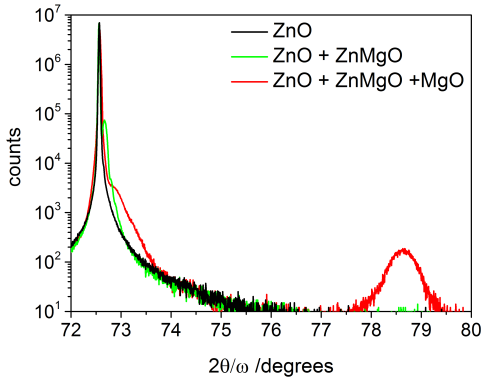

Figure 5.11: XRD of ZnO (black), ZnMgO thin film deposited from 10 % Mg flux (red) and ZnMgO + MgO thin film deposited from 15 % Mg flux (green). The peak at 72.5°is attributed to the ZnO [0004] diffraction and the peak at 78.6 °is attributed to MgO [222] diffraction.

If the Mg content is too high, the lattice mismatch at the interface will result in an increase in interface scattering. This becomes the limiting mechanism to mobility at the interface [114]. The confinement of electrons also moves towards the interface, and the interface roughness is further enhanced [115]. On the other hand it has also been shown that within confined electron spaces the increase in Mg content can increase the mobility observed due to increased band bending.

Initial investigations were carried out with a constant zinc flux (4 x 10^{-7} Torr) and temperature, varying only the Mg flux. XRD analysis showed those with Mg/Zn ratios of ≥ 0.15 had segregation into ZnMgO and MgO with three clear peaks observed in the XRD in figure 5.11; the ZnO substrate peak [0002], the ZnMgO [0002] thin film peak and the MgO [222] peak all seen in the red trace in figure 5.11. Due to this segregation causing large defects, these films would not show any confinement of the charge carriers. A discontinuity in the Mg concentration as measured by the XRD is observed in figure 5.12. This is due to the segregation of the MgO providing a relaxation route for the thin film, with less pinning to the ZnO substrate. This relaxation causes the peak to move to higher angles and the inferred % Mg increases.

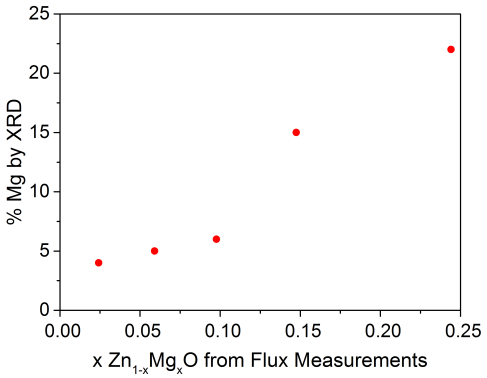

Figure 5.12: Mg incorporation determined by XRD with varying Zn:Mg ratios with constant oxygen plasma flow of 3 sccm and constant zinc flux of 4 x 10^{-7} Torr. Large increase after 0.15% Mg from flux measurements observed due to MgO segregation.

The films were also investigated via XPS. Those which had MgO segregation showed very high Mg content due to the ZnMgO and MgO in the thin film. Those with a Mg flux ratio less than 0.15 had two different growth mechanisms. Those at low Mg flux ratio only had measurable Mg in the top 20-30 nm of the film (nearest the surface to atmosphere). With surface effects dominant in this graded system, it is likely that the confinement here will be suppressed by the depletion observed back in figure 5.1. Some films show a constant Mg flux and then graded Mg concentration to the substrate, % Mg =0; the control over the graded area will be discussed more in section 5.2.3.

In the bulk, the theoretical solubility limit in wurtzite ZnO is 4% [116]. However solubilities as high as 49% have been achieved for thin films which maintain their wurtzite structure and have no MgO segregation [117]. Those reaching x=0.6 have often found MgO segregation or ZnMgO changing to the cubic phase [116]. This segregation, seen at high Mg flux, can be suppressed. Since the MgO segregation is a relaxation mechanism, it is possible with higher zinc fluxes that the system can be forced into higher Mg concentrations without segregation. By using higher zinc fluxes, the system is forced to incorporate the Mg on the wurzite lattice. We have been able to achieve concentrations as high as 57 % constant concentration for a 100 nm film on top of 70 nm graded slab in which x varies from 57 % to zero. To our knowledge

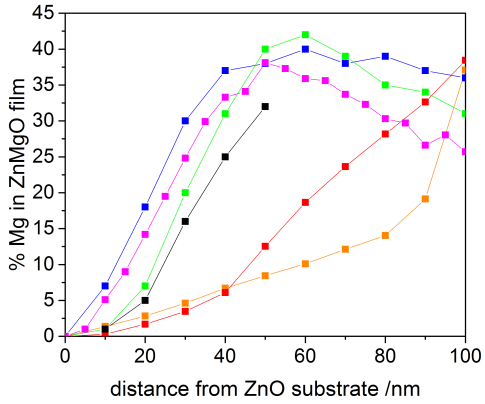

Figure 5.13: XPS mill profiles of a sample of six ZnMgO graded films. XPS spectra acquired at every 10 nm milled step. Milled step calculated from post mill profilometry

this is one of the highest Mg concentrations in ZnMgO without MgO segregation reported.

5.2.3 Growth conditions for graded systems

Although the temperature controlled crystalline quality plays a key role in the formation of confined charge carriers, the Mg concentration profile is ultimately what decides the degree of band bending and the shape of the confined electron space. The formation of a diffuse interface and the subsequent formation of the three dimensional electron slab has been extensively studied in AlGaAs/GaAs and theoretically proven with details given in chapter 2.1.3. They arise from the change in polarization in the ZnMgO graded film. To create such an electronic environment the film must have a continuously changing polarization, which can be achieved through a graded Mg content in ZnMgO films on ZnO substrates. As the polarization depends upon the Mg content we can create a continuously changing polarization by having a continuously changing Mg concentration at the interface between bulk ZnO and a ZnMgO film. As the gradient of polarization depends on the gradient of Mg, that in turn is regulated through controlling the Mg incorporation at the point of growth, we can control the electronic environment.

The formation of the graded Mg content relies heavily on the systems ability to provide

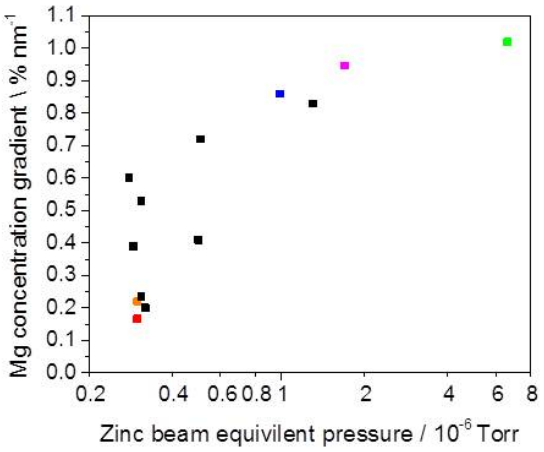

Figure 5.14: Dependence of the Mg concentration gradient near the ZnO substrate on the zinc beam-equivalent-pressure during MBE growth of the ZnMgO films. Coloured symbols correspond to the coloured plots in figure 5.13.

a route to the most thermodynamically stable state. Here we have achieved this through low zinc fluxes and therefore a lower deposition rate. With a lower deposition rate, the re-evaporation and surface migration provide a route for the system to reach an equilibrium and the film becomes lattice latched, whereby the Mg content is determined by the excess energy the system has compared to that needed to grow a lattice mismatched unit cell. Examples of these lattice latched films are given in XPS depth profiles shown in figure 5.13. The control of the gradient of the Mg incorporation can be seen in figure 5.14, with the smaller zinc fluxes creating a more diffuse graded system in the growth direction, z. The scatter in the data at low zinc flux is likely due to the substrate quality at the surface and mechanical polishing defects.

Here lattice latching is used to describe a film grown on a substrate where, due to the energetics of the growth of the film, it is preferential to grow a film with the same lattice constant as the substrate regardless of reactants reaching the surface. In this set of films shown in figure 5.13 the desired ZnMgO film is lattice latched to the ZnO, so initially ZnO or low Mg concentration ZnMgO grows. The lattice is relaxed as the film grows. This allows for gradual incorporation of Mg into the film, leading to a gradient of Mg throughout the film,

without changing any of the external parameters such as fluxes of reactants. These films are relaxed with regard to the substrate due to this growth mechanism.

The suppression of this mechanism, which leads to a less thermodynamically stable film, is realized by pushing the system into a kinetic mode of growth, by an increase in zinc flux. As more reactants are reaching the surface of the substrate there is more repulsion between the non-bonded atoms. This increases the energy of the reactants and leads to the formation of the discontinuous interface in the growth direction. As the rate of deposition is now much greater than those of both surface migration and re-evaporation, the film no longer reaches equilibrium and the film is frozen in this state. This leads to more abrupt interfaces, observed at higher zinc fluxes in figure 5.14 which would lead to a smaller confinement and a move towards a two dimensional electronic system. But due to the faster growth rates and discontinuity at the interface, the film is more strained, which could hinder the conduction through the confined electron space due to strain induced defects acting as scattering centers.

To demonstrate the difference in strain, XRD is used. In order to analyze the strain present across the interfaces, both in and out of the plane, we plot reciprocal space maps (RSMs) of two representative films, one with an Mg concentration gradient of 0.2%/nm (figure 5.15(a)) and the other with a higher Mg gradient of 1%/nm (figure 5.15(b)). In both RSMs the high intensity central point is the peak from the bulk ZnO substrate $(01\bar{1}4)$ diffraction. The RSM is centered at the ZnO peak. Variations in the absolute value of Qz and Qx for this peak arise from sample variations including curvature as well as alignment procedures. Both RSMs show an additional peak which is assigned to the $(01\bar{1}4)$ ZnMgO plane.

For the less abrupt interface the shift in Qx and Qz shows that the lattice parameter has changed both in and out of plane to that of relaxed ZnMgO. For the more abrupt interface the absence of a Qx shift shows that the in plane lattice parameter of the ZnMgO layer is the same as the underlying ZnO substrate. This means that the ZnMgO is strained in plane. The larger Qz shift is to compensate for the lack of a Qx shift and to maintain unit cell volume of ZnMgO. There is a trade off between the strain induced to create the abrupt interface and the reduction in the length scale of the graded area.

There are other advantages to the more diffuse graded system when comparing the elec-

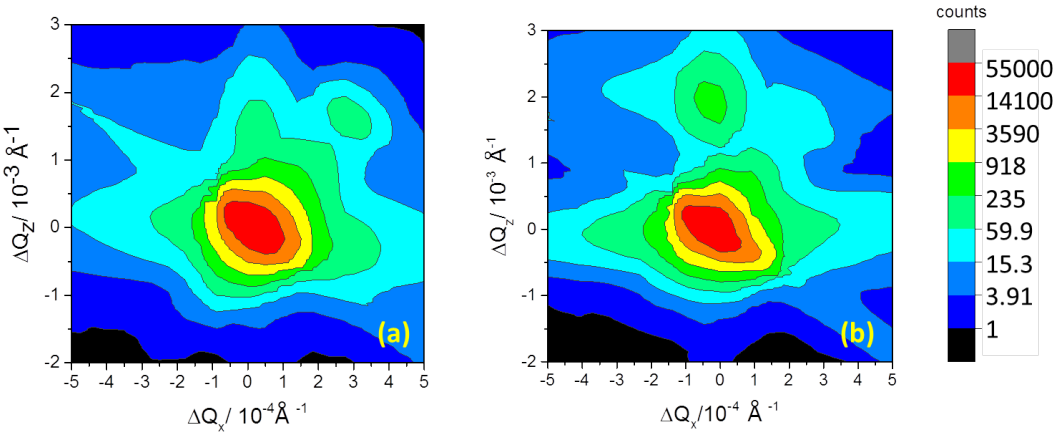

Figure 5.15: X-ray diffraction reciprocal space maps of the $(01\bar{1}4)$ reflection in films with (a) an Mg concentration gradient of $0.2\%/nm$ and (b) a higher Mg gradient of $1\%/nm$. (a) Shows two clear peaks in Qx direction, ZnO and ZnMgO, indicating the ZnMgO is relaxed in the x direction. (b) Lacks a variation in Qx for both peaks, indicating that it is strain in the x direction so that it has the same in plane lattice parameters of the ZnO substrate. Both show two clear peaks in Qz indicating the ZnO and ZnMgO variations in the z direction Both are on the same colour scale.

tronic systems. Compared to the more common 2DEG there is a more diffuse carrier concentration in the channel of conduction. This leads to a reduction in the non-equilibrium polar optical phonons which could limit high-field velocity of carriers in high density charge carriers [63]. It is also postulated that the reduction of charge carrier density will further increase the electron correlation effects, resulting in enhancements of the electron mass and spin susceptibility [64]. Even though diffuse interfaces with correspondingly diffuse confined electrons hold great possibilities there is still a limiting factor of achieving these high mobility devices so the electrons can be utilized.

It is also noted that the system can be pushed into a shallower graded system with the same fluxes if the temperature is raised. This is due to the fact that the competing, equilibrating rate of re-evaporation is again increased, forcing the system to a shallower gradient.

This is not the only mechanism by which the graded system can be achieved. Surface diffusion also plays a large role in creating a graded system. The samples also display similar error function type distribution which would be expected from thermal diffusion equation [118]. This being said, with strong links to the zinc flux and the temperature and the variations in strain, though the diffusion may play a part, we are confident that the lattice latching is playing the more dominant role.

5.3 Conclusion

In summary, initial studies into the effects of surface wet etching and pre-annealing have been done, using AFM and PL to determine the optimised parameter space. Lithium has been detected and its interaction with deep level donors discussed. Initial pre-treatment of HCl wet etch and not exceeding the growth temperature has been seen to be the best pre-treatment for the ZnO substrates.

ZnMgO films have been grown on ZnO substrates. These samples have been studied by XPS and XRD. Three mechanisms for controlling Mg concentration have been discussed. Temperature has been shown to affect the Mg incorporation and the crystallinity of the

as-grown ZnMgO thin film, with high temperature films decreasing Mg concentration while increasing crystallinity. Reducing the Mg flux during growth has a similar effect on the concentration but growth dynamics lead to surface migration of the Mg limiting the thin film Mg incorporation at low Mg concentrations.

At high Mg flux, there is seen to be MgO segregation, which has been shown to be suppressed when higher zinc fluxes are used; allowing for a strained but high concentration ZnMgO to be formed.

We have demonstrated control over the abruptness of ZnO/ZnMgO interfaces through the control of the Zn pressure. Varying these gradients affects crystallographic strain at such interfaces.

These optimizations pave the way to probe the electrical properties of the ZnMgO thin films and their interfaces.

Chapter 6

Controlling Electron Confinement with Mg Gradients

The Mg profile across an interface between ZnO to ZnMgO will ultimately determine the confinement of the electrons. A diffuse interface, where the Mg content changes gradually, can lead to a 3DES whereas at sharp interfaces, the discontinuity in both polarization and band gap cause the formation of a 2DEG.

The Mg profile across the interface is determined at the point of growth and can be controlled by the growth conditions as shown in the previous chapter. In this chapter we discuss modeling such an interface and experiments on the effects of different Mg gradients on the mobility of the subsequent confined electron space. The effect of a tilted magnetic field will also be discussed to determine the confinement. The effective mass, scattering times and mechanisms of the electron scattering will be correlated to the Mg gradients and room temperature resistance to determine the dominating scattering event.

This will not only help us understand the electronic properties of the interface but is also used as a feedback for further optimization of the growth. This was an ongoing process throughout the growth and device fabrication process, with each device providing feedback on the properties of the growth which allows us to optimize our growth further. Of the over one hundred samples grown, twenty two exhibit elevated mobilities at low temperature. Of

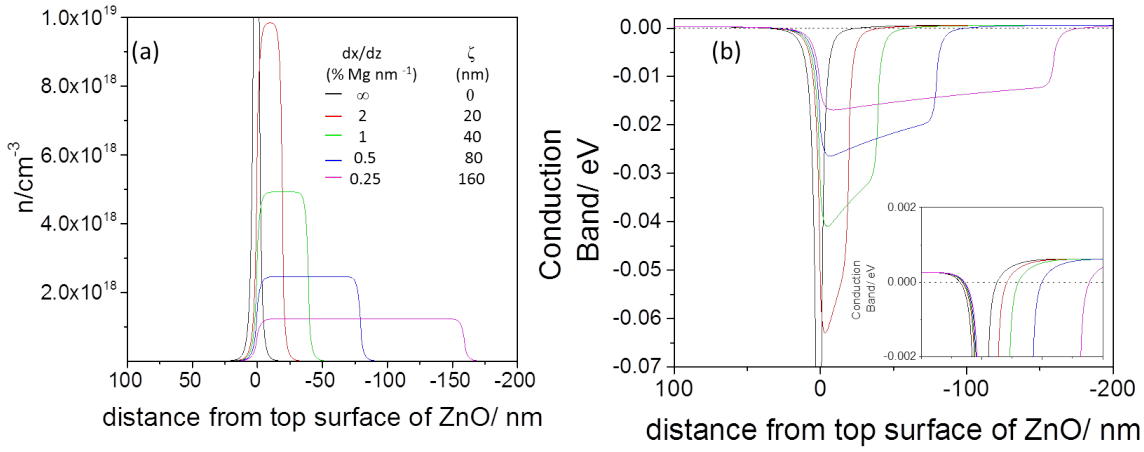

Figure 6.1: Self-consistent calculations of (a) the free electron density and (b) the conduction band edge for selected values of the Mg concentration gradient, dx/dz, in the interface region. The bulk Mg concentration for z> ζ is $x_0 = 40\%$ in all cases. The dotted line in (b) indicates the Fermi engery with the inset showing a magnified view of the offset of the bands.

these twenty two, six have a similar maximum Mg content so are compared to isolate the effects of changing the gradient of the interface. The depth profiles of these six are given in figure 5.13. These six samples are the ones used in this work in looking at the effect of changing the Mg gradient of the film and its affects on the confined electron space.

6.1 Modeling Confinement at a Diffuse Interface

First the band structure and electron concentration at a diffuse interface between two semi-infinite regions of ZnO and ZnMgO with growth direction [0001] is calculated. The region z<0 is ZnO while the interface region $0 < z < \zeta$ is ZnMgO with the Mg content x being linearly graded from zero to x_0. The region z> ζ is uniformly ZnMgO with x=x_0. Hence the diffuse interface extends from z=0 to z=ζ. The Mg concentration gradient in this region being dx/dz=x_0/ζ, as shown in figure 2.5 with theory given for the subsequent confinement.

In figure 6.1 the results of self-consistent finite element simulations of ZnO/ZnMgO interfaces performed by solving the Poisson-Schrödinger equation are presented with all constants

and reasonings for their usage given in Appendix B. The equation is solved in one dimension with an element size of 1 Å. The bulk Mg concentration at z> ζ is 40%. In figure 6.1(b) the spatial variation of the conduction-band edge for selected values of dx/dz is shown. In figure 6.1(a) the resulting electron density is shown. It can be seen that the confinement is over the same dimensions as the graded area.

At the abrupt interface (dx/dz $\rightarrow \infty$) a sharp, deep quantum well forms in the conduction band. A 2DEG is formed at the surface of the ZnO. In ZnO/ZnMgO heterostructures in-built polarization mismatch provides a confining field in addition to the built in electric field resulting from the band gap discontinuity. By contrast, for diffuse interfaces we see broader conduction-band wells. This has previously been referred to as a three dimensional electron slab (3DES) and experimentally observed in ZnO/ZnMgO [63] and other polar materials such as AlGaN/GaN [119]. It results from the continuously spatially varying lattice parameter which gives rise to a continuously changing polarization. This leads to a built-in electric field across the interface. Free charges move into the ZnMgO layer in order to compensate for the built-in field, resulting in a lower carrier density than for the abrupt interface. This type of 3DES can only exist in crystal systems where polarization engineering is possible. For diffuse interfaces a significant fraction of the carriers are located in the ZnMgO layer, unlike for abrupt interfaces. For dx/dz = 1% nm^{-1}, for example, 96% of the carriers are located in the interface region $0 < \zeta <$ z.

6.2 Low Temperature Measurements

Experimental determination of such confined electron spaces was then undertaken. Films were grown with the graded systems similar to those defined in the modeling in the previous section. Of all the films observed in figure 5.14, six had similar maximum Mg concentrations, between 30% and 40%, and so the effects of changing the length of the interface and therefore the gradient of the Mg concentration profile can be investigated. The length of the Mg incorporation graded system determines dx/dz, the spatial derivative of the magnesium concentration, x, in the growth direction, z. The graded ZnMgO varies from 100 nm in length,

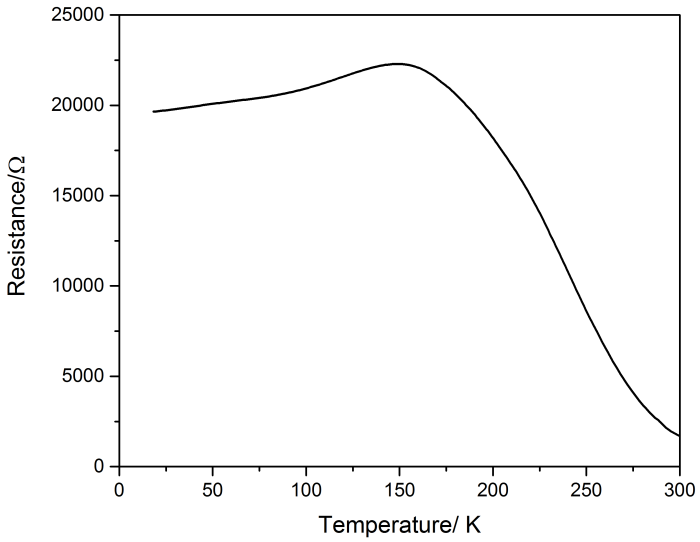

Figure 6.2: The temperature dependence of the resistance of the device for a film with mobility of 3100 $cm^2V^{-1}s^{-1}$ (green trace in the depth profile in figure 5.13). Two distinct regimes are identified $\leq$ 200 K (semiconducting region) and $200K \leq$ (2DEG region).

which corresponds to the whole grown film, a shallow gradient and small dx/dz; to only 30 nm with a larger gradient of Mg composition, large dx/dz and with a region of constant ZnMgO film observed on top. The graded area was determined by XPS mill profiles of all six films given in figure 5.13. Growth mechanisms were discussed in the previous chapter.

Devices were fabricated as per figure 4.5. These were wire bonded to a PPMS puck and cooled down to 2 K. An AC 19 Hz 0.01 mA current was applied. The temperature dependence of the resistance is shown in figure 6.2. This is a typical result for a sample with a confined electron space with there being an increase in resistance as the temperature is cooled from 300 K followed by a plateau. The initial increase in resistance is typical of semiconductors, where the charge carriers in the ZnO are frozen out giving rise to this increase in resistance. The plateau occurs when the dominating conduction is through the confined electron space. This gives first indications of confined electron behaviour in the samples. Confined electron spaces are known to have temperature independent resistance [120]. The scattering of electrons in two dimensional systems is dominated by electron scattering at low temperatures and phonon scattering at high temperature leading to minimal temperature dependence below the temperature at which electron scattering is the dominant scattering mechanism.

6.3 Observation of Shubnikov-de Haas Oscillations

All devices in the six sample set showed Shubnikov-de Haas (SdH) oscillations when the magnetic field was swept at low temperatures (<10 K), showing the presence of a confined electron space. A typical magnetic field sweep at temperatures of 2 K to 10 K is seen in figure 6.3. From the SdH oscillations, the sheet charge carrier density and mobility may be determined. The relationship between sheet carrier concentration and periodicity of the SdH oscillation is given by:

$$\Delta\left(\frac{1}{B}\right) = \frac{2e}{nh}. \tag{6.1}$$

By plotting the inverse of the applied perpendicular magnetic field, B, vs peak number (with the first peak observed in plots of longitudinal resistance versus 1/B arbitrarily assigned

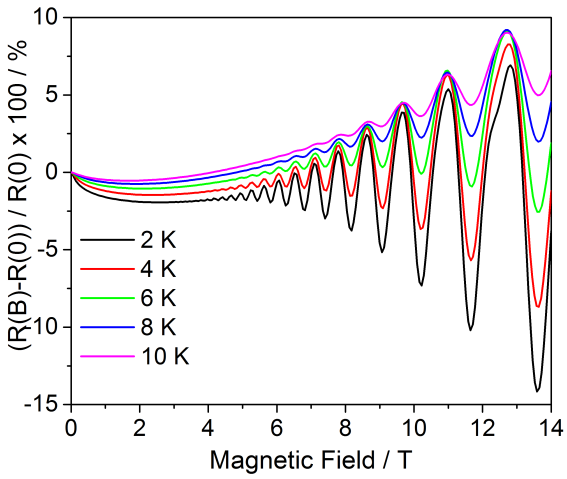

Figure 6.3: Typical SdH oscillations from a film with Mg concentration gradient 1 % nm $^{-1}$ giving a mobility of $3100 cm^2 V^{-1} s^{-1}$ at 2 K, (green trace in depth profile in figure 5.13) . Colours correspond to different temperatures at which the perpendicular field sweep was taken.

the value 1), the carrier concentration can be determined. Such a plot is shown in figure 6.4 (a) . It can be seen that there is no discernible correlation between the sheet carrier concentration and Mg gradient, dx/dz, as seen in figure 6.4 (b). There is a variation of approximately ±25% in the charge carrier concentration throughout the devices tested. This mean sheet carrier concentration of 3 x10^{12} cm^{-2} is the same order of magnitude as the model discussed in section 6.1 which gives rise to a theoretical carrier concentration of 6.3 x10^{12} cm^{-2}. There is no correlation between the Mg gradient and the calculated theoretical sheet carrier concentration as is observed in the experimental data.

The values of the sheet carrier concentration can be confirmed by the plot of Hall voltage, V_H as a function of magnetic field B using the Hall geometry within our devices, giving a linear correlation as shown in figure 6.5. The Hall coefficient is given by:

$$R_H = \frac{V_H t}{IB}, \tag{6.2}$$

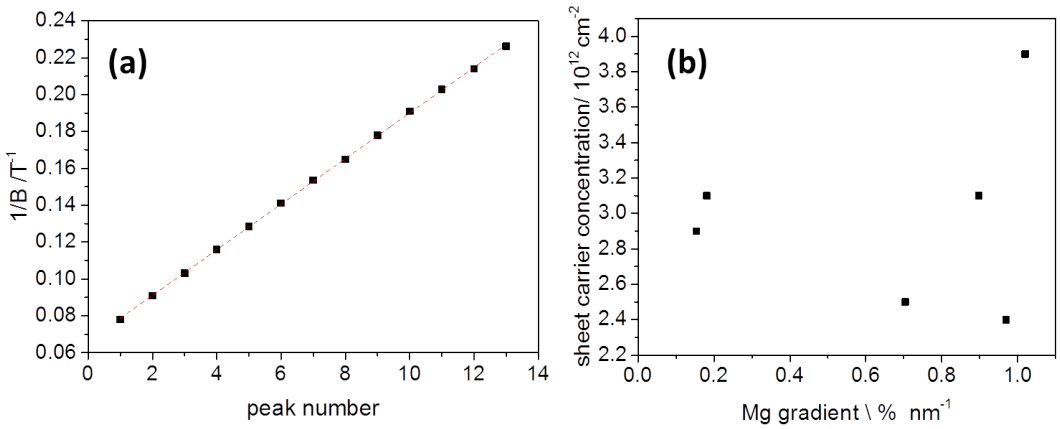

Figure 6.4: (a)1/B versus peak number for film with a mobility of 3100$cm^2V^{-1}s^{-1}$(green trace in depth profile in figure 5.13). Peak number assigned as first peak observed on 1/B vs longitudinal resistance = 1 (b) Sheet carrier concentration as a function of Mg gradient of film. All data shown for T = 2 K

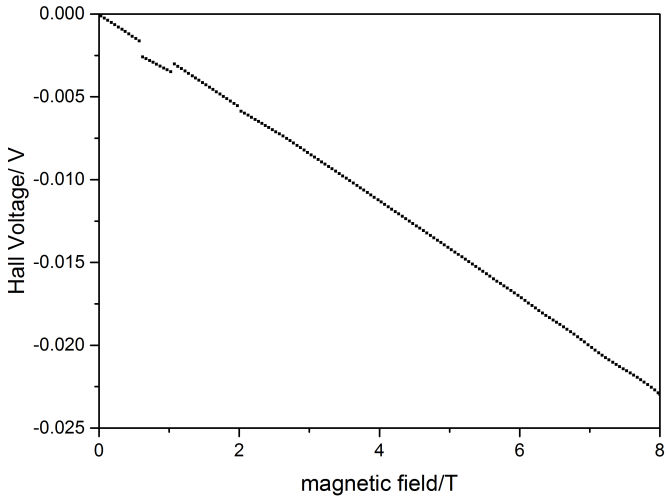

Figure 6.5: Hall voltage vs magnetic field for film with mobility 1300 $cm^2V^{-1}s^{-1}$,(orange in depth profile in figure 5.13) at 2 K.

where t is the thickness of the conductive channel and I is the current. Furthermore that:

$$R_H = -\frac{1}{n_s e}, \tag{6.3}$$

where e is the electron charge and n_s is the sheet charge carrier concentration enabling the sheet charge carrier concentration to be determined.

Of the six samples only three devices yielded Hall voltages. In these samples there is seen to be some oscillatory behavior superimposed on the linear correlation. There are two possible explications for this behavior: firstly it could be oscillatory behavior from the SdH oscillations observed in the longitudinal measurement. Those samples which did not yield Hall voltages had correlations that looked similar to that of the longitudinal resistance measurement in field, i.e. curved traces rather than the expected straight lines. This would indicate that there is the possibility for a longitudinal component in the Hall voltages with the current geometry. The second explanation is the quantum Hall effect. This gives rise to Hall plateaus, as in figure 2.6. The origins of this oscillatory behavior was examined, to determine if they are due to Hall plateaus or possible remnants of SdH oscillations.

The first derivative of the Hall voltage with respect to magnetic field was compared to that of the SdH oscillation as shown in figure 6.6. Since the maxima in the Hall voltage derivative do not occur at the same value of magnetic field as the longitudinal voltage derivative, we discount the possibility that the oscillatory transverse measurement results from the longitudinal magnetoresistance. Due to this we would then propose that there is the onset of Hall plateau type behavior within our samples.

For samples where there is no linear relationship between the Hall voltage and current, we propose that the longitudinal component is visible due to the large low temperature resistances observed, so having an effect on the Hall voltage. This a problem associated with the material electronic characteristics of the system.

In the devices where Hall voltages were successfully obtained, such as in figure 6.5 there are still some discrepancies observed. Overall there is a strong linear dependence on the magnetic field but some discontinuities are observed. The linear fit used for calculating the carrier concentrations were taken from the high magnetic field sweeps. The discontinuities

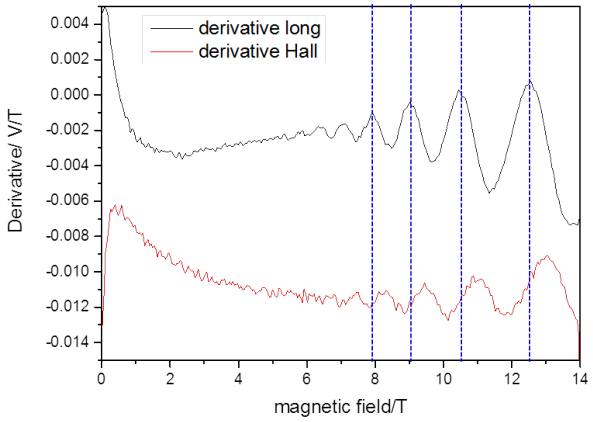

Figure 6.6: Derivative of longitudinal voltage and Hall voltage magnetic field sweeps, showing the variations in locations of these two peaks. Dashed lines show the maxima of $\partial R_{long}/\partial B$ and are given as guide to the eye. For film with mobility 1800 $cm^2V^{-1}s^{-1}$ (magenta trace in depth profile in figure 5.13)

are not reproducible and are thought to be instrumental error.

Once the carrier concentration is determined the mobility can then be determined by using:

$$\mu = \frac{1}{R_0}\frac{1}{en_sW/L}, \tag{6.4}$$

where R_0 is the resistance in zero field, W is the width of the conduction channel and L is the length of the conduction channel. This gives a mobility as high as 3,100 $cm^2V^{-1}s^{-1}$ in our sample set. This is much higher than that expected in undoped ZnO, which is reported to be 12 $cm^2V^{-1}s^{-1}$ at 2 K [121]. The temperature dependence of the ensemble mobility can also be determined by Hall voltage measurements and SdH oscillations . At low temperatures the Hall mobility is found to be temperature independent, as shown in figure 6.7. The device shown has dx/dz $\sim$ 0.2 % nm $^{-1}$ and a low temperature mobility of 1300 $cm^2V^{-1}s^{-1}$(orange trace in depth profile in figure 5.13). A maximum ensemble mobility of 2200$cm^2V^{-1}s^{-1}$ is found at $\sim$ 100 K. It has been shown that undoped ZnO has a maximum mobility between 40 K and 80 K of 2400 $cm^2V^{-1}s^{-1}$ due to polar optical scattering, deformation potentials,

piezoelectric effects and ionized impurities [121] . This value corresponds well to the maximum observed in figure 6.7, showing that at lower temperatures, the ensemble conduction has a strong element of conduction through the confined electrons, with ZnO charge carriers being frozen out.

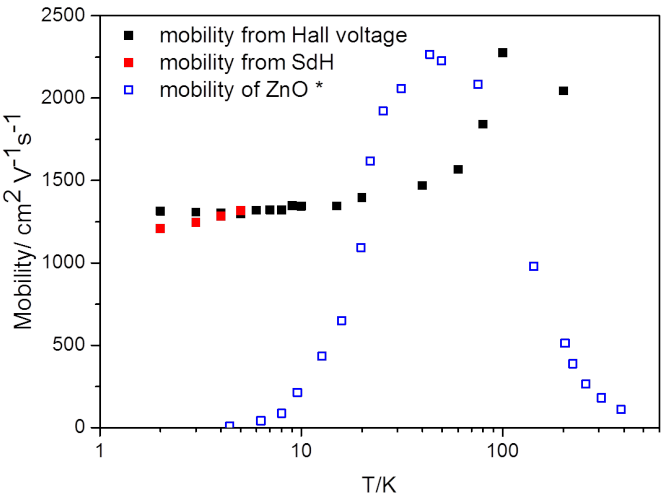

Figure 6.7: Temperature dependence of the mobility of the sample with low temperature mobility 1,300 $cm^2V^{-1}s^{-1}$ (orange trace in depth profile in figure 5.13), evaluated from Hall voltage measurements (black) and SdH oscillations (red) . * Literature values for bulk ZnO given in blue from reference [121].

The carrier concentration as determined by Hall measurements and SdH oscillations agree within ±7%, as shown in figure 6.8. The agreement of both these methods gives confidence in the obtained carrier concentration using either technique. We can conclude that at 2 K the current is essentially carried only by the confined charge carriers.

There can be seen to be a dependence of the mobility on the abruptness of the interface, with the less abrupt films giving lower mobilities, as shown in figure 6.9 (a). The reduction in the confinement width overrides the relaxation of the strain in the lattice which was seen in the x-ray reciprocal space maps in figure 5.15 . The reduction in the extent of the confined electron space increases the degree of confinement of the electrons. When there is a more

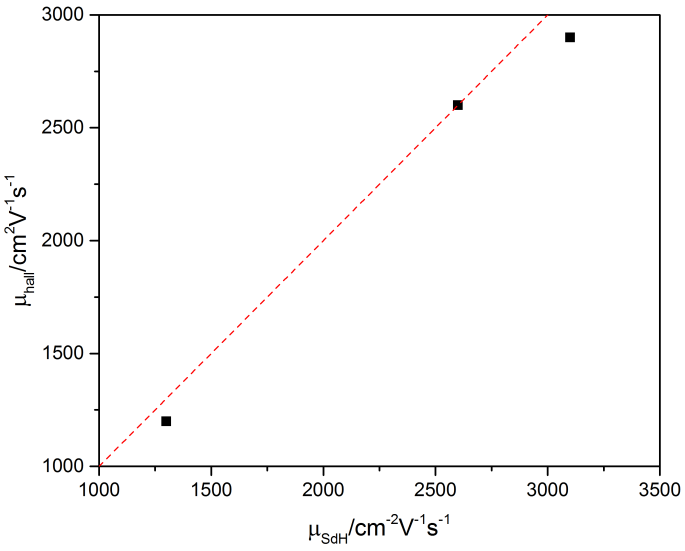

Figure 6.8: Comparison of mobility from the SdH oscillations and Hall voltage measurements at 2 K, for those devices that exhibit both.

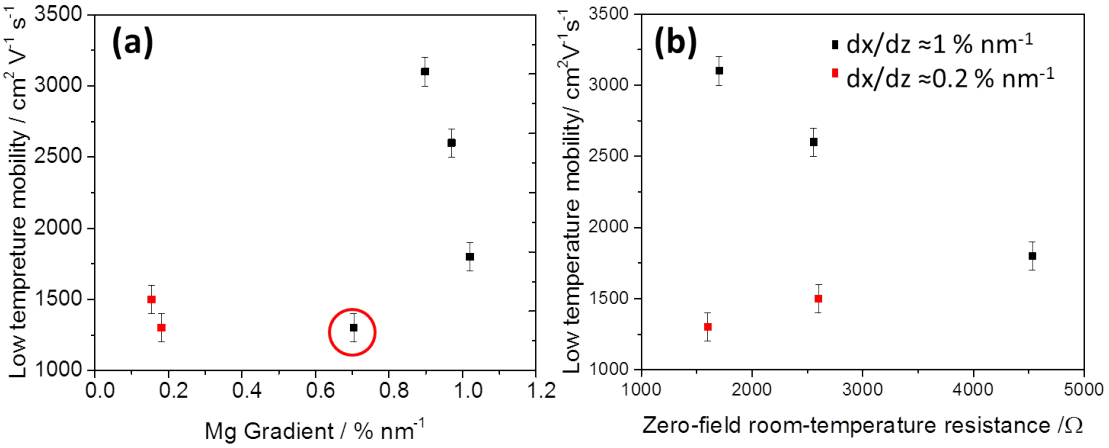

Figure 6.9: (a) Dependence of electron mobility on Mg gradients for films with 40% maximum Mg content, point circled in red indicating high room temperature resistance of substrate. (b) The dependence of mobility on room temperature substrate resistance where the two colours indicate films with steep gradient interfaces (black) and shallow gradient interfaces (red).

diffuse interface, there is a perturbation of the 2D Fermi surface allowing for more scattering therefore decreasing the observed mobility. The largest amplitude SdH oscillations were seen in the samples with the most abrupt interfaces.

The sample seen circled in red in figure 6.9 (a) has a lower than expected mobility and corresponds to the black trace in the depth profile in figure 5.13. This is proposed to be due to the substrate quality. The resistance of the device at room temperature is 40 kΩ. The room-temperature resistance is measured through the same contacts used for the low temperature transport measurements (these are configured in a geometry which is not designed for and hence does not enable the extraction of the substrate resistivity). This resistance is an order of magnitude larger than any of the other samples, suggestive of poor substrate quality. As we are growing our confined electron spaces directly at the substrate/film interface, this is detrimental to its formation. With an order of magnitude lower carrier density at room temperature in the substrate, this results in a much lower density of electrons that are able to move within the film to create the charge accumulation needed in the confined electron space. Li is proposed to be the main source of impurity in these kinds of samples, providing more defect sites for conducting electrons to scatter from and acting as a deep donor [12].

This film is also seen to be much thinner then the other films, with only 40 nm of ZnMgO thin film. This is in part due to lattice latching, which was discussed in the previous chapter. There were many samples where only surface Mg was detected due to the lattice latching previously mentioned. With only 40 nm of Mg within the film, there can also be seen to be surface effects, including surface traps and contaminant absorbents quenching the dangling bonds post growth, which would deplete the electron accumulation in the ZnMgO. The reduction in dimensionality in films with ZnMgO layer on top would generally move to higher carrier concentrations and higher mobilities, but here the reduction is detrimental to the accumulation, with surface traps playing a large part. Due to these reasons, this film was not considered in subsequent analysis.

The effect of substrate quality is highlighted further in figure 6.9 (b). Here we plot the mobility at 2 K as a function of the resistance at room temperature of the as fabricated devices, where most of the charge carriers are located in the ZnO. There is a strong trend

within the devices with steep interface gradient, (dx/dz $\sim$ 1 %/nm), shown in black. For the two red points which indicate samples with low Mg gradient, dx/dz ~ 0.2 %nm^{-1}, the mobility is limited by the degree of confinement. The black points all have similar Mg gradients so should have similar mobilities. However their mobilities vary significantly and are seen to be a function of the room temperature resistance. The room temperature conduction path is dominated by the conductive ZnO substrate and so gives us a measure of the levels of impurities in the ZnO substrate which may supress the low temperature mobilities. The black points map out a line where the mobilities are substrate limited rather than controlled by the Mg gradient.

Although there have been some attempts within this study to grow bi-layers which include a ZnO buffer layer, these have so far been unsuccessful. With 1 μm of low temperature (110 °C) ZnO grown using similar growth parameters as the ZnMgO, we observed SdH oscillations but no Hall voltage with minimal increase in the low temperature mobility. Although optimization of the ZnO buffer layer could possibly yield improvements in mobility, it has also been proposed that one of the key detrimental components is Li implantation in the hydrothermally grown ZnO substrates [6]. Li concentrations in the bare substrates have already been demonstrated by the yellow band PL observed in the substrates shown in figure 5.5. Li impurities act as a deep level acceptors. The thermal mobility of Li is high, so that even with large 1 μm buffer layers of ZnO we have not been able to prevent the diffusion of the Li throughout the sample, reducing the mobility of the samples. This has led researchers to investigate other substrates, which will be briefly discussed in chapter 8.

With a reduction in the dimensionality the average Mg concentration that each electron interacts with also is reduced, which therefore reduces the amount of scattering. By evaluating the band structure consistent with the Poisson Schrödinger equations, it can be noted that a steeper interface leads to a reduction in the average Mg concentration observed by the charge carriers and therefore less scattering of the electrons as shown in figure 6.10. Below 20 nm there is a sharp decline in the average Mg that the electron sees owing to the onset of the two dimensional character of the well as the interface moves to a more abrupt geometry and the fraction of electrons located in the ZnO increases. Although this two dimensional regime has

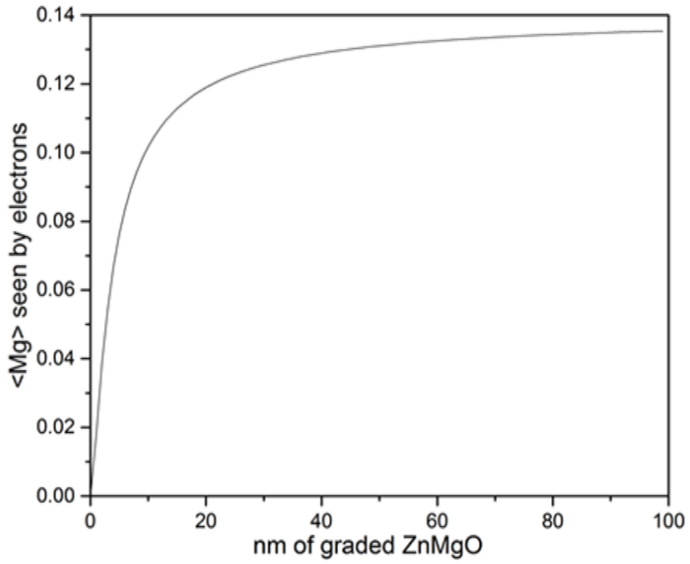

Figure 6.10: The average Mg composition observed by charge carriers as a function of the spatial extent of the ZnMgO interface. Values determined by the Poisson and Schrödinger model [122] [123] using parameters given in Appendix B.

not been reached in our samples, there is still a reduction in the Mg observed by the charge carriers, which would lead to an overall increase in the mobility.

Overall we find that the quality of substrates is of paramount importance when trying to achieve high mobilities as substrate impurities can limit the low-temperature mobility. Although the shallow gradient interface creates a more relaxed film with fewer crystal defects, the electrons are confined in a region with a larger average Mg concentration which is the dominant scattering mechanism so the mobility is reduced. The films with a larger Mg gradient have more strain yet see less Mg and are more confined so the mobilities observed are higher. It is concluded that the degree of confinement over the graded system has a greater impact on the mobility than crystal defects induced by strain, but at higher mobilities the limiting factor is substrate quality.

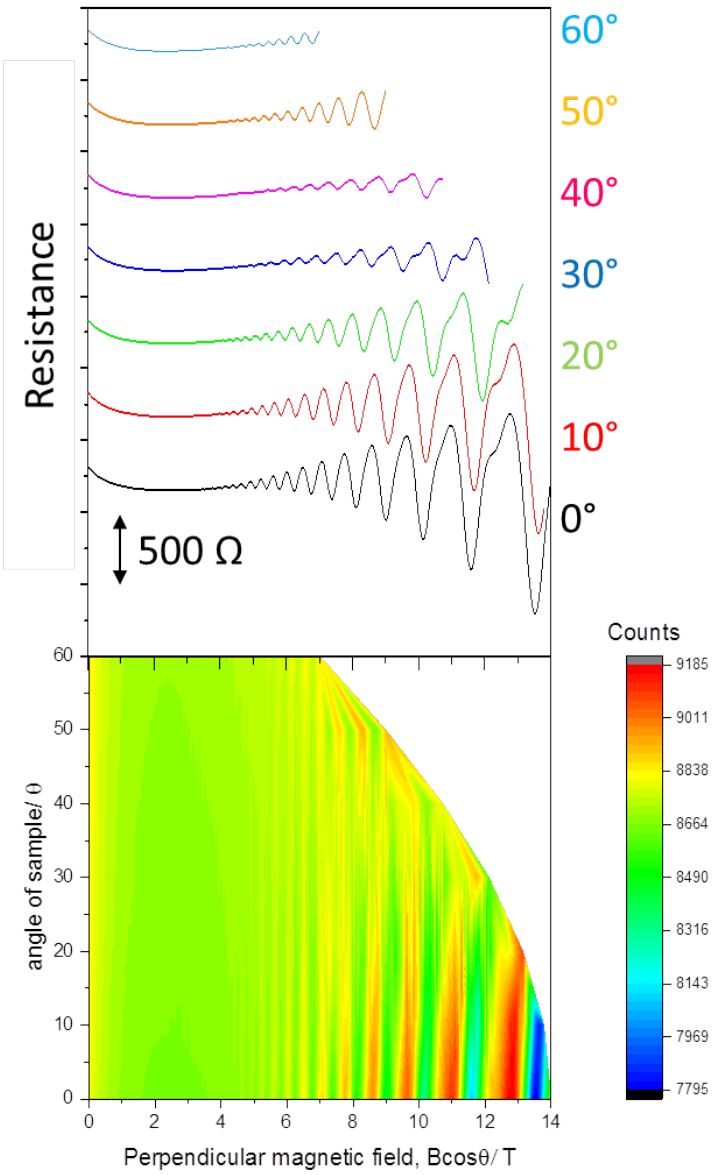

Figure 6.11: Resistance as a function of the perpendicular component of the applied field. The magnetic field is swept at 2 K, every 10 degrees. Measured for device with mobility 3100 $cm^2V^{-1}s^{-1}$(green trace in depth profile in figure 5.13) In (a) curves are offset for clarity (b) intensity map to further illustrate peak alignment.

6.4 Confirmation of Dimensionality

The dependence of the SdH oscillations upon the orientation of the applied field can also tell us much about the confined nature of the electrons at the interface. Due to the diffuse nature of the confined electron space it is important to determine whether it is defined two- or three-dimensional. This can be ascertained by the angular dependence of the oscillations. The magnetic field was tilted from 0°(perpendicular to current path) to 90°(parallel to conduction path). A typical resistance intensity map is seen in figure 6.11 (b). Only the perpendicular component of the field $Bcos\theta$ creates the quantization, so the plotted field is adjusted for this. The resistance maxima are well aligned at low tilt angles with some distortion as the angle is increased. When the magnetic field is orientated above 70 degrees there are no SdH oscillations observed. There is an emergence of a satellite peak in addition to the main peaks as shown in figure 6.12. Such satellite peaks have previously been associated with varying scattering times for the up and down spins of each Landau level [124].

Due to the nature of the confined electron space it is important to examine the Fermi surface (FS) so as to assign the dimensionality of the system. In a three dimensional case the external cross section area S_F of the FS, as seen by a magnetic field applied perpendicular to the surface is related to the SdH oscillation frequency, B_F by [125]:

$$B_F = hS_F/(2\pi)^2 e. \tag{6.5}$$

As the sample normal is tilted away from the field by angle θ the S_F seen by the field varies depending on the tilt, θ and the FS dimensionality and subsequent shape. The shape can be approximated by a tri-axial ellipsoid given by:

$$\frac{2E_f}{\hbar^2} = \frac{k_x^2}{m_x^*} + \frac{k_y^2}{m_y^*} + \frac{k_z^2}{m_z^*}. \tag{6.6}$$

Here m_x^* and m_y^* are assumed to be m^* as calculated earlier and m_z^* given as $0.24m_e$ [126]. E_f is the Fermi energy.

As the sample is tilted about an in-plane axis the external cross section seen by the magnetic field becomes [127]:

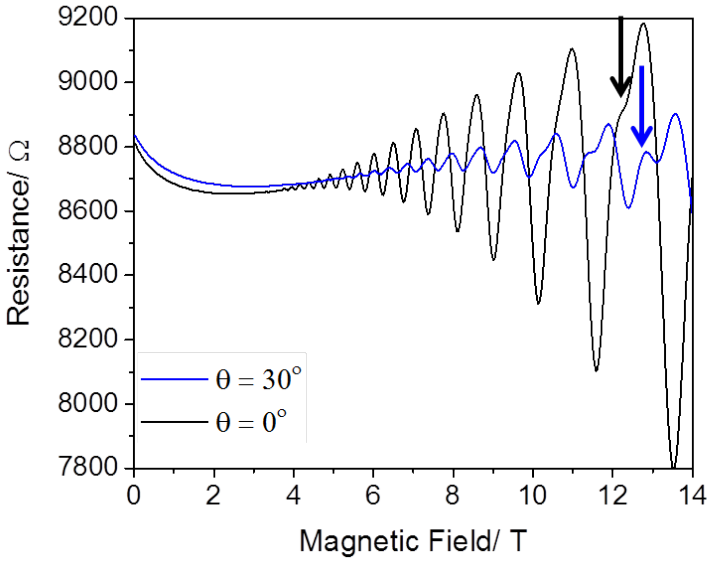

Figure 6.12: Resistance as a function of the perpendicular component of the applied field. The magnetic field is swept at 2 K. Measured for device with mobility 3100 $cm^2V^{-1}s^{-1}$(green trace in depth profile in figure 5.13.Emergence of satellite peak for field angles of 0 and 30 degrees. Satellite peak denoted with an arrow in both cases.

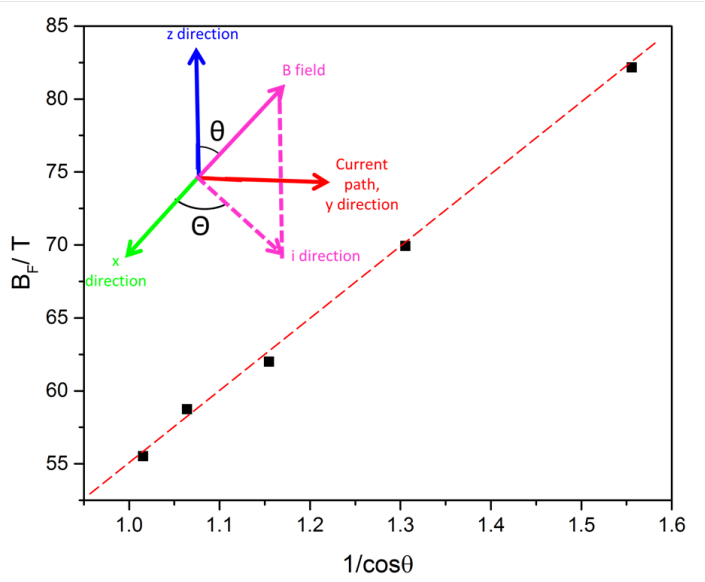

Figure 6.13: B_F as extracted from figure 6.11 (a) as a function of $1/\cos\theta$ for $\Theta = 90°$. Linear relationship indicting two dimensional transport. Inset is schematic that defines the axis and angles used in text for equation 6.7 in relation to currant path.

$$S_F = \left[\left(\frac{cos\theta}{S_{F-xy}} \right)^2 + \left(\frac{cos\theta}{S_{F-iz}} \right)^2 \right]^{-1/2}, \tag{6.7}$$

where:

$$S_{F-xy} = \frac{2\pi E}{\hbar^2} \sqrt{m_x^* m_y^*}, \tag{6.8}$$

$$S_{F-iz} = \frac{2\pi E}{\hbar^2} \sqrt{m_z^* ((cos(\Theta)^2/m_x^* + (sin(\Theta)^2/m_y^*)}, \tag{6.9}$$

are the external cross-sections in the x-y and i-z plane, respectively, and Θ is the angle in the x-y plane as defined in figure 6.13.

B_F as a function of θ is therefore:

$$B_F = B_{F-xy} \left[(cos\theta)^2 + \left(sin\theta \frac{S_{F-xy}}{S_{F-iz}}^2 \right) \right]^{-1/2}, \tag{6.10}$$

where $B_{F-xy}$is the oscillation frequency when the magnetic field is normal to the x-y plane. Therefore important information about the FS can be obtained by measuring B_F as a function of θ. This three dimensional case can be simplified to two dimensions. In the two dimensional case (S_{F-xy}=S_{F-iz}) the above equation simplifies to the FS scaling as cos(θ). Therefore B_F $\propto$ 1/cos(θ), and BF is independent of θ. This is shown explicitly in Appendix C.

As is observed in figure 6.13 there is a linear positive correlation. This gives evidence that the FS is two dimensional. With samples rotated at $\Theta = 0^\circ$ and $\Theta = 90^\circ$ giving identical oscillation frequencies, this further confirms the two dimensional nature of the confined electron space. Therefore although labeled three-dimensional, the density of states (DOS) indicated by the angular dependence of the SdH oscillation, both with no SdH observed at parallel magnetic field and $B_F \propto 1/\cos\theta$, show there is still a strong two-dimensional component. Therefore the DOS maintains its circular approximation instead of deviating to the 3D DOS of a sphere

A fast Fourier transform (FFT) was performed on the SdH oscillations at various angles, as shown in figure 6.14. The result indicates only one frequency, observed near 75 T with higher harmonics, observed due to deviations from the perfect sinusoidal in the 1/B oscillations. This implies there is only one conduction band present in the confined electron space. The

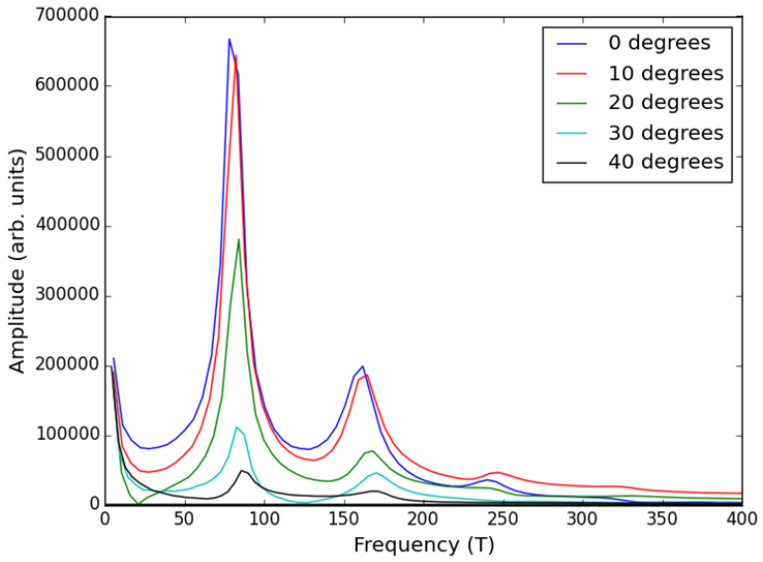

Figure 6.14: FFT of (1/B) SdH oscillations, colours correlating to different orientations of the magnetic field with respect to the current path, for a magnetic field corrected for θ.

peak is seen to move to higher frequencies as the angle is increased corresponding to a lower mobility in the x-y plane as the magnetic field is rotated, even when only the z component of the field is considered.

The damping of the magnetoresistance amplitude of the oscillations was also compared to observe any indication of the confinement dimensionality. In figure 6.15(a) the amplitude, A, is normalized to the zero tilt oscillation amplitude, A_0. The reduction in A can be seen as θ increases. Larger suppression of amplitude indicates a more confined electron space. There is no correlation observed with the Mg gradient of the films, as seen in figure 6.15 (b). This is perhaps due to the damping being dwarfed by the large magnetoresistance observed for some devices. There is however a possible correlation between the damping and the observed mobility shown in figure 6.16. This indicates that the mobility is the best measure of the electron confinement as assigned from the damping of the amplitude of the SdH.

Overall it can be seen that the angular dependence confirms a two dimensional density for states for the confined electron space while also indicating that the damping of the SdH

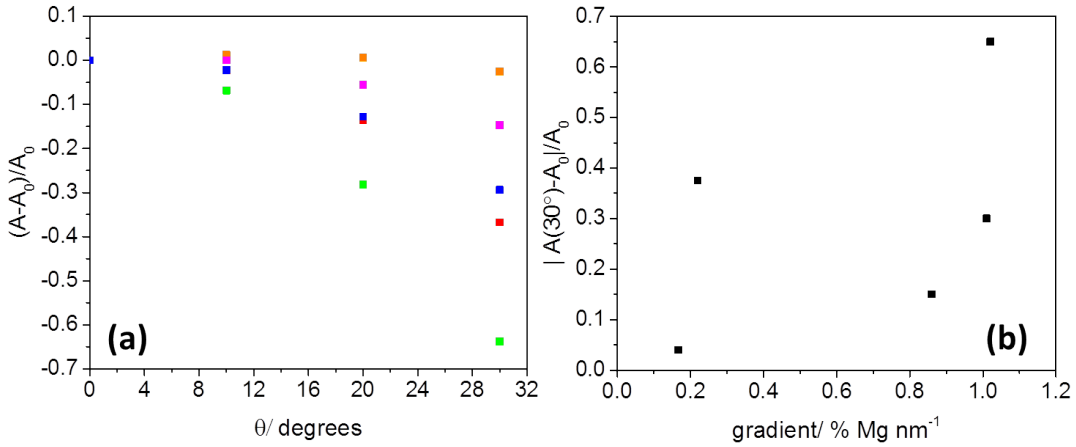

Figure 6.15: (a) Normalized SdH oscillation amplitude at approximately 11 T as a function of field angle. Colours correspond to colouration used in figure 5.13, (b) the normalized change SdH oscillation amplitude from 30 degrees to 0 degrees against gradient of the graded area of ZnMgO.

amplitude with changing the angle of the field can be used to look at the confinement of the electron space. This two dimensionality will be assumed for subsequent estimations of the scattering rate.

6.5 Classical and Quantum Scattering Rates

So far the confined electron space has been assessed in a qualitative fashion. To further understand the properties of the confined space a more quantitative approach must be taken. This can be achieved by considering electron scattering rates. In this section the classical and quantum scattering times will be determined for the set of ZnMgO films, along with the extent to which they correlate with the Mg gradient. The electron-electron scattering time will also be determined for one of the samples. By comparing the classical and quantum scattering times an indication of the dominant scattering processes can be inferred. In the latter section we show that, since the classical and quantum scattering times being similar, one scattering mechanism is seen to be dominant. In turn size effect scattering and charged dislocation

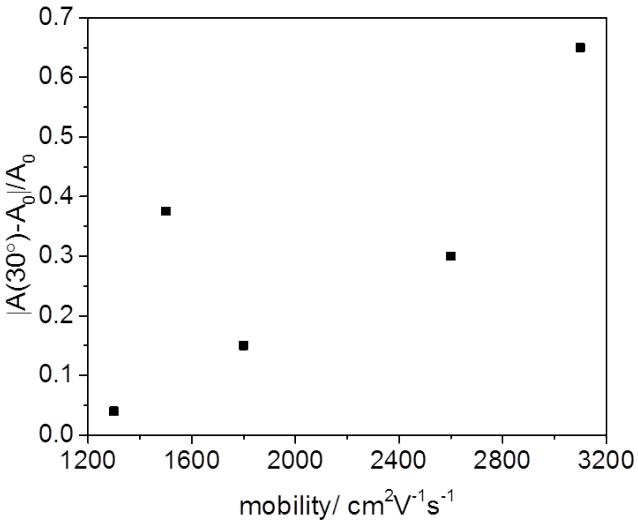

Figure 6.16: The normalized change SdH oscillation amplitude from 30 degrees to 0 degrees against the mobility of the samples.

scattering are considered before being dismissed. Alloy scattering is therefore inferred to be the dominant scattering mechanism, showing correlations with both the gradient of the Mg concentration and the room temperature resistance.

6.5.1 Classical Scattering Rate

To evaluate the classical scattering times, first the effective mass must be calculated. The effective mass takes into consideration the effect of scattering events and correlations between charge carriers. It can be extracted from the temperature dependence of the SdH oscillations. To find the effective mass, the natural logarithm of the amplitude of the SdH oscillations, A, divided by the temperature, T, is plotted as a function of temperature, figure 6.17. This is then converted to effective mass through the equation:

$$\Delta R_{xx}^{osc} \propto A = \frac{A^T}{sinhA^T} 4e^{-\pi/(\omega_c \tau_{tot})}, \tag{6.11}$$

where ΔR_{xx}^{osc} is the oscillating part of the magnetoresistance with the background removed, A^T accounts for thermal broadening at temperature T and is given by $A^T = 2\pi^2 kT/\hbar\omega_c$, ω_c is the cyclotron frequency given by $\omega_c = eB/m*$ and τ_{tot} is the total scattering lifetime. Using the approximation $sinh(\chi) \approx exp(\chi)/2$ and the derivation given in Appendix C the equation becomes [128]:

$$ln\left(\frac{A}{T}\right) = C_2 - \frac{2\pi^2 k_B T m^*}{e\hbar B}, \tag{6.12}$$

where C_2 is a temperature independent term at a constant field B. The amplitude is taken from the maximum of each peak to the next minimum, going from low to high field. This reduces the effect of the background magnetoresistance that is observed. The quoted B is given as the field at which the peak occurs.

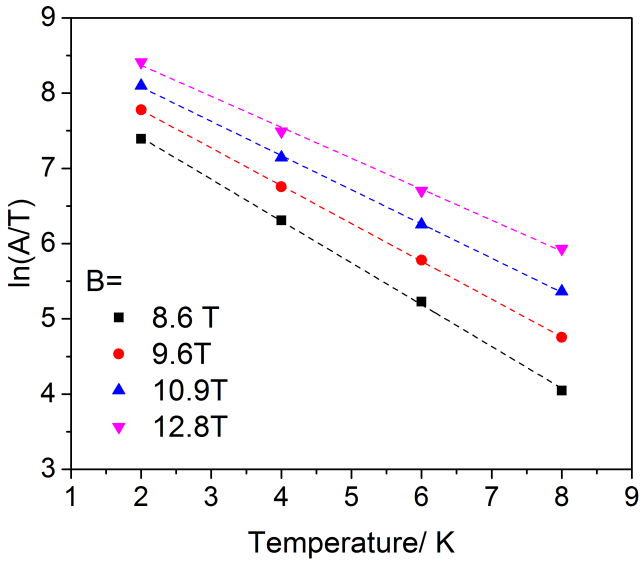

Figure 6.17: Temperature dependence of ln(A/T) and linear fits for sample with a mobility of 1,300 $cm^2V^{-1}s^{-1}$ (orange trace in depth profile in figure 5.13). Different colours represent different magnetic fields at which the SdH peaks were observed. Linear fit used for effective mass calculation shown as dashed line.

Figure 6.17, shows the correlation between ln(A/T) and temperature for peaks at various

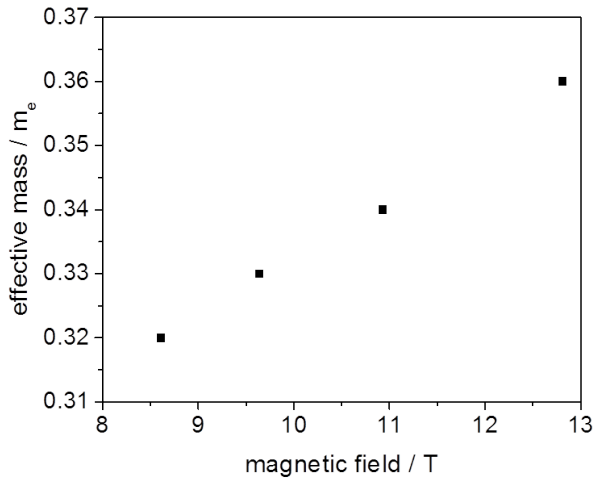

Figure 6.18: The dependence of the effective mass on the magnetic field for the sample with mobility of 3100 $cm^2V^{-1}s^{-1}$ (green trace in depth profile in figure 5.13).

fields for a given device. Measurement of the sample with the smallest change in magnetoresistance over the sweep of the field are shown for the greatest clarity and reduction in the effects of the background negative magnetoresistance. The temperature goes up to 8 K where the peaks were still discernible, and only conduction through the confined electron space is observed. The gradient of each of these sets for a particular field can then be used to extract an effective mass at that field. This is shown in figure 6.18 showing a general positive correlation with increasing effective field. Palik *et al.* predicted a linear dependence of electron effective mass on magnetic field, and therefore on the filling factor ν in GaAs, InP and InAs semiconductors [129]. The slope we observe is about 0.01 m_eT^{-1} which indicates that the effective mass has a strong dependence on the magnetic field. This mass enhancement is a consequence of the non-parabolicity of the conduction band in ZnO. An increase in magnetic field corresponds to a larger value of the wave vector in the plane of the confined electron space and an increased flattening of the E(k) curve below the sub-band because of the interaction with higher subbands.

Measurements of the effective mass from ∼8 T to ∼13 T were made for each device as in figure 6.18, and interpolation was used to extract an effective mass at a field 9 T. The

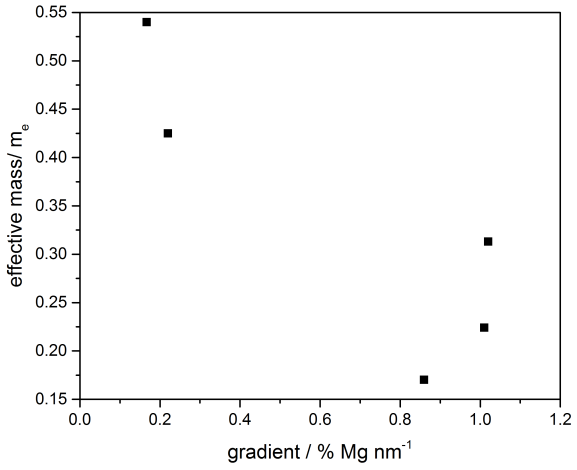

Figure 6.19: Dependence of the effective mass at 9 T, 2 K< T <8 K on the gradient of the Mg within the ZnMgO film.

extracted values for the effective mass are given in figure 6.19. Here it can be seen that with shallower gradient films there is a larger effective mass. Looking initially at the higher gradient samples, they fall in the range 0.17-0.32 m_e. This straddles the accepted range of wurtzite ZnO which is often given to be between 0.23 to 0.28 m_e (measured with field perpendicular to the current path) [130] [131]. The lower experimental effective masses could potentially be due to strain. Strain has been associated with a reduction of the effective mass due to the associated change in band gap energies [132]. This demonstrates the more confined nature of the confined electron space and also that the charge carriers are experiencing less Mg interaction as the effective mass is lower than that expected for a 30% Mg incorporation (discussed later).

When we now consider the shallower gradient the effective mass is much larger. It has been shown that the effective mass of ZnMgO is greater than that of ZnO so we first examine whether this increase of effective mass is due only to the presence of Mg and not the confinement that the arises at the interface.

The change of the effective mass perpendicular to the c-axis with the introduction of Mg has been calculated using the curvature of the dispersion relation E(k) according to:

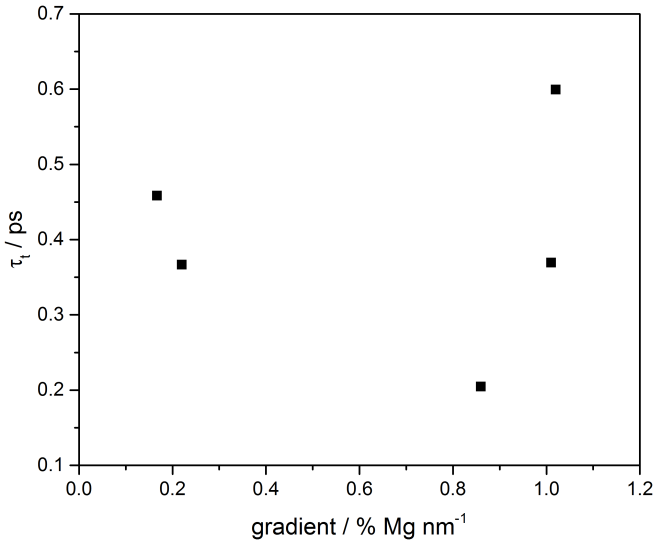

Figure 6.20: Classical scattering time τ_t at 2 K given as a function of gradient of Mg.

$$(1/m*)_{\mu\nu} = (1/\hbar^2)\frac{d^2E(k)}{dk_\mu dk_\nu}, \tag{6.13}$$

where k is the wave vector of electron in the crystal, and μ and ν are Cartesian coordinates. This gives an effective mass of ZnMgO with x_0=30% of 0.4 m_e [133]. Since both of the measured effective masses are higher for dx/dz $\sim$ 0.2 % nm^{-1}, this cannot be the only explanation, especially when the percentage of charge carriers observing the full x_0=30% is small. As the films are more relaxed and three dimensional in nature, it has been proposed that a higher effective mass is accessible through the three dimensional electron slab due to the lower charge carrier density. It has however also been observed in many systems including two dimensional systems so is seen as an effect of the low charge carrier densities in confined spaces overall [134] [135].

With the effective mass now determined, the classical scattering time can be calculated. The classical scattering time τ_t is the relaxation time from the summation of all classical scattering events such as phonon, ion and defect scattering and is related to conductivity by:

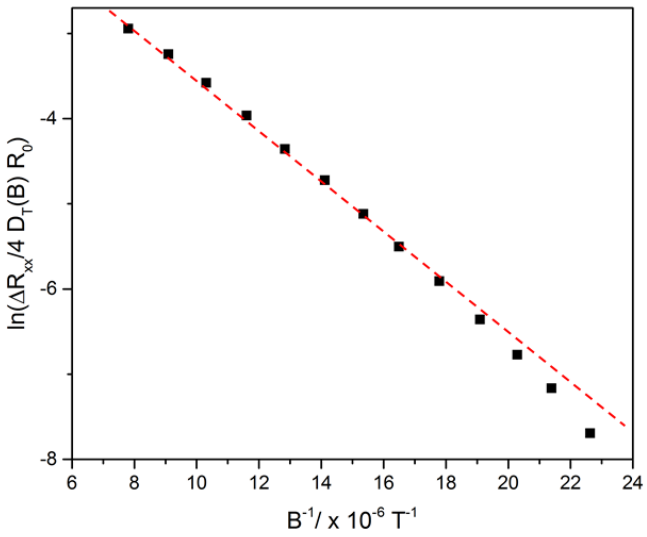

Figure 6.21: Dingle plot, used for the calculation of quantum scattering times, showing the linearity. Fitting used to give quantum scattering time τ_Q given as red dashed line. All data at 2 K.

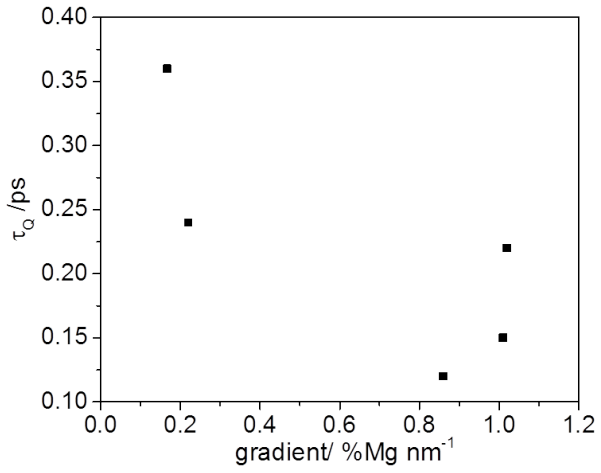

Figure 6.22: Derived quantum scattering time, τ_Q, as a function of the gradient of Mg.

$$\sigma = ne^2\tau_t/m*, \tag{6.14}$$

where σ is the conductivity, τ_t is the classical (transport) scattering time, μ is the mobility and e is the elemental charge. There is no correlation between the Mg gradient of the film and the classical scattering times, as shown in figure 6.20.

6.5.2 Quantum Scattering Times

The quantum scattering time is related to the single particle relaxation time and is a characteristic of the quantum mechanical broadening of a single particle electron state. It relates to Heisenberg's uncertainty principle $\Delta E.\Delta t \geq (1/2)\hbar$. For a confined electron state, the quantum scattering time τ_q is calculated by plotting a "Dingle plot"[136]. Here the parameter on the left hand side of the following equation is plotted against the inverse field $1/B$:

$$ln\left(\frac{\Delta R_{xx}}{4D_T(B)R_0}\right) = C_3 - \frac{\pi m^*}{e}\frac{1}{\tau_q}\frac{1}{B}, \tag{6.15}$$

where C_3 is a constant at a given temperature, T , $\Delta R_{xx}/R_0$ is the normalized amplitude of the resistance oscillations and D_T is the thermal damping factor given by:

$$D_T = \frac{2\pi k_B T/\hbar\omega_c}{sinh(2\pi k_B T/\hbar\omega_c)}, \tag{6.16}$$

where ω_c is the cyclotron frequency. This gives a straight line at high field as shown in figure 6.21. The deviation from this at low field could be due to variation in m*. As previously observed in figure 6.18 there is a lower associated effective mass at lower magnetic field, which could give rise to the non-linearity. The high-field linear nature of the plot implies there is only one conduction channel in the sample at 2 K.

The quantum scattering time, τ_Q, can be extracted from the linear fit to the Dingle plot. The dependence of τ_Q on the Mg gradient of the film, figure 6.22, shows a similar correlation to that of the effective mass shown in figure 6.19. This is expected as the effective mass is used in the calculation to determine the quantum scattering time and the mass of the particle has a large effect on the quantum relaxation of a single particle. With a larger effective mass in films with a shallower gradient there is an associated momentum which will lead to a longer relaxation time of the particle itself.

6.5.3 Electron-electron interaction

Another scattering event that occurs is between electrons themselves. This can be explicitly determined through the examination of the decreasing continuous component in the longitudinal resistance superimposed on the SdH oscillations at all magnetic field ranges. This parabolic negative magnetoresistance in the low magnetic field range, attributed to diffusive electron-electron interaction (EEI), has also been observed in GaAs/AlGaAs [137]. This is only seen for devices where the oscillations are suppressed so will be demonstrated for one sample from the set: the device with mobility 2600 $cm^2V^{-1}s^{-1}$ (blue trace in depth profile in figure 5.13).

From perturbation theory, there is a correction to the Drude conductivity (σ_0) due to EEI in the diffusion channel in the metallic regime ($E_F\tau_{ee}/\hbar > 1$) where τ_{ee} is the impurity scattering time. Then in the low temperature limit ($k_BT\tau_{ee}/\hbar < 1$) the theory predicts in 2D:

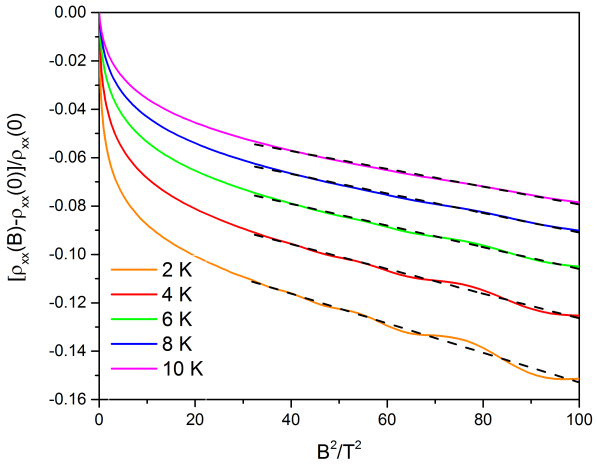

Figure 6.23: The normalized resistivity as a function of B^2 with colours corresponding to temperature for the device with mobility 2600 $cm^2V^{-1}s^{-1}$ (blue trace in depth profile in figure 5.13). The linear slope, γ, is well defined and is a function of T and the fitting is given in a dashed black line.

$$\delta\sigma_{xx}^{EEI} = -\sigma_{00}\left[4 - 3\frac{2+F}{F}ln\left(1+\frac{F}{2}\right)\right]ln\left(\frac{\hbar}{k_BT\tau_{ee}}\right), \tag{6.17}$$

where $\sigma_{00} = e^2/2\pi^2\hbar$ and F= <V(k)>/V(0) is the Hartree factor, where <V(k)> is the Fourier transform of the EEI averaged over the Fermi surface [138]. These corrections for the $\rho_{xx}^{EEI}(B)$ components of the magnetoresistance are given by [139]:

$$\rho_{xx}^{EEI}(B) = -\rho_0^2\delta\sigma_{xx}^{EEI}[1-(\omega_c\tau_0)^2], \tag{6.18}$$

where $\rho_0 = 1/\sigma_0$ is the Drude resistivity. ρ_{xx}^{EEI} is positive for low magnetic field but negative for high magnetic field. The zero of ρ_{xx}^{EEI} defines a critical magnetic field $B_0 = m*/e\tau_0$. The experimental ρ_{xx} at this magnetic field is equal to the Drude resistivity, ρ_0.

In order to check the EEI in the sample, the normalized magnetoresistance $(\rho_{xx}(B) - \rho_{xx}(0))/\rho_{xx}(0)$ is plotted as a function of B^2 in figure 6.23. The slope, defined as $\gamma(T)$ is well defined except at low magnetic field where weak localization is dominant. γ as a function

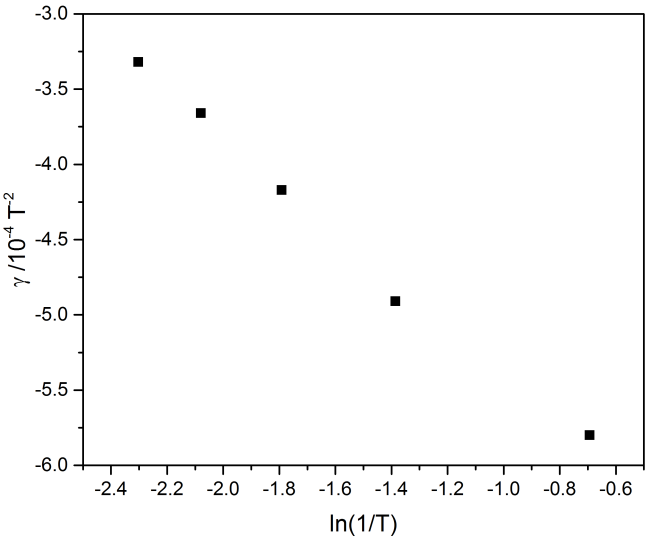

Figure 6.24: γ as extracted from the gradient of figure 6.23 as a function of ln(1/T).

of ln(1/T) is then plotted in figure 6.24. From this slope using equations 6.17 and 6.18 we obtain the impurity scattering time τ_{ee}, which is 0.085 ps for this given sample.

The term ρ_{xx} shows parabolic negative dependence on the magnetic field and the γ a temperature dependence over the whole magnetic field range. This dependence allows us to assign the magnetoresistance to EEI in the diffusive transport regime given by $k_B T\tau/\hbar < 1$ [140].

6.6 Determination of Scattering Mechanism

Determining where the scattering is originating from is important when looking into mechanisms for improving interface mobilities. The ratio of the classical and quantum scattering times can be very telling of the dominant mechanism of the confined electron space. τ_t can be quite different from τ_Q depending on the angular weighting of the scattering event. It is seen in figure 6.25 that there is a correlation between τ_t/τ_Q and the % Mg nm^{-1} gradient. Here it is seen that films with a more abrupt interface have a more dominant quantum scat-

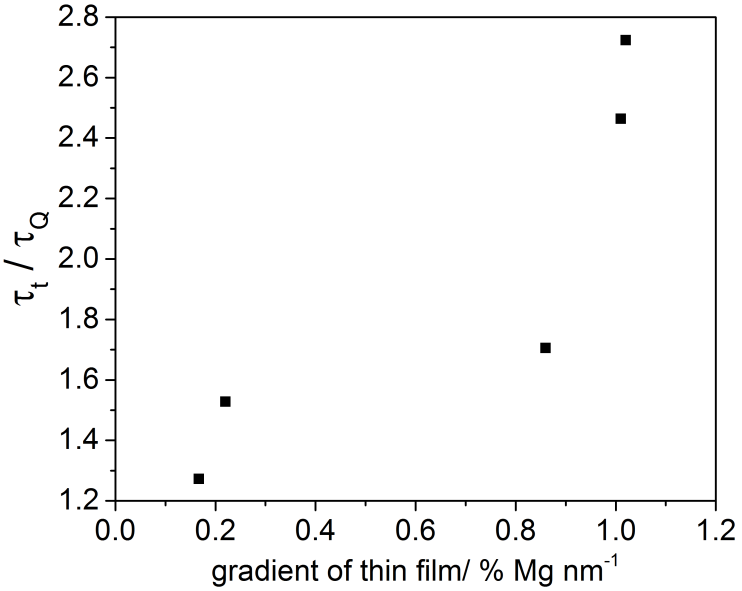

Figure 6.25: Ratio of τ_q to τ_t, both at 2 K, to the gradient of the Mg in the ZnMgO film.

tering rate. For the more confined space, the correlations between charge carriers are more pronounced leading to smaller effective masses, which in turn leads to the smaller quantum scattering times seen here. With this being said all the values fall into the category that would be classed around 10^0 [141] therefore eliminating the possibility of remote ionized impurity scattering (which strongly favors small angle scattering) as the dominant scattering mechanism. This would indicate that the dominant scattering mechanism is short order, long range; although caution has to be applied, as discussed by Hsu and Walukiewicz [142]. In their work they proposed that it is possible to have a ratio close to unity if the mechanisms by which the classical and quantum scattering occur are different. With this being the case we will now discuss three of the most common mechanisms: size effect, charged dislocation and alloy disorder. With the first two of these not proving dominant, the last is discussed as a possible candidate, shown by the correlation with Mg concentration. Finally the effects of other possible impurities, such as Li in the substrate, is discussed.

6.6.1 Size effect scattering

First we consider size effect scattering. This is because at low temperatures both acoustic and optical phonon modes of scattering are frozen out. Size effect scattering occurs if the width of the confined electron space is much less than the mean free path of the charge carrier (λ). This is given by [143]:

$$\lambda = \hbar k_F \mu / e, \tag{6.19}$$

where k_F is the Fermi wave vector in a 2D system given by $k_F = (2\pi n)^{1/2}$. When this is plotted against the Mg gradient it can be seen that the samples fall on either side of the relevancy line, as seen in figure 6.26. In the shallow graded system the mean free path is smaller than the size of the graded system so size effect scattering can be ignored. The steeper graded systems do have a mean free path that is longer then the dimensionality of the confined space itself. This indicates that there is a degree of size effect scattering in the space, but since they are on the same order this is not deemed the dominating scattering effect.

6.6.2 Charged Dislocation Scattering

Next we consider scattering off charged dislocations. The ratio of classical to quantum scattering times due to charged dislocations is still under research. Look [144] has determined the classical scattering time due to charged dislocations and applied it to explain the mobility of bulk doped GaN. The ratio of classical to quantum scattering times due to charged dislocations in a confined electron space is given by [145]:

$$\frac{\tau^c_{disl}}{\tau^q_{disl}} = 1 + 2k_F^2 \lambda_{TF}^2, \tag{6.20}$$

where k_F is the Fermi wave vector and $\lambda_{TF}^2 = 2\epsilon E_F / 3e^2 n$ is the Thomas-Fermi screening length. Here n is the sheet carrier concentration, ϵ is the permittivity and $E_F = \hbar^2 k_F / 2m*$ is the Fermi energy. The values calculated do not correlate with the measured values and the calculated values are much bigger in most cases as seen in figure 6.27. When comparing

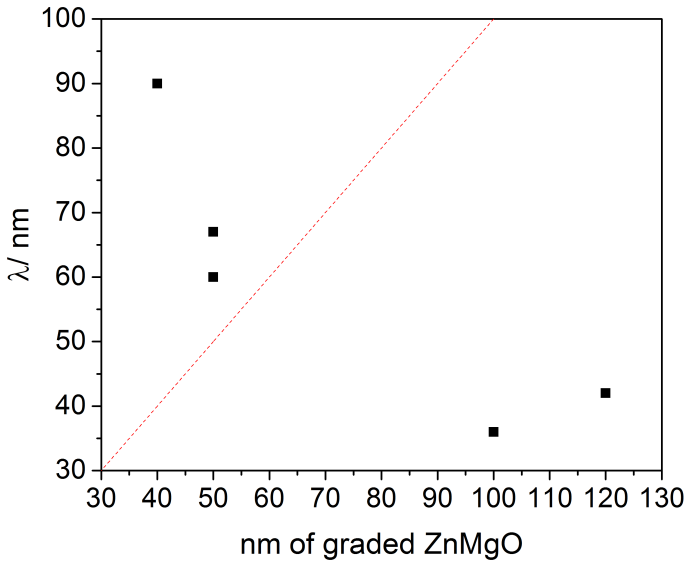

Figure 6.26: Mean free path of charge carriers λ as a function of the spatial extent, ζ, of the graded Mg region. Red line indicates $\lambda = \zeta$.

this dislocation model compared to the impurity scattering model [146] the magnitude of $2k_F\lambda_{TF}$, and therefore the ratio of scattering times, is much larger for dislocation scattering than for alloy scattering since dislocation scattering is inherently more anisotropic than impurity scattering. The impurity scattering potential of point charges is seen to be spherical in symmetry whereas the dislocation scattering potential of a line charge is cylindrical in symmetric, thus causing an additional anisotropy in the scattering of charge carriers.

Due to this being the case, dislocation scattering is not thought to be the dominant scattering mechanism but instead alloy scattering. The quantum and classical scattering rates are of the same magnitude since the scattering potential V_0 is of short range nature which makes the scattering process independent of angle.

6.6.3 Alloy Disorder Scattering

With size effect and charged dislocation scattering deemed not to be the dominant effect, a likely candidate is alloy disorder scattering. The scattering rates due to alloy disorder with

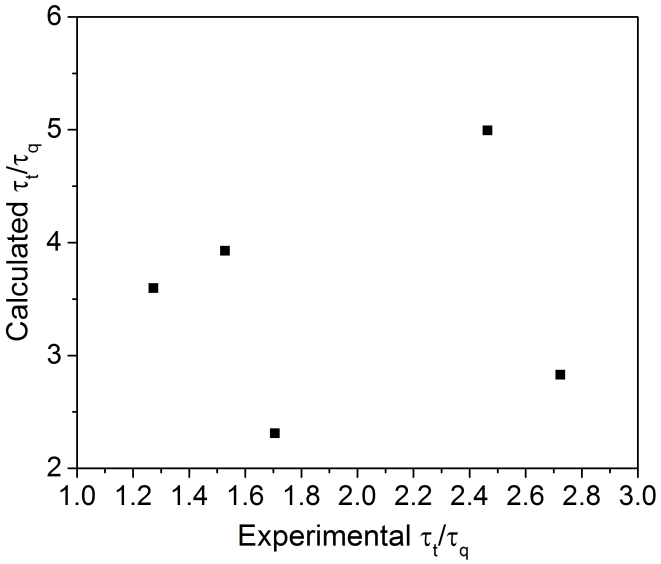

Figure 6.27: Calculated τ_T/τ_Q from equation 6.20 where the dominant scattering mechanism is assumed to be from charged dislocations vs the actual experimental ratio of the classical and quantum scattering times.

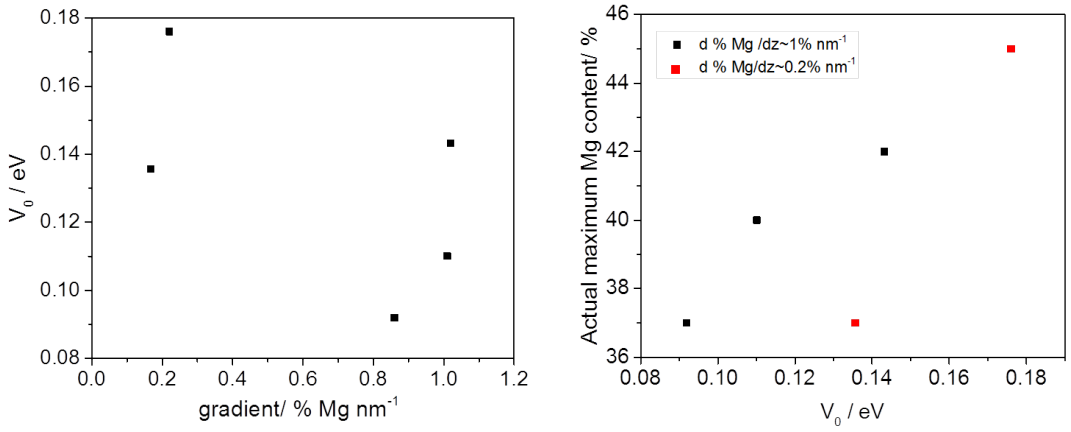

Figure 6.28: (a) Calculated V_0, assuming alloy disorder scattering dominant scattering mechanism, showing no correlation to the Mg gradient. (b) The calculated V_0 showing a strong correlation with the actual maximum value of % Mg as taken from XPS depth milling. The different gradients are shown in black dz/dx 1% nm $^{-1}$. and red dz/dx 0.2 % nm $^{-1}$

short range potential have been shown to be governed by [147]:

$$\frac{1}{\tau_{alloy}(k)} = \frac{2\pi}{\hbar} V_0^2 \Omega(x) x(1-x) g(\epsilon_k), \tag{6.21}$$

where $\Omega(x)$ is the alloy composition-dependent volume of the unit cell over which the alloy scattering potential V_0 is effective and the x is the alloy composition. $g(\epsilon_k)$ is the density of states (DOS). Only carriers with wave vectors close to $k = k_F$ are considered to contribute to the transport at low temperatures, therefore the scattering can be evaluated at the Fermi energy $\tau^{-1}_{alloy} = \tau^{-1}_{alloy}(\epsilon_F)$. The spatial average of the scattering rate is given by:

$$\left\langle \tau^{-1}_{alloy} \right\rangle = \frac{1}{x_0} \int_0^{x_0} \tau^{-1}_{alloy}(x) dx, \tag{6.22}$$

where x_0 is the alloy composition at the edge of the confined electronic slab. From this one can determine the alloy scattering potential corresponding to the measured mobilities and scattering times previously extracted as shown in figure 6.28 (a).

With x_0 approximately 0.13 for all interfaces within this given set (see figure 6.10) the

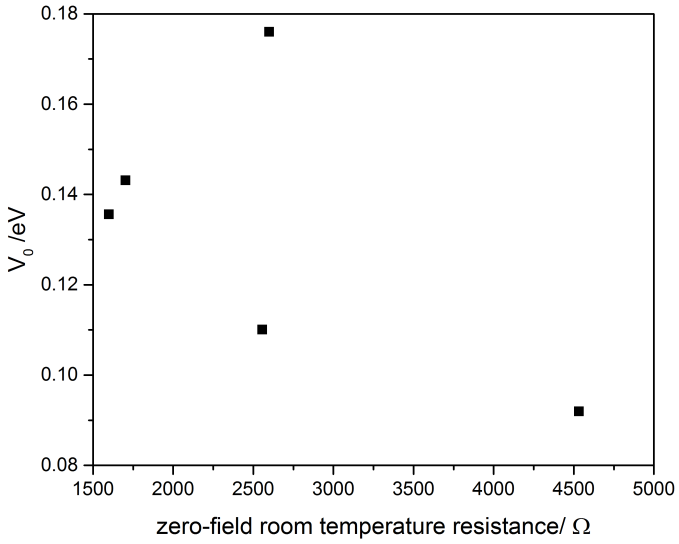

Figure 6.29: The calculated V_0 against the room-temperature zero-field resistance.

calculated V_0 is 0.26 eV. This is an assumption of an average Mg concentration as observed by charge carriers which is a slight over-simplification of what is observed in the confined electron space. As seen in figure 6.28 (a) there is a rather large spread of values given for the alloy scattering potential. So far there has been an assumption of a similar Mg content away from the interface region in all films. If the actual bulk Mg concentrations are taken it can be seen that they correlate well with the extracted V_0 as shown in figure 6.28 (b). There is one sample where this is not the case. This is one of the films where there is no ZnMgO constant film on top of the graded sample and there is a low Mg concentration. Here a larger than expected V_0 is observed. The surface bound states are increasing the scattering in the confined electron slab with there being the potential for incorporation of impurities at the surface. This correlation helps support the assignment of alloy scattering as the dominant scattering event.

Effects of Substrate Impurities

Although it can be seen that the maximum Mg concentration correlates well with V_0, the effects of contaminant ions can also be considered. It has already been noted that the room temperature resistance can give us a good indication of the purity and quality of the substrate and therefore a crude measure of these contaminant ions, such as Li. There is somewhat of a correlation between the zero-field room-temperature resistance and the alloy scattering potential as seen in figure 6.29. This could indicate that although the intended alloying with Mg is dominating the scattering, scattering from unintentional impurities such as Li could also be contributing to the scattering observed.

This is further supported when the classical and quantum scattering times are correlated to the room-temperature resistance. There is a strong dependence of the classical scattering time upon the room temperature resistance as shown in figure 6.30. This provides further indication that defects and impurities (possibly Li) and poor substrate quality play a significant role as alluded to in section 6.3. The Li impurities and defects act as spot defects to the conduction and therefore increase the scattering rate. This correlation further supports alloy scattering as the dominant scattering mechanism. The quantum scattering also demonstrates a similar trend, further supporting the assignment of one dominant scattering mechanism, and that mechanism being being alloy scattering.

6.7 Conclusion

In summary we have looked at the electronic model of a ZnMgO graded system and how changing the length of the graded region affects the confined nature of the electrons. A set of films was grown with graded ZnMgO. These were fabricated into devices and electronic measurements were made at low temperatures.

Increases in the low temperature mobility compared to ZnO bulk mobilities, indicates confined nature in the ZnMgO graded system. The presence of SdH oscillation further indicates the confined nature in these devices. The dependence of low temperature mobility on the Mg gradient at these interfaces was measured. We find that the quality of substrates is

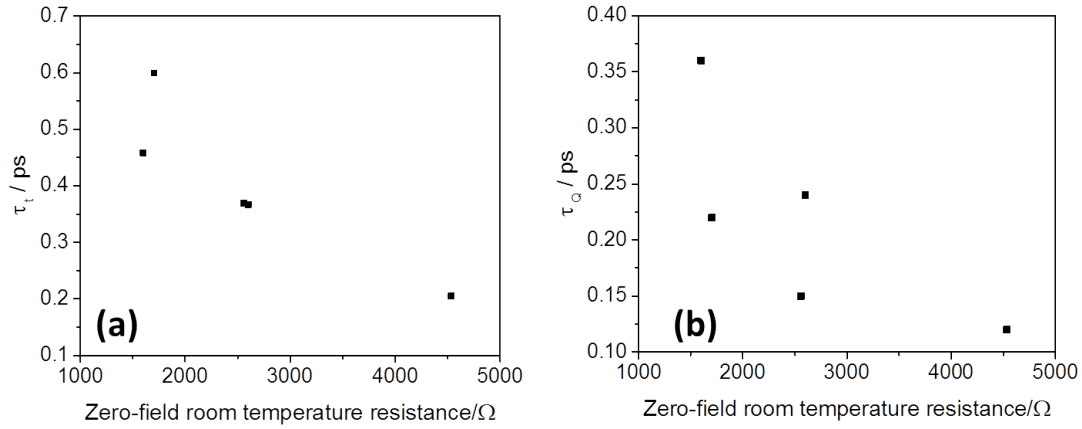

Figure 6.30: Zero-field room-temperature resistance plotted as a function of (a) τ_t and (b) τ_Q measured at 2 K.

of paramount importance when trying to achieve high mobilities as substrate impurities can limit the mobility. Although the shallow gradient interface creates a more relaxed film, the electrons are confined in a region with a larger than average Mg concentration. Since alloy scattering is the dominant scattering mechanism, the mobility is reduced. The films with a larger Mg gradient have more strain, yet the charge carriers see less Mg so the mobility observed is higher. We conclude that the degree of confinement over the graded system has a greater impact on the mobility than the strain.

The angular dependence of the magnetoresistance confirms the two dimensional nature of the confined electron space, with the confined electron space maintaining the 2D density of states. The Fourier transform of the megnetoresistance confirms that there is only one conduction path at low temperatures.

The classical scattering time shows a large dependence on the room-temperature resistance of the substrates, while quantum scattering has been shown to dominate the effective mass. The ratio of these two scattering times is on the same order, indicating one dominant scattering mechanism. This mechanism is alloy scattering due to the confined space being located in the ZnMgO. There is also an observed correlation between the alloy scattering and room temperature resistance indicating that the impurity is also contributing to this affect.

Correlations between room temperature resistance and the classical and quantum scattering times also indicating its affects. Therefore it is seen that both Mg-ion and impurity-ion scatting limit the mobility.

Chapter 7

Formation of Zn/ZnO/Zn Trilayers

With work still ongoing with 2DEG creation within ZnO/ZnMgO interface, work has also been done on Zn/ZnO/Zn MBE-grown Josephson junctions. With advantages of homoepitaxial junctions discussed in chapter 1.2, this new system could open up a new areas of low temperature superconducting applications. This chapter looks at the initial work done in the deposition of zinc thin films by MBE, its subsequent oxidation and device fabrication which will lead to initial testing of the junctions.

7.1 Zn Thin Film Growth

Similar to that of the ZnO/ZnMgO thin films, substrate selection and preparation is key to the growth of continuous metallic thin films. Within our MBE chamber there are limitations as to which substrates are appropriate, with it being necessary to limit contamination within the chamber. With this being the case initial trials with A- and C-plane sapphire , Si, soda-lime-glass and ZnO substrates with large zinc fluxes did not produce any zinc deposition, although there were small agglomerations of Zn at point defects on the surface. These were visible to the eye but only over small portions of the substrate. It is seen that the adhesion to these commonly used substrates is limited for zinc, as is the case for many metallic films with some common substrates [148]. With this being the case there was investigation into a wetting layer to provide a surface for the zinc to adhere to.

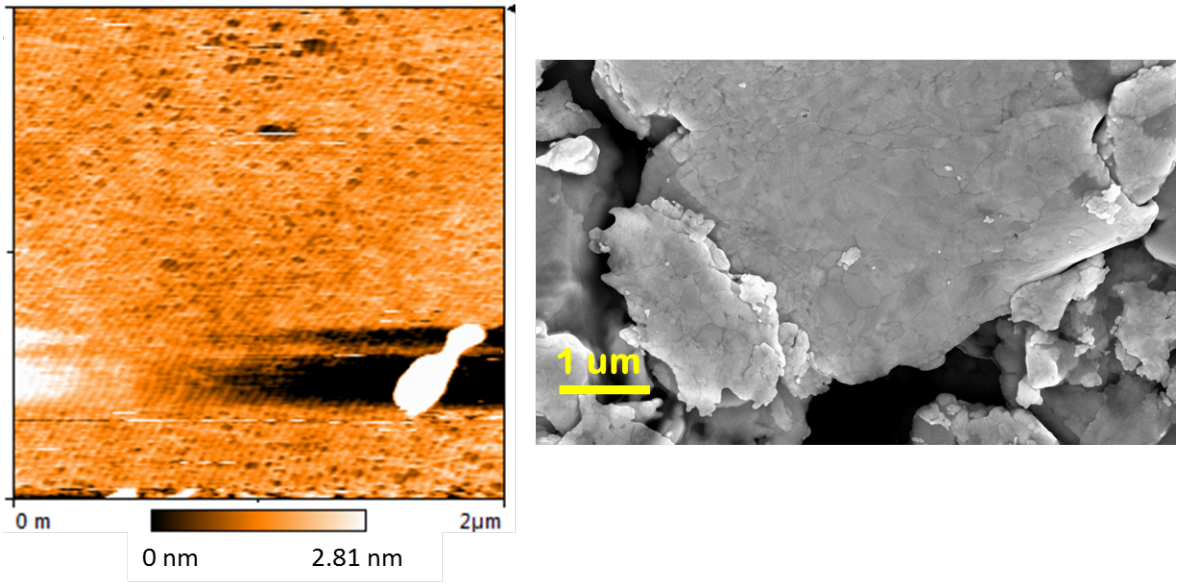

Figure 7.1: (a) AFM of 3 nm gold evaporated onto sapphire used as initial substrate, (b) SEM of zinc film grown on sapphire with 3 nm of gold evaporated pre-growth.

It was decided that a 3 nm layer of thermally evaporated Au could provide this wetting layer, as Au is already used in the chamber for nanowire growth. A 3 nm thickness was chosen as it is the same amount used for nanowire growth and would be enough to wet the substrate but also to limit contamination through the film. Figure 7.1 (a) shows the morphology of the gold as deposited on the c-plane sapphire. This provided a sufficient wetting layer for the zinc to adhere to. Thin films of zinc were grown as shown in figure 7.1 (b). The XPS (not shown) shows contamination of gold at the top surface of Zn of approximately 2 % for 100 nm grown of Zn. If we look at the as sputtered gold on sapphire we can see that there is some inherent roughness in the films. When the zinc grows on this surface the roughness is not seen to propagate through the film but is thought to provide points of nucleation for the large interconnected zinc flakes, seen in figure 7.1 (b), to grow from. These relatively large (3-6 μm), flat surfaces are difficult to make subsequent devices from due to the large surface roughness at the edges of the flake. These could provide routes for short circuits across subsequent junctions. As of yet, these are still the best quality results we have obtained for large area zinc deposition.

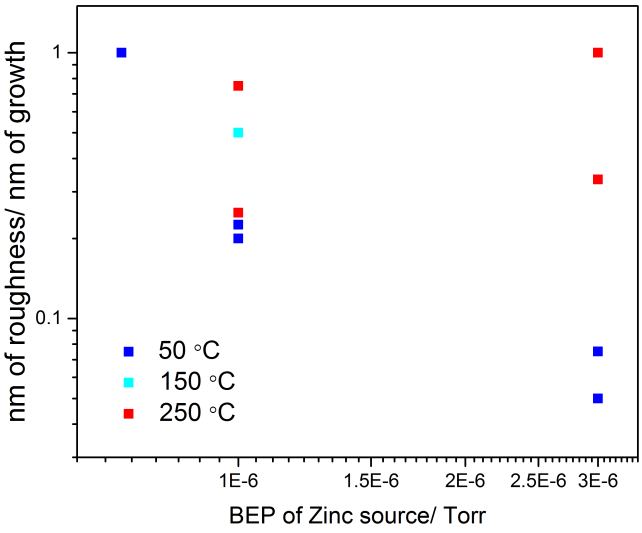

Figure 7.2: Dependence of relative film roughness (as defined in the text) on zinc beam equivalent pressure. Variations in colour denote the different stage temperatures during growth.

To create superconducting elemental zinc it is important to have a continuous zinc film so the deposition parameters play a vital role. The effects that varying zinc flux and substrate temperature have on the overall roughness of the film is shown in figure 7.2. The relative roughness is taken as the average change in the surface height over an area of (5 μm^2) divided by the overall film thickness These parameters are measured by profilometry. As the substrate temperature is increased there is an increase in the roughness compared to the film thickness grown. The changes in roughness are due to the re-evaporation and surface migration rates increasing as temperature increases, providing a route for the most thermodynamically stable film. These effects can be seen to be even more prevalent than in the ZnMgO thin films grown in earlier chapters. This is due to the metallic nature of the Zn-Zn bond making the adatoms more mobile than the ionic Zn-O bond that was seen in the ZnMgO. With Stranski-Krastanov mechanisms observed, it is seen that although there is thin film growth there is also island growth, and with more mobile surface atoms, these islands grow quicker than the thin films.

Temperatures were kept lower than observed for the ZnMgO/ZnO interfaces due to high temperatures causing Au particle formation [149] and also high rates of re-evaporation of the Zn, with the deposition rate at 250°C being half of that at 50°C. With lower deposition rates, there can be seen to be a sharp rise in the roughness as seen in figure 7.3, with the relative roughness being defined as the same as in figure 7.2. With longer depositions the preferential deposition sites become more pronounced, with roughness increasing as the film relaxes to its most stable form. With the need for subsequent ZnO growth to be continuous across the Zn, roughness will be a great disadvantage that could hinder its formation and allow for shorts through the ZnO.

With short growth times preferred, high zinc flux is preferred to keep the deposition times short while still growing significant thickness of zinc. The effect of varying the zinc flux is shown in figure 7.2. When considering only films grown at 50 °C (dark blue) there is a clear correlation, with higher zinc fluxes resulting in smoother films. With this being the case it is imperative that the growth temperature be kept low to stimulate good quality zinc growth with high zinc fluxes. The timings of growth are dictated by the required device geometry, although it is seen that shorter times minimize roughness.

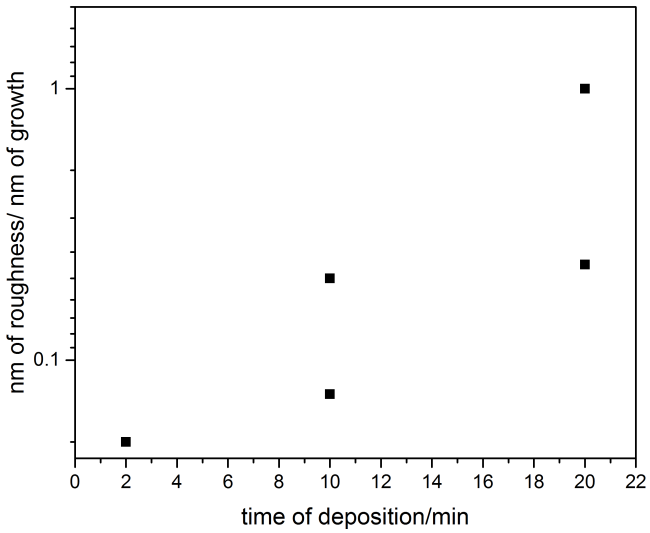

Figure 7.3: Duration of the MBE deposition affecting the ratio of thickness to roughness determined by profilometry. All samples grown at 50 °C with varying zinc BEPs on sapphire with 3 nm of gold seeding layer.

Overall we conclude that relaxation and thermodynamic stabilization is creating the roughness observed in the films. Although there is the possibility for limiting their effects by growing at lower temperatures, higher fluxes and short deposition times, these may mask possible issues with substrate preparation. More investigation into different possible wetting layers and substrates is really needed to reduce the need for such large relaxations which cause the roughness. Better nucleation coverage is required to promote thin film growth over island growth, which is currently not observed.

7.2 Electrical Characterization of Zn Thin Films

An un-patterned zinc film grown 1 μm thick with an area of approximately 5 mm x 5 mm on C-plane sapphire was Al wire-bonded in a four-terminal geometry and temperature lowered. Initial electrical characterization on the zinc showed that it was superconducting at 0.86 K

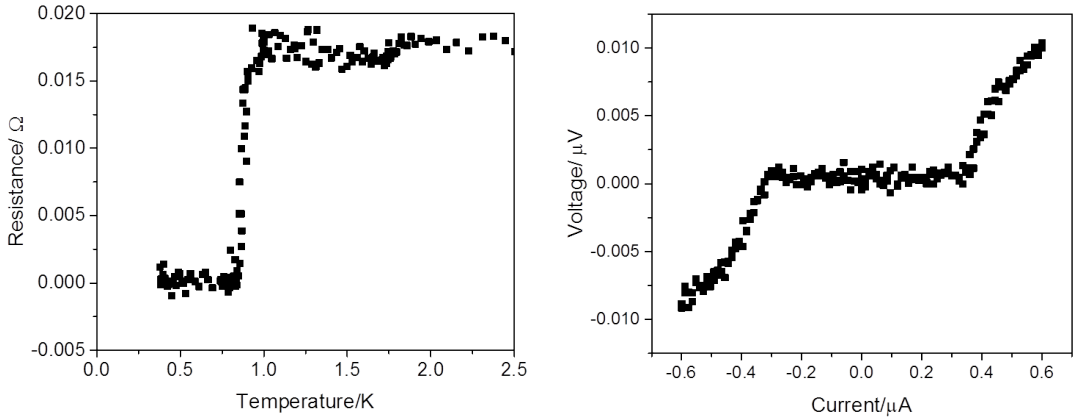

Figure 7.4: Four point resistance measurements of as grown zinc film directly wire bonded to as grown film, showing superconducting transition below 1 K (b) I-V sweep of same device at 0.4 K with superconducting region from -0.003 A to 0.003 A, with normal state observed outside this region.

which is in good agreement with the literature value of 0.85 K [150]. This is observed in the transition in figure 7.4 (a). This represents bulk Zn properties. The critical current feature is seen in figure 7.4 (b). This feature is seen to disappear when a specific magnetic field is applied normal to the film. The magnitude of the field needed to suppress the superconductivity varies as a function of temperature and is shown in figure 7.5. This is approximated by [151]:

$$B_c(T) = B_c(0)\left[1 - \left(\frac{T}{T_c}\right)^2\right], \tag{7.1}$$

which gives the zero temperature critical field needed as $B_c(0) = 4.7$ mT. This is in good agreement to that given in the literature of 5.0 mT [152].

With 1 μm deposited showing the same properties as bulk Zn, the effects of reducing the thickness were also considered. Although a variety of films were grown with varying thickness, there was no correlation between the thickness observed and the critical temperature or critical field. This due to the initial lack of device fabrication and the variations in the growth itself. The lack of device fabrication means that there are large variations in geometry and dimensionality from sample to sample. To vary the thickness the growth parameters need

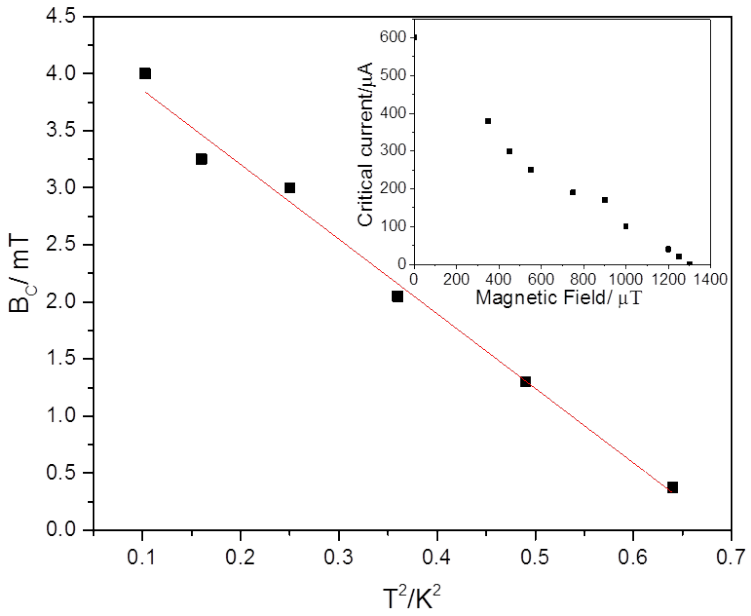

Figure 7.5: Observed critical field, B_C as a function of the square of the temperature. B_C obtained from x axis intercept of I_C against B as per the inset. I_C is obtained from measurements as in figure 7.4 (b), where the device changes from superconducting to normal state . Red line shows the fitting used to find $B_C(0)$.

to change. To get different thicknesses the temperatures of substrates, zinc fluxes or time of deposition needs to be changed. All of these have been seen to change the roughness of the films. The roughness of the film however does not directly affect the electrical properties of the film, though it can be indicative of boundaries and voids within the film which would directly affect the electrical properties as the thickness of the film is reduced. Therefore the morphology of the thin film itself plays a larger part in dictating the properties of the zinc than the thickness. Films with a thickness of 50 nm with comparable roughness but different deposition parameters have vastly different properties. A film deposited at 50 °C was seen to have T_c of 0.62 K where as a film at 250 °C was seen to start the transition at 0.6 K but the full transition was not observable within the He3 probe configuration whose minimum temperature is 0.3 K. With this being the case to really establish the effects of the dimensionality of the zinc film then there would have to be pre-growth device geometry fabrication in the gold film which would work if there was selectively in the growth (this will be discussed later) or post-growth device fabrication to standardize the measurement being taken.

7.3 Zn-ZnO-Zn Sandwich Layers

We have made initial investigations into the oxidization of zinc films to create the required geometry, with a thin ZnO layer having to be fabricated. Two methods of deposition are possible: opening the zinc and oxygen plasma at the same time and growing a zinc oxide film; or opening the oxygen plasma only and oxidizing the already formed zinc film. Initial trials were undertaken for the first option with the growth of zinc oxide, but since zinc is readily oxidizes, there is thought to still be some oxidation of the preliminary zinc layer as well, creating a continuous ZnO film.

We began by opening the oxygen and zinc for zinc oxide growth, followed by 10 min pump down and further zinc growth. The subsequent zinc films grown after ZnO deposition actually were zinc oxide containing zinc nano-particles, known as black zinc oxide. With the addition of a 1 hour pump down in between oxidation and zinc growth the zinc remained in

its un-oxidized form. XRD rocking curves of the films were used to determine the direction of growth of the embedded zinc oxide films. The XRD shows zinc (0002) peak [153] and definitively that zinc oxide has been formed with clear ZnO diffraction peaks seen in figure 7.6, although at such low intensities there are no thickness fringes to confirm thickness. There are two ZnO orientations observed; (0002) and (10-12), all in the growth direction. This indicates that there are many grain boundaries and roughness at the surface between the Zn and the ZnO. Although there is no preferential growth face from the two ZnO faces observed in the growth direction, (0002) is often seen for metallic surfaces such as gold and on c-plane sapphire, so the other planes observed may result from the increased roughness observed. With similar intensities both seem to have similar energetics during growth on the zinc top face.

The zinc grown on the zinc oxide does not seem to have the same sticking coefficient difficulties as experienced when using zinc oxide substrates. Initial oxidation set at 3 sccm of oxygen plasma for 10 minutes provided 300 nm of ZnO as seen in figure 7.7 (a). This is not ideal for observation of Josephson effect due to the zinc oxide being too thick. It was however used for initial device trials.

7.4 Device Fabrication

The initial device design is seen in schematic in figure 7.7 (b). Using the as grown film an array of EBL squares with side dimensions ranging from 1 μm to 10 nm were fabricated using a bi-layer PMMA/HSQ mask. HSQ was used for added resilience against the subsequent argon milling process. After masking these squares were milled. SiN was then sputtered with physical masking to leave an area of zinc accessible away from the milled squares. Nb tracks were then sputtered on the SiN only, with one milled square under each track. This included superconducting top and bottom contacts (Zn and Nb) and SiN to prevent shorting across the oxide layer. The SEM of a gallium FIB milled edge of a fabricated device is shown in figure 7.7 (a). It shows the device that was fabricated and highlights the problems we face on this top down approach. The different layers in the grown film can clearly be seen but voids

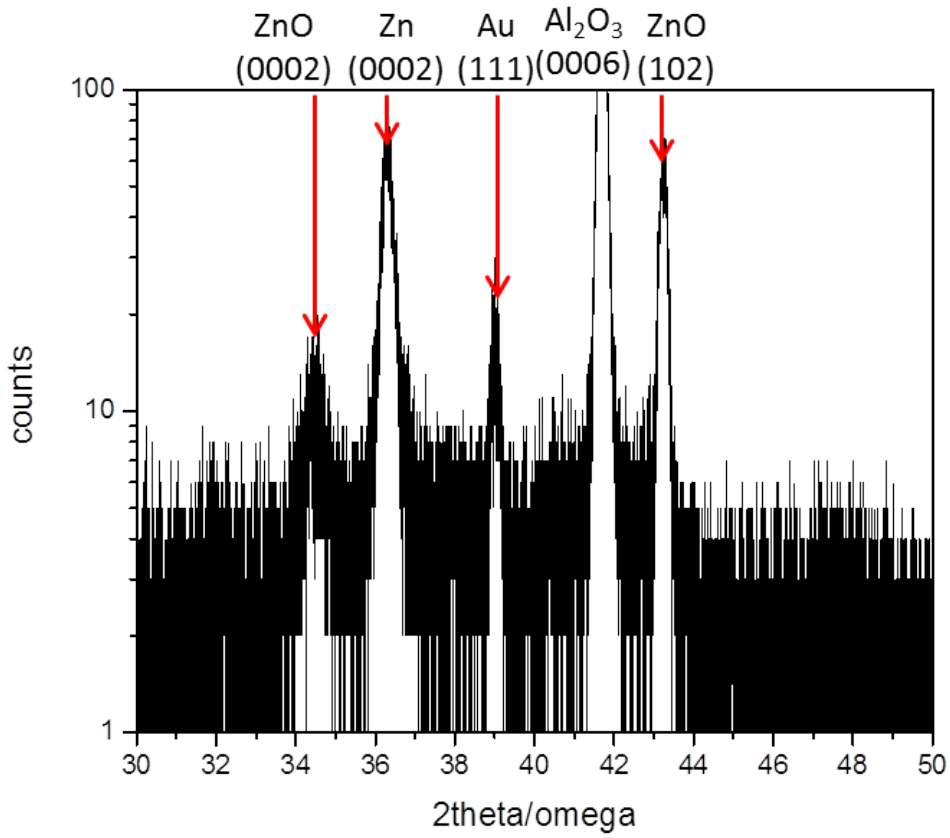

Figure 7.6: XRD rocking curve of the initial Zn/ZnO/Zn sandwich film, optimized for the substrate Al_2O_3 (0006) peak, with clear peaks from the Au wetting layer (111), Zn peak (0002) and two ZnO peaks (0002) and (10-12).

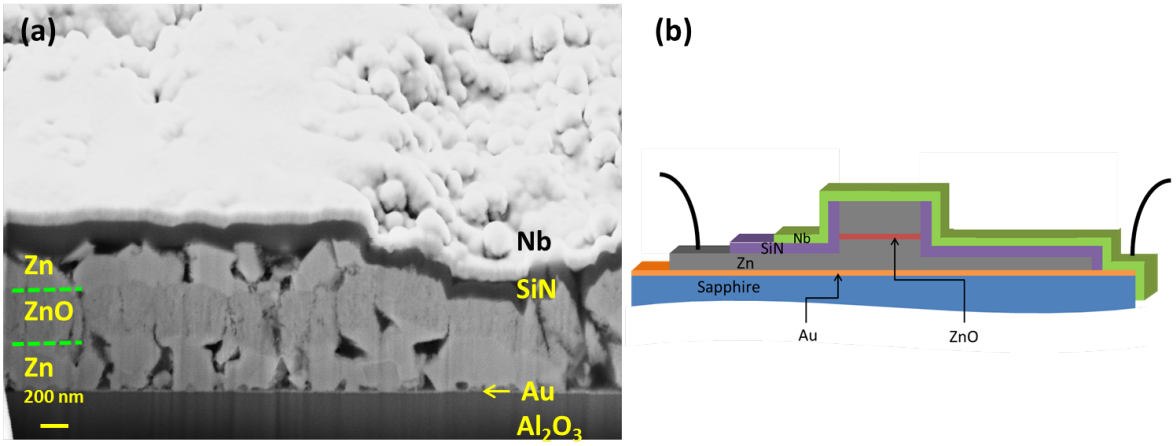

Figure 7.7: (a) SEM of processed device He-FIB milled through the layers of the device (b) expected cross-sectional device schematic (same angle as (a)).

in the film are also apparent. These initial voids in the growth lead to the porous nature of the Zn film and the large roughness that has been observed. This is not ideal for device fabrication. With this being said it can be seen that the ZnO is less porous and shows good coverage.

One of the most problematic features of this device fabrication is that the lift off was difficult since the HSQ/PMMA mask was removed during the argon mill, accompanied by minimal removal of the ZnO. This highlights a key difficulty that we have faced with Zn and ZnO milling compatibility with e-beam resists. With only a low voltage argon mill used all resist was removed within 15 minutes of milling. Reactive ion etching (RIE) had greater selectivity but was problematic due to the larger amounts of residual PMMA needed for the lift-off following SiN deposition. The difficulty is further accentuated by the difference in milling rates with Zn and ZnO, although having a ZnO layer under the SiN is not a problem for further device measurements.

With this being the case, the bottom up approach was considered. As previously mentioned attempts to grow Zn on c-plane sapphire were unsuccessful; demonstrating selectivity of growth on gold covered areas. Selectivity has also been shown for ZnO. Zinc oxide has also been grown for photonic devices and has shown selectivity as shown in figure 7.8. Therefore

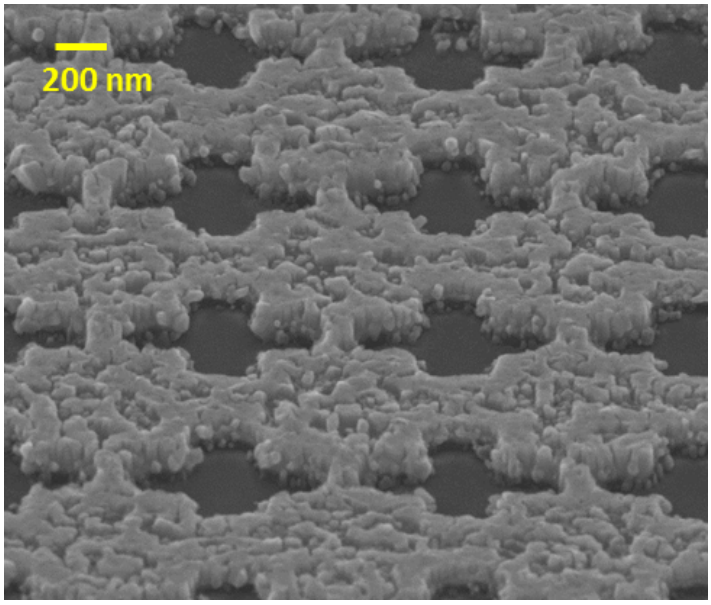

Figure 7.8: SEM of ZnO growth at 200 °C on Au covered sapphire. Crosses (dark contrast) contain no Au.

the pre-deposition of gold should be in small tracks, on the same scale as the flakes previously observed. This will also force the zinc to smaller dimensions and promote the geometry seen on the surface of the flake, removing the porous nature of the film as seen in figure 7.7 and therefore at the junction. The Nb top contact would be sputtered as before and then zinc can be milled between contacts using the low voltage mill which will remove the shorting zinc top layer without touching the zinc oxide, and the Nb contacts acting as a hard mask protecting the junction below. This is a possibility for further device fabrication, but was not carried out in this work.

7.5 Conclusion

We have demonstrated the possibility for superconducting zinc to be deposited by MBE. To date only bulk electronic properties of the zinc have been observed with deviation from bulk qualities not quantifiable due to large scale internal roughness that is dictated by the growth parameters. Oxidation layers have been grown without increasing the roughness of the film.

The orientation of the grown ZnO has been assigned to three primary orientations from the observed XRD peaks. These peaks are discernible from the background and are all of similar intensities but are low in intensity compared to the 3 nm of gold peak, indicating that there is a limited crystallinity within these layers grown.

Subsequent device fabrication has highlighted problems with the initial zinc deposition and optimization of wetting layer as the porosity of the zinc is observed. There have also been difficulties when using an EBL mask, needed for the small feature size needed for some Josephson junctions, with milling, prompting the need for a bottom up approach. The selectivity of the zinc and zinc oxide growth toward the gold compared to the sapphire has been observed and proposed as a possible method for creating a bottom up approach for the device fabrication.

Chapter 8

Conclusions and Future Work

8.1 Conclusions

In this work I have studied thin films of MBE grown ZnMgO on ZnO substrates and MBE grown Zn/ZnO/Zn films on sapphire. These thin films have been studied using XRD, AFM, SEM, XPS and PL. Hall bar devices have been fabricated and have been electronically studied in the PPMS and in a Helium 3 dip probe.

The primary investigations were into the ZnMgO/ZnO confined electron space. Initial studies into substrate preparation have shown that the as-received ZnO substrates contain Li implantation and $Zn(OH)_2$ surface implantation due to the solutions used in the hydrothermal growth of the ZnO. Through the use of a pre-etchant, HCL:H_2O (7:2000) for 30 seconds, there has been a decrease in the roughness of the Zn-polar ZnO substrate surface. It has been proposed that this is due to the removal of the $Zn(OH)_2$. Li implantation has not been overcome within this study and remains an issue for consideration.

The ZnMgO film was then grown directly onto the ZnO substrate. A variety of ZnMgO films have been grown with varying growth parameters. It has been shown that an increase in growth temperature can increase the crystalline quality of ZnMgO films and decrease the observed Mg incorporation. It has also been shown that the Mg BEP affects the morphology of the film, by reducing the Mg flux, the incorporated Mg concentration is reduced. Surface migration of the Mg has however been observed limiting the thin film Mg incorporation at

low Mg concentrations. At high Mg flux, there is seen to be MgO segregation, which has been shown to be suppressed when higher zinc fluxes are used, allowing for a strained but high concentration ZnMgO to be formed.

ZnMgO films have also been grown with Mg concentration gradients through the control of the zinc BEP at the point of growth. It has been observed that with high zinc flux, the growth is in the kinetic regime where the film is not able to form a relaxed film and the Mg concentration is more abrupt. With lower zinc fluxes the film is more relaxed so there is a shallower gradient. These variations in gradient have lead to variations in the properties of the confined electron space. The confinement of the elections is proposed to be over the same region as the graded interface. The samples that showed confinement through SdH oscillations and had similar maximum Mg concentrations were then compared. This confined electron space has lead to mobilities as high as $3,100 cm^2V^{-1}s^{-1}$ at 2 K. Two values of gradient were seen in the as grown samples, those approximately 0.2 % nm^{-1} and those with 1 % nm^{-1}. Those with a larger gradient, are seen to be more strained but have smaller length of confinement and therefore higher values of mobility.

Angular dependence of the applied magnetic field confirms that the space is two-dimensional through observing a lack of SdH oscillations when the magnetic field and current are perpendicular. The Fermi surface has been explored through the variations in the SdH oscillation frequency as the field is rotated. The damping of the SdH oscillation amplitude observed by the rotation of the magnetic field was also examined, again showing that the degree of confinement strongly correlates with the mobility of the samples.

The mechanisms of scattering were observed through the effective mass, which showed a dependence on the Mg gradient of the thin film. The scattering mechanisms were further discussed with the main mechanisms of interest being that of classical (being dictated by thermal events) and quantum scattering. A positive correlation of the thermal scattering rate with the room temperature resistance of the substrate again shows the importance of the substrate preparation and selection. Quantum scattering correlates with the effective mass of the charge carrier which is rationalized with the scattering event being a single body event, but more importantly the ratio of the classical and quantum scattering times is deemed

to be around unity. This suggests a similar overall overriding mechanism for both thermal and quantum scattering. With size scattering and dislocation scattering not being applicable, the main mechanism is seen to be alloy scattering. The origin of the alloy scattering is seen to be from the Mg as expected but also from the impurities such as Li.

Moving away from the confined electron space as observed in ZnMgO/ZnO there have also been investigations into the deposition of Zn/ZnO/Zn trilayers. Initial growth of MBE grown Zn and subsequent electrical measurements have shown the bulk properties for films above 100 nm in thickness and demonstrate good agreement with the literature. Thinner Zn layers have been grown but have been seen to be dictated by the growth conditions varying the internal morphologies rather than by the film thickness itself. Oxidation of these films has been successful showing two predominant growth directions of the ZnO on the Zn. It has then been possible to grow Zn on top of these structures. Initial Zn/ZnO/Zn trilayers have yielded problematic devices due to limited selectivity of the EBL masking. New bottom-up device fabrication and selective of growth of the ZnO and Zn have been proposed to grow devices, although no Josephson effect has yet been observed.

8.2 Further Work

8.2.1 Optimization of ZnMgO

It has become clear through the investigations conducted that ZnO native substrates have far to go before they can truly be considered for ZnO/ZnMgO confined electron space applications, especially with the solid-state mobility of Li being high. ZnO buffer layers have so far not yielded any samples with as high mobilities as those already quoted in this work at low temperature. Therefore the successful implementation of buffer layers is one of the next steps that is needed for high electron mobility samples.

If we continue to obtain ZnO substrates from the current supplier, due to there being a limited range of supplies for ZnO substrates worldwide, establishing the zero field room temperature resistance before growth could provide a method of eliminating poor substrates. By creating an ohmic contact to the ZnO substrate before growth without destroying the

surface polishing and smooth finish of the ZnO this could be measured. The possibility of gold contact with subsequent gold etchant is currently still being investigated by the group. The etchant would provide a route of removing the gold and acting in a similar manner to the HCl etch that was observed in chapter 5.1. Although this would enable us to identify the problematic substrates sooner, it would not reduce its impact on the subsequent films.

It is therefore proposed that the following work is undertaken into the following to overcome this:

- Further optimization of pre-growth parameters; the HCl etch is currently the method of choice but there are a variety of etchants available that may be better suited, as well as other thermal processes which could be used to better prepare the surface.

- Optimization of ZnO buffer layers; so far we have only grown ZnO using the same parameter space as considered when growing ZnMgO. By having a buffer layer grown at multiple temperatures there is the possibility that Li incorporation into the uppermost surface could be reduced. The optimization of this layer would also lead to better morphologies of the ZnO with smaller roughness which would also be advantageous.

- Moving to other substrates; other substrates such as sapphire have had some success. Although we have had no SdH observed, the Hall mobility is as high as 200 $cm^2V^{-1}s^{-1}$. There are still problems with roughness at the interface due to lattice mismatch and control of the polarity of the interference, with c-plane sapphire giving rise to O-polar Zn. In the current literature it has been shown that this can be changed by the introduction of a MgO layer [154]. For this to be successful there would have to be optimization of the MgO and ZnO to reduce the roughness of the films

Overall the variations in substrate have made reproducible sample growth difficult. If this was overcome then the properties of the confined electron space could be explored further and devices with superconducting contacts or spin injection could be realized.

There is also the possibility to consider device fabrication further. Argon milling is known to be a harsh milling technique, and due to the importance of surface transport in confined electron spaces its harshness could be detrimental to the transport. The possibility of RIE

has been alluded to in the previous chapter, and its problems stated. With selectivity of less than 2:1 PPMA:ZnO this is not ideal but there are some possibilities when using thicker photoresist for larger features. The effects of lowering the dimensionality of the system by reducing the channel width to that of a nanowire is also a possibility. Although this would have to be a top down approach (for example by using focused ion beam to reduce dimensions on already contacted devices) it will give an insight into the way the 2DEGs behave within a nanowire with reduced disorder. Disorder is inherent in those nanowires grown by catalysis [93]. It is also common for nanowires that are grown by catalysis to be in the core shell geometry so this sheet formation may be less affected by surface states. Nanowires grown with c-axis ZnO perpendicular to the growth direction is still under investigation [155].

8.2.2 Zn/ZnO/Zn device optimization

The growth and properties of Zn/ZnO/Zn trilayers grown by MBE is in its infancy. It may be useful to take a step back and a more extensive look into the wetting layer used for the zinc deposition while reducing the contamination of the MBE chamber. With this process optimized it is hoped that there would be fewer voids and boundaries observed in the as-grown films. By doing this in conjunction with pre-designed tracks of the same dimensionality of the flakes, as previously seen there should be a well ordered zinc thin film allowing us to investigate the effect that the dimensionality of the zinc has on the superconducting properties of the Zn. The selectivity has been shown in bulk, but the exact morphology of the edges of such a geometry is also something that requires further investigation. Once this has been mapped out, as the subsequent oxidation and Zn top layer has already been proven, so device fabrication should be reasonably straightforward. Overall the deposition of the metallic zinc is in its infancy, but with the selectivity discussed, we may provide a novel way to use MBE for the growth of Josephson junctions.

Appendices

Appendix A

Publication from this Work

The following publication was published using data presented in chapter 5 and chapter 6. The reference for this publication is;

Electron confinement at diffuse ZnMgO/ZnO interfaces; Maddison L. Coke, Oscar W. Kennedy, James T. Sagar and Paul A. Warburton; APL MATERIALS **5**, 016102 (2017)

APL MATERIALS **5**, 016102 (2017)

Electron confinement at diffuse ZnMgO/ZnO interfaces

Maddison L. Coke,[1] Oscar W. Kennedy,[1] James T. Sagar,[1] and Paul A. Warburton[1,2]
[1]*London Centre for Nanotechnology, University College London, 17-19 Gordon Street, London WC1H 0AH, United Kingdom*
[2]*Department of Electronic and Electrical Engineering, University College London, Torrington Place, London WC1E 7JE, United Kingdom*

(Received 28 September 2016; accepted 21 December 2016; published online 10 January 2017)

Abrupt interfaces between ZnMgO and ZnO are strained due to lattice mismatch. This strain is relaxed if there is a gradual incorporation of Mg during growth, resulting in a diffuse interface. This strain relaxation is however accompanied by reduced confinement and enhanced Mg-ion scattering of the confined electrons at the interface. Here we experimentally study the electronic transport properties of the diffuse heteroepitaxial interface between single-crystal ZnO and ZnMgO films grown by molecular-beam epitaxy. The spatial extent of the interface region is controlled during growth by varying the zinc flux. We show that, as the spatial extent of the graded interface is reduced, the enhancement of electron mobility due to electron confinement more than compensates for any suppression of mobility due to increased strain. Furthermore, we determine the extent to which scattering of impurities in the ZnO substrate limits the electron mobility in diffuse ZnMgO–ZnO interfaces. [http://dx.doi.org/10.1063/1.4973669]

ZnO has attracted much interest recently owing to its favourable electronic properties. ZnO is a wide band gap (3.37 eV) semiconductor[1] with a polar unit cell.[2] In ZnMgO, both the band gap and polarization depend upon the Mg concentration, x. At the interface between ZnO and ZnMgO, a combination of band-gap and polarization mismatch confines electrons to a two-dimensional electron gas (2DEG) with low-temperature electron mobility exceeding 10^6 cm^2 V^{-1} s^{-1}.[3] Such high mobilities have been realized due to high-quality interfaces made possible by molecular beam epitaxy (MBE) growth techniques. Mg incorporation also causes the c-lattice parameter of ZnMgO to decrease with increasing x due to the smaller atomic radius of Mg.[4] This is accompanied by a small increase in the a-lattice parameter.[5] Therefore, at an abrupt ZnO/ZnMgO interface some strain is inevitable. The strain can be relaxed if the system is in equilibrium during growth. This occurs through a redistribution of the Mg atoms across the interface region during the growth process, resulting in a less abrupt interface. Neighbouring unit cells have a small difference in Mg concentration and thus the lattice mismatch is negligible. By contrast, at abrupt interfaces, neighbouring unit cells have different lattice parameters, resulting in a significantly strained interface.

In order to create a high mobility 2DEG, it is necessary to minimize the amount of scattering. Scattering may occur both due to crystal defects associated with lattice mismatch between film and substrate and due to randomly substituted Mg atoms. At a diffuse interface we expect less scattering at the interface due to the more gradual release of strain, but an increase in random alloy scattering by comparison with abrupt interfaces. These two scattering mechanisms vary in importance depending on the spatial extent of the Mg redistribution at the interface. In addition, the degree of electron confinement depends upon the abruptness of the interface.

Here, we present an experimental study of the competing effects of electron scattering and confinement at ZnO/ZnMgO interfaces as we vary the spatial extent of the interface region. The Mg concentration gradient is controlled by varying the zinc flux during MBE growth and measured by x-ray photoelectron spectroscopy (XPS) depth-profiling. The electron mobility at the interface is extracted from magnetoresistance measurements at low temperature.

We first calculate the band structure and electron concentration at a diffuse interface between two semi-infinite regions of ZnO and ZnMgO with growth direction [0001]. The region $z < 0$ is ZnO while the interface region $0 < z < \zeta$ is ZnMgO with the Mg content x being linearly graded from zero to x_0. The region $z > \zeta$ is uniformly ZnMgO with $x = x_0$. Hence, the diffuse interface extends from $z = 0$ to $z = \zeta$, the Mg concentration gradient in this region being $dx/dz = x_0/\zeta$, as shown in Figure 1(a). Band bending at the interface arises from two distinct sources—the spatial variation of both the bandgap and the polarization P. Specifically, the Maxwell-Gauss law states that the charge density ρ_{pol} arising from the polarization gradient is given by the divergence of P. In the absence of any polarization gradient, the carriers would be confined in the material with the lower bandgap as for a conventional GaAs–AlGaAs heterostructure. For a non-zero polarization gradient, however, it is possible for carriers to be confined in the interface region where the bandgap is not at its minimum value. This is schematically illustrated in Figure 1(a).

Furthermore, in Figures 1(b)–1(c), we present the results of self-consistent finite element simulations of ZnO/ZnMgO interfaces performed by solving the Poisson-Schrödinger equation. The equation is solved in one dimension with an element size of 1 Å.[1,6–10] The "bulk" Mg concentration at $z > \zeta$ is 40%. The carrier concentration in both the ZnMgO and ZnO far from the interface region is taken to be 10^{18} cm^{-3}.[11] This yields a sheet carrier concentration at the interface of 6.3×10^{12} cm^{-2}, this being independent of the width ζ of the interface region. At the abrupt interface ($dx/dz \rightarrow \infty$) a sharp, deep quantum well forms in the conduction band.[18] A 2DEG is formed at the surface of the ZnO. By contrast, for diffuse interfaces we see broader conduction band wells with the charge-confined region extending over the whole width of the interface region. This has previously been referred to as a three dimensional electron slab (3DES) and experimentally observed in ZnO/ZnMgO[12] and other polar materials such as AlGaN/GaN.[13] It results from the continuously spatially varying lattice parameter which gives rise to a continuously changing polarization. This leads to a built-in electric field across the interface. Free charges move into the ZnMgO layer in order to compensate for the built-in field, resulting in a lower carrier density than for the abrupt interface. This type of 3DES can only exist in crystal systems where polarization engineering is possible. For diffuse interfaces, a significant fraction of the carriers are located in the ZnMgO layer, unlike for abrupt interfaces. For $dx/dz = 1\%$ nm^{-1}, for example, 96% of the carriers are located in the interface region $0 < \zeta < z$.

ZnMgO films were grown directly onto Zn-polar ZnO polished substrates (SurfaceNet GmbH) in an MBE chamber at 750 °C for 1 h. Oxygen plasma was generated using a 300 W RF generator. The Zn beam equivalent pressure was measured by a retractable beam flux monitor. The elemental

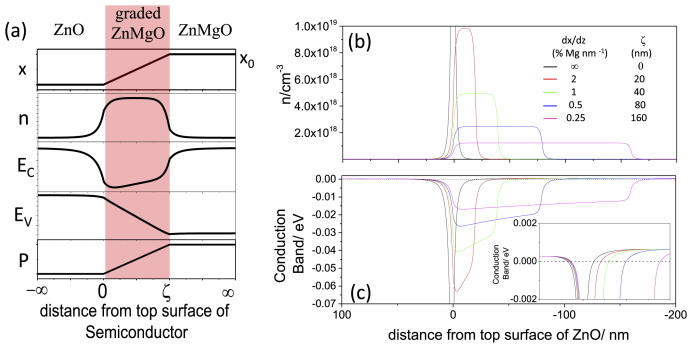

FIG. 1. (a) Schematic diagrams showing the fractional Mg concentration, x, carrier density, n, conduction band edge, E_C, valence band edge, E_V, and charge polarization, P, across a linearly graded interface of width ζ between ZnO and ZnMgO. Note that in reality the magnitude of the change in E_V exceeds that of E_C by one or two orders of magnitude so that the spatial variation of the bandgap essentially follows that of E_V. Self-consistent calculations of (b) the free electron density and (c) the conduction band offset, with the dotted line showing the Fermi energy, for selected values of the Mg concentration gradient, dx/dz, in the interface region. The "bulk" Mg concentration for $z > \zeta$ is $x_0 = 40\%$ in all cases. The inset in (c) shows the conduction band offset between ZnMgO and ZnO at a magnified scale.

composition was determined by XPS. A depth profile of the composition was obtained by sequential 3 keV argon-ion milling to a depth of 10 nm per iteration before performing *in situ* XPS measurements. X-ray diffraction (XRD) was used to characterize crystalline quality. Devices were fabricated by argon milling a mesa in the Hall bar geometry and sputtering Ti/Au (15 nm/50 nm) contacts. Resistivity and magnetoresistance measurements were carried out using a Quantum Design PPMS, in a perpendicular magnetic field.

In order to investigate the effect of varying the Mg gradient at the ZnO/ZnMgO interface, we must be able to control the Mg concentration gradient at the point of growth. The Mg gradient depends on the rate of Mg incorporation relative to the growth rate. This can be controlled by adjusting the zinc flux. With low Zn flux, re-evaporation and surface migration allow the system to reach equilibrium. The film becomes lattice latched[14] whereby the Mg content is determined by the excess energy the system has compared to that needed to grow a lattice mismatched unit cell. Conversely, at high Zn flux, due to the system not reaching equilibrium, a more abrupt Mg interface is grown.

In Figure 2(a) we show the spatial variation of the Mg content of five ZnMgO films grown at various values of Zn flux. We extract the Mg concentration gradient, dx/dz, by fitting to the approximately linear region of the depth profile close to the interface. The dependence of the Mg gradient upon the zinc flux for all samples is shown in Figure 2(b), confirming that more abrupt interfaces are obtained at higher zinc flux. Furthermore, at high zinc flux we can reduce the abruptness of the interface by increasing the temperature of the substrate (data not shown). This results from an increase in re-evaporation which reduces the growth rate, further confirming the above conjecture. The scatter in the data at low zinc flux is possibly due to variations in the substrate quality at the surface and mechanical polishing defects.

We now determine the crystallographic properties of the ZnMgO films using XRD. In order to analyse the interface strain we plot reciprocal space maps (RSMs) of two representative films, with Mg concentration gradients of 0.2% nm^{-1} (Figure 3(a)) and 1% nm^{-1} (Figure 3(b)). In both RSMs the high intensity central point is the $(01\bar{1}4)$ peak from the bulk ZnO substrate. Both RSMs show an additional peak which is caused by diffraction from the $(01\bar{1}4)$ ZnMgO planes. For the interface with the lower Mg gradient (Figure 3(a)), this peak is shifted with respect to the substrate peak in both Q_x and Q_z, showing that the ZnMgO lattice parameter has changed both in-plane and out of plane with respect to ZnO. For the more abrupt interface (Figure 3(b)), however, there is no shift in Q_x for the $(01\bar{1}4)$ ZnMgO peak, showing that the in-plane lattice parameter of the ZnMgO layer is the same as the underlying ZnO substrate. This film is therefore subject to in-plane strain. To maintain the ZnMgO unit cell volume, the shift in Q_z is larger for the more abrupt interface.

We now consider the electronic properties of the interfaces. We select five films, all of which have a maximum Mg concentration between 30% and 40%. The XPS depth profiles of these films are shown in Figure 2(a). The spatial extent of the interface region varies from 100 nm (corresponding to the whole grown film) to 40 nm. All five films show Shubnikov de Haas (SdH) oscillations at low temperatures in a perpendicular magnetic field. A typical magnetoresistance plot is shown in the inset

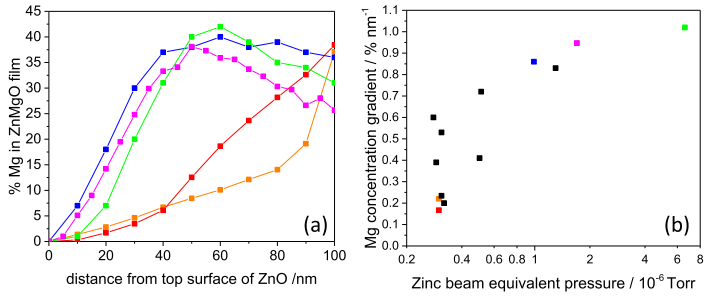

FIG. 2. (a) Mg concentration variation in five ZnMgO films as determined by XPS depth profiling. (b) Dependence of the interface Mg concentration gradient on the zinc beam-equivalent-pressure during MBE growth of the ZnMgO films. Coloured symbols in (b) correspond to the coloured plots in (a).

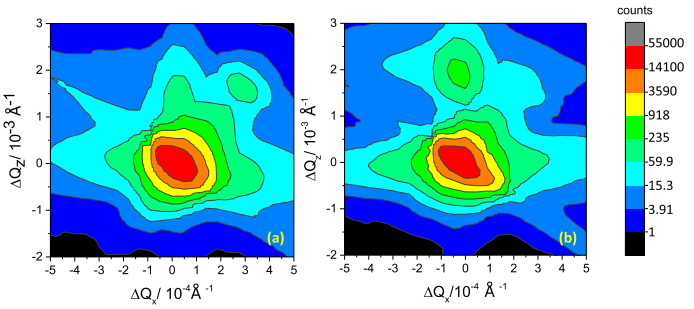

FIG. 3. X-ray diffraction reciprocal space maps referred to the $(01\bar{1}4)$ ZnO reflection in films with (a) an Mg concentration gradient of 0.2% nm^{-1} and (b) a higher Mg gradient of 1% nm^{-1}.

of Figure 4(a). At low field, prior to the onset of the SdH oscillations there is a region of negative magnetoresistance arising from the suppression of weak localization. The sheet carrier concentration extracted from the periodicity of the SdH plots is 3×10^{12} cm^{-2} with a sample-to-sample variation of ±25%. This value is consistent with those determined using the Poisson–Schrodinger model as shown in Figure 1(b). From the sheet carrier concentration the mobility can be extracted. This is shown as a function of the Mg interface concentration gradient in Figure 4(a). The mobility at 2 K is observed to be as high as 3100 cm^2 V^{-1} s^{-1}. This is two orders of magnitude higher than the low temperature mobility of ZnO,[15] confirming that substrate conduction plays no significant role. We also performed measurements of the Hall mobility which yield values within 10% of those in Figure 4(a), giving further confirmation that any parallel conduction paths are frozen out. Figure 4(a) shows a possible trend towards higher electron mobility for more abrupt interfaces, suggesting that, at least within the presented range of values of the Mg concentration gradient, the benefits of carrier confinement outweigh the additional scattering resulting from the strained lattice. This is the main conclusion of our experiments.

We note however that there is significant scatter in the data. Electron mobilities at ZnO/ZnMgO interfaces depend upon impurities in the substrates. The presence of residual lithium ions in the substrate can severely reduce the 3DES mobility.[16] Since the zero-field room-temperature electrical resistance of the substrate correlates with the residual lithium concentration,[17] we have plotted the dependence of the low temperature (i.e., confined electron dominated) mobility as a function of the room-temperature (i.e., substrate-conduction dominated) resistance as shown in Figure 4(b). The room-temperature resistance is measured through the same contacts used for the low temperature transport measurements. These are configured in a geometry which is not designed for and hence does not enable the extraction of the substrate resistivity. We observe that the data fall into two distinct

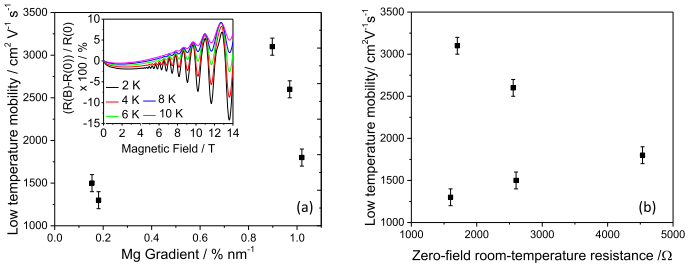

FIG. 4. (a) The electron mobility at T = 2 K (extracted from magnetoresistance measurements) as a function of the Mg concentration gradient dx/dz for films with bulk Mg content x_0 = 40%. The inset is a typical magnetoresistance measurement showing SdH oscillations at various indicated temperatures. This film has dx/dz = 1% nm^{-1}. (b) Dependence of mobility at 2 K on zero-field room temperature substrate resistance.

sets. Films with less abrupt interfaces ($dx/dz \sim 0.2\%$ nm^{-1}) have mobility less than 1600 cm^2 V^{-1} s^{-1} with no discernible dependence on the crystalline quality of the substrate. By contrast, films with more abrupt interfaces ($dx/dz \sim 1\%$ nm^{-1}) show a marked increase in low temperature mobility as the room temperature resistance decreases. From these data we conclude that there exists a threshold level of electron confinement (corresponding to an Mg concentration gradient lying between 0.2% and 1% nm^{-1}), below which the mobility is limited by scattering off the Mg ions and above which it is limited by scattering off defects in the ZnO substrate.

We have demonstrated control over abruptness of ZnO/ZnMgO interfaces through the control of the Zn flux during growth. Varying the Mg concentration gradient affects both the electrostatics and the crystallographic strain at the interface. Although a more diffuse interface yields a more relaxed film with fewer crystalline defects, the electrons are confined in a region with a larger average Mg concentration. The electron mobility is reduced due to the increase in electron-ion scattering. The films with a larger Mg gradient are more strained yet see less Mg resulting in higher values of mobility. We conclude that degree of electron confinement in the graded system has a greater impact on the mobility than crystal defects induced by strain.

This work was supported by UK EPSRC Grant Reference No. EP/H005544/1 and by U.S. AFOSR Grant Reference No. FA8655-12-1-2126.

[1] A. Janotti and C. G. Van de Walle, "Fundamentals of zinc oxide as a semiconductor," Rep. Prog. Phys. **72**(12), 126501 (2009).
[2] H. Morkoç and Ü. Özgür, *General Properties of ZnO, in Zinc Oxide* (Wiley-VCH Verlag GmbH & Co. KGaA., 2009), pp. 1–76.
[3] J. Falson *et al.*, "MgZnO/ZnO heterostructures with electron mobility exceeding 1×10^6 cm^2/Vs," Sci. Rep. **6**, 26598 (2016).
[4] T. A. Wassner *et al.*, "Optical properties and structural characteristics of ZnMgO grown by plasma assisted molecular beam epitaxy," J. Appl. Phys. **105**(2), 023505 (2009).
[5] A. Ohtomo *et al.*, "$Mg_xZn_{1-x}O$ as a II–VI widegap semiconductor alloy," Appl. Phys. Lett. **72**(19), 2466–2468 (1998).
[6] Y. Kozuka *et al.*, "Precise calibration of Mg concentration in $Mg_xZn_{1-x}O$ thin films grown on ZnO substrates," J. Appl. Phys. **112**(4), 043515 (2012).
[7] A. Malashevich and D. Vanderbilt, "First-principles study of polarization in $Zn_{1-x}Mg_xO$," Phys. Rev. B **75**(4), 045106 (2007).
[8] H. Tampo *et al.*, "Band profiles of ZnMgO/ZnO heterostructures confirmed by Kelvin probe force microscopy," Appl. Phys. Lett. **94**(24), 242107 (2009).
[9] G. L. Snider, I. H. Tan, and E. L. Hu, "Electron states in mesa-etched one-dimensional quantum well wires," J. Appl. Phys. **68**(6), 2849–2853 (1990).
[10] I. H. Tan *et al.*, "A self-consistent solution of Schrödinger–Poisson equations using a nonuniform mesh," J. Appl. Phys. **68**(8), 4071–4076 (1990).
[11] N. A. Jayah *et al.*, "High electron mobility and low carrier concentration of hydrothermally grown ZnO thin films on seeded a-plane sapphire at low temperature," Nanoscale Res. Lett. **10**(1), 7 (2015).
[12] J. Ye *et al.*, "Spin-polarized wide electron slabs in functionally graded polar oxide heterostructures," Sci. Rep. **2**, 533 (2012).
[13] D. Jena *et al.*, "Realization of wide electron slabs by polarization bulk doping in graded III–V nitride semiconductor alloys," Appl. Phys. Lett. **81**(23), 4395–4397 (2002).
[14] M.delP. Rodríguez-Torres *et al.*, "Investigation of the 'composition-pulling or lattice-latching' effect in LPE," J. Cryst. Growth **277**(1–4), 138–142 (2005).
[15] P. Wagner and R. Helbig, "Halleffekt und anisotropie der beweglichkeit der elektronen in ZnO," J. Phys. Chem. Solids **35**(3), 327–335 (1974).
[16] P. T. Neuvonen *et al.*, "Intrinsic point-defect balance in self-ion-implanted ZnO," Phys. Rev. Lett. **110**(1), 015501 (2013).
[17] E. D. Kolb and R. A. Laudise, "Hydrothermally grown ZnO crystals of low and intermediate resistivity," J. Am. Ceram. Soc. **49**(6), 302–305 (1966).
[18] In reality, due to the finite element size used, the curves labelled $dx/dz \to \infty$ correspond to a change in Mg concentration from zero to 40% over one element, i.e., $dx/dz = 400\%$ nm^{-1}.

Appendix B

Data for Modeling

In this appendix the values of the parameters used for modeling described in section 6.1 are given. Software obtained at the website given in [156] was used. This is derived from the principles set out in [122] [123]. The following parameters were used to simulate band bending at the ZnO/ZnMgO interface.

The code defines all the elements that are needed to simulate the band bending. The code consists of 2 files; the materials file- where the materials used and their parameters are defined; and the structure file, where the conditions for the system being investigated are defined.

If we first take the structure file. The system is defined in terms of slabs of ZnO and ZnMgO, with an associated Mg concentration. These concentrations can be set to vary linearly throughout the slab from two pre-defined concentrations. These slabs also indicate which material file to use for given slabs of the system. These slabs are then are sandwiched between commands to define the substrate and the surface condition. The surface condition is given so that the gradient at the condition band is zero; this is realistic based on Maxwells equations. Over these slabs, there is a mesh overlaid which defines the step size of the calculation, for our calculations this is 1 A. Over the band bending slab(s) is where the code will calculate the values whilst keeping it consistent with the Schrödinger equation. Finally the system is noted as fully ionized and the temperature of the sample is also given, in our calculations it is given as 2 K.

The materials files are separated into two sets of parameters, those that are constant in both ZnO and ZnMgO and those that change with relation to how much Mg is incorporated. The table below gives the values of the parameters that do not change with added Mg, so only one value is given.

parameter	value	reference or justification
donor concentration	5.2x $10^{18} cm^3$	[157]
acceptor concentration	0	p type conduction dominant in regime we are considering
deep donor concentration	0	ideal ZnO with no O_{vac}
deep acceptor concentration	0	ideal ZnO with no Li incorporation

The second set of parameters are given in the following table. Given that parameter, y, can change linearly with respect to Mg concentration, x, in the form y=ax + c, where c represents the base value where x=0 i.e. ZnO and a is a constant that controls the effect of Mg on a given parameter and can range from 0 to 1.

parameter	c	a	reference or justification
energy gap	3.37 eV	2.0 eV	[56] [12]
band offset	-	0.67 eV	The heterojunction between ZnO and ZnMgO is assumed to have type-I alignment with the difference in the band-gap evenly divided between the conduction-band offset and the valence-band offset [158], XPS measurements used to determine the variation with Mg incorporation

dielectric constant	7.78	-	[159] [160]
donor ionization energy	0.058 eV	-	[161]
acceptor ionization energy	0.23 eV	-	[162]
deep donor ionization energy	0.4 eV	-	O_{vac} in ZnO. Taken from experimental data from Chapter 5.1, no Mg contribution
deep acceptor ionization energy	-2.6 eV	-	Li present in ZnO. Taken from experimental data from Chapter 5.1, none Mg dependent
effective mass	0.25 m_e	0.27 m_e	average taken from literature [130] [131], Mg dependence from [163]
conduction band valence degeneracy	1	-	[164]
heavy hole effective mass	0.1 m_e	-	[165]
light hole effective mass	0.1 m_e	-	[165]
electron mobility	69 $cm^2V^{-1}s^{-1}$	-290 $cm^2V^{-1}s^{-1}$	[166]
hole mobility	0 $cm^2V^{-1}s^{-1}$	-	p type conduction dominant in regime we are considering

electron lifetime	1x10^{12}s	-	of the order of scattering times observed in Chapter 6.5
hole lifetime	1E-09 s	-	p type conduction dominant in regime we are considering
polarization	3.22x 10^{-6} Cm^2	7.88x 10^{-7} Cm^2	[167] [62]
absorption coefficient	5.0 cm^{-1}	-0.625 cm^{-1}	taken at 3.35 eV [168] [169]

Appendix C

Derivations

Derivation for the following equations

From Section 6.4 Confirmation of Dimensionality

Using the equation

$$B_F = B_{F-xy}\left[(cos\theta)^2 + (sin\theta\frac{S_{F-xy}}{S_{F-iz}})^2\right]^{-1/2} \tag{C.1}$$

First considering the fraction $\frac{S_{F-xy}}{S_{F-iz}}$, and substituting in equations 6.8 and 6.9, this fraction cancels to

$$\frac{\sqrt{m_x m_y}}{\sqrt{m_z(\frac{cos\theta^2+sin\theta^2}{m_x})}} \tag{C.2}$$

If we assume a two dimensional case then m_z tends to infinity due to there being no movement of charge carriers in the z direction. If this is the case then $\frac{S_{F-xy}}{S_{F-iz}}$ tends to zero. Adding this back to the equation C.1, we then find that $B_F = B_{F-xy}\cos\theta$

From Section 6.5 Classical and Quantum Scattering Rates

For equation 6.11

$$\Delta R_{xx}^{osc} \propto A = \frac{A^T}{sinhA^T} 4e^{-\pi/(\omega_c\tau_{tot})} \tag{C.3}$$

$$A/T = \frac{2\pi^2 k/\hbar\omega_c}{e^{A^T}/2} 4e^{-\pi/(\omega_c\tau_{tot})} \tag{C.4}$$

$$ln(A/T) = ln(2\pi^2 k/\hbar\omega_c) - \pi\omega_c\tau_{tot} - A^T \tag{C.5}$$

If all terms that are non-temperature dependent are grouped to give C_2 and A^T is defined as $A^T = 2\pi^2 kT/\hbar\omega_c$ with $\omega_c = eB_{tot}/m*$, then the overall equation is

$$ln\left(\frac{A}{T}\right) = C_2 - \frac{2\pi^2 k_B T m^*}{e\hbar B} \tag{C.6}$$

Bibliography

[1] H.L. Störmer, R. Dingle, A.C. Gossard, W. Wiegmann, and M.D. Sturge. Two-dimensional electron gas at a semiconductor-semiconductor interface. *Solid State Communications*, **29**(10):705 – 709, 1979.

[2] Tomoya Kaneko, Kazumi Shiikuma, and Kazuaki Kunihiro. GaN HEMT high efficiency power amplifiers for 4G/5G mobile communication base stations. In *2014 Asia-Pacific Microwave Conference*, pages 994–997. IEEE, 2014.

[3] K. v. Klitzing, G. Dorda, and M. Pepper. New method for high-accuracy determination of the fine-structure constant based on quantized Hall resistance. *Phys. Rev. Lett.*, **45**:494–497, Aug 1980.

[4] D. C. Tsui, H. L. Stormer, and A. C. Gossard. Two-dimensional magnetotransport in the extreme quantum limit. *Phys. Rev. Lett.*, **48**:1559–1562, May 1982.

[5] A. Kumar, G. A. Csáthy, M. J. Manfra, L. N. Pfeiffer, and K. W. West. Nonconventional odd-denominator fractional quantum Hall states in the second Landau level. *Phys. Rev. Lett.*, **105**:246808, Dec 2010.

[6] Joseph Falson, Yusuke Kozuka, Masaki Uchida, Jurgen H Smet, Taka-Hisa Arima, Atsushi Tsukazaki, and Masashi Kawasaki. MgZnO/ZnO heterostructures with electron mobility exceeding $1\times10^6\mathrm{cm}^2/\mathrm{Vs}$. *Scientific reports*, **6**:26598, 2016.

[7] Y Kozuka, A Tsukazaki, D Maryenko, J Falson, S Akasaka, K Nakahara, S Nakamura, S Awaji, K Ueno, and M Kawasaki. Insulating phase of a two-dimensional electron gas

in Mg_x Zn_{1-x} O/ ZnO heterostructures below ν= 1/3. *Physical Review B*, **84**(3):033304, 2011.

[8] Feng Bi, Daniela F. Bogorin, Cheng Cen, Chung Wung Bark, Jae-Wan Park, Chang-Beom Eom, and Jeremy Levy. Water-cycle mechanism for writing and erasing nanostructures at the $LaAlO_3/SrTiO_3$ interface. *Applied Physics Letters*, **97**:173110, 2010.

[9] J. Y. Fu and M. W. Wu. Spin-orbit coupling in bulk ZnO and GaN. *Journal of Applied Physics*, **104**(9):093712, 2008.

[10] Alexander Shnirman, Yuriy Makhlin, and Gerd Schön. Noise and decoherence in quantum two-level systems. *Physica Scripta*, **102**:147, 2002.

[11] D.G. Thomas. The exciton spectrum of zinc oxide. *Journal of Physics and Chemistry of Solids*, **15**(1):86 – 96, 1960.

[12] Anderson Janotti and Chris G Van de Walle. Fundamentals of zinc oxide as a semiconductor. *Reports on Progress in Physics*, 72(12):126501, 2009.

[13] Sunayna B Bashar, Mohammad Suja, Muhammad Morshed, Fan Gao, and Jianlin Liu. An Sb-doped p-type ZnO nanowire based random laser diode. *Nanotechnology*, **27**(6):065204, 2016.

[14] Xiaolong Du, Zengxia Mei, Zhanglong Liu, Yang Guo, Tianchong Zhang, Yaonan Hou, Ze Zhang, Qikun Xue, and Andrej Yu Kuznetsov. Controlled growth of high-quality ZnO-based films and fabrication of visible-blind and solar-blind ultra-violet detectors. *Advanced Materials*, **21**(45):4625–4630, 2009.

[15] Ameer Azam, Faheem Ahmed, Sami S Habib, Zishan H Khan, and Numan A Salah. Fabrication of co-doped ZnO nanorods for spintronic devices. *Metals and Materials International*, **19**(4):845–850, 2013.

[16] Satishchandra B Ogale. *Thin films and heterostructures for oxide electronics*. Springer Science & Business Media, 2006.

[17] T. Makino, Y. Segawa, M. Kawasaki, A. Ohtomo, R. Shiroki, K. Tamura, T. Yasuda, and H. Koinuma. Band gap engineering based on $Mg_xZn_{1-x}O$ and $Cd_yZn_{1-y}O$ ternary alloy films. *Applied Physics Letters*, **78**(9):1237–1239, 2001.

[18] Alexander Frank Wells. *Structural inorganic chemistry*. Oxford University Press, 1984.

[19] David C Look. Recent advances in ZnO materials and devices. *Materials Science and Engineering: B*, **80**(1):383–387, 2001.

[20] Y.W. Heo, K. Ip, S.J. Pearton, D.P. Norton, and J.D. Budai. Growth of ZnO thin films on c-plane Al_2O_3 by molecular beam epitaxy using ozone as an oxygen source. *Applied Surface Science*, **252**(20):7442 – 7448, 2006.

[21] WL Dang, YQ Fu, JK Luo, AJ Flewitt, and WI Milne. Deposition and characterization of sputtered ZnO films. *Superlattices and Microstructures*, **42**(1):89–93, 2007.

[22] An-Jen Cheng, Yonhua Tzeng, Yi Zhou, Minseo Park, Tsung-hsueh Wu, Curtis Shannon, Dake Wang, and Wonwoo Lee. Thermal chemical vapor deposition growth of zinc oxide nanostructures for dye-sensitized solar cell fabrication. *Applied Physics Letters*, **92**(9), 2008.

[23] M.G. Tsoutsouva, C.N. Panagopoulos, D. Papadimitriou, I. Fasaki, and M. Kompitsas. ZnO thin films prepared by pulsed laser deposition. *Materials Science and Engineering: B*, **176**(6):480 – 483, 2011.

[24] Jürgen Hüpkes, Jorj I. Owen, Sascha E. Pust, and Eerke Bunte. Chemical etching of zinc oxide for thin-film silicon solar cells. *ChemPhysChem*, **13**(1):66–73, 2012.

[25] Kevin Robbie, Gisia Beydaghyan, Tim Brown, Cory Dean, Jonathan Adams, and Cristina Buzea. Ultrahigh vacuum glancing angle deposition system for thin films with controlled three-dimensional nanoscale structure. *Review of Scientific Instruments*, **75**(4):1089–1097, 2004.

[26] X Z Shang, W C Wang, S D Wu, Z G Xing, L W Guo, W X Wang, Q Huang, and J M Zhou. Effects of indium doping on the properties of AlAs/GaAs quantum wells

and inverted AlGaAs/GaAs two-dimensional electron gas. *Semiconductor Science and Technology*, **19**(3):519, 2004.

[27] S. Bollaert, Y. Cordier, M. Zaknoune, H. Happy, V. Hoel, S. Lepilliet, D. Thron, and A. Cappy. The indium content in metamorphic $In_xAl_{1x}As$ / $In_xGa_{1x}As$ HEMTs on GaAs substrate: a new structure parameter. *Solid-State Electronics*, **44**(6):1021 – 1027, 2000.

[28] R. J. Nicholas, J. C. Portal, C. Houlbert, P. Perrier, and T. P. Pearsall. An experimental determination of the effective masses for $Ga_xIn_{1x}As_yp_{1y}$ alloys grown on InP. *Applied Physics Letters*, **34**(8):492–494, 1979.

[29] K. Hess. Real space transfer: Generalized approach to transport in confined geometries. *Solid-State Electronics*, **31**(3):319 – 324, 1988.

[30] H. Brech. *Optimization of GaAs Based High Electron Mobility Transistors by Numerical Simulations*. 1998.

[31] V. Umansky, R. de Picciotto, and M. Heiblum. Extremely high-mobility two dimensional electron gas: Evaluation of scattering mechanisms. *Applied Physics Letters*, **71**(5):683–685, 1997.

[32] Loren Pfeiffer and K.W West. The role of MBE in recent quantum Hall effect physics discoveries. *Physica E: Low-dimensional Systems and Nanostructures*, **20**(12):57 – 64, 2003.

[33] V. Umansky, M. Heiblum, Y. Levinson, J. Smet, J. Nübler, and M. Dolev. MBE growth of ultra-low disorder 2DEG with mobility exceeding 35×10^6 cm^2/v s. *Journal of Crystal Growth*, **311**(7):1658 – 1661, 2009.

[34] Michael J Manfra. Molecular beam epitaxy of ultra-high quality AlGaAs/GaAs heterostructures: Enabling physics in low-dimensional electronic systems. *arXiv preprint arXiv:1309.2717*, 2013.

[35] A Ohtomo and HY Hwang. A high-mobility electron gas at the $LaAlO_3/SrTiO_3$ heterointerface. *Nature*, **427**(6973):423–426, 2004.

[36] Wan-Jian Yin, Su-Huai Wei, Mowafak M. Al-Jassim, and Yanfa Yan. Origin of the diverse behavior of oxygen vacancies in ABO_3 perovskites: A symmetry based analysis. *Phys. Rev. B*, **85**:201201, May 2012.

[37] H.Y. Hwang, A. Ohtomo, N. Nakagawa, D.A. Muller, and J.L. Grazul. High-mobility electrons in $SrTiO_3$ heterostructures. *Physica E: Low-dimensional Systems and Nanostructures*, **22**(13):712 – 716, 2004.

[38] Nobuo Tsuda, Keiichiro Nasu, Atsushi Fujimori, and Kiiti Siratori. *Electronic conduction in oxides*, volume **94**. Springer Science & Business Media, 2013.

[39] I. Pallecchi, M. Codda, E. Galleani d'Agliano, D. Marré, A. D. Caviglia, N. Reyren, S. Gariglio, and J.-M. Triscone. Seebeck effect in the conducting interface. *Phys. Rev. B*, **81**:085414, Feb 2010.

[40] N. Reyren, S. Thiel, A. D. Caviglia, L. F Kourkoutis, G. Hammerl, C. Richter, C. W. Schneider, T. Kopp, A.-S. Retschi, D. Jaccard, M. Gabay, D. A. Muller, J.-M. Triscone, and J. Mannhart. Superconducting interfaces between insulating oxides. *Science*, **317**(5842):1196–1199, 2007.

[41] C. W. Bark, D. A. Felker, Y. Wang, Y. Zhang, H. W. Jang, C. M. Folkman, J. W. Park, S. H. Baek, H. Zhou, D. D. Fong, X. Q. Pan, E. Y. Tsymbal, M. S. Rzchowski, and C. B. Eom. Tailoring a two-dimensional electron gas at the $LaAlO_3/SrTiO_3$ (001) interface by epitaxial strain. *Proceedings of the National Academy of Sciences*, **108**(12):4720–4724, 2011.

[42] Y Matsubara, KS Takahashi, MS Bahramy, Y Kozuka, D Maryenko, J Falson, A Tsukazaki, Y Tokura, and M Kawasaki. Observation of the quantum Hall effect in δ-doped $SrTiO_3$. *Nature communications*, **7**:11631, 2016.

[43] Cheng Cen, Stefan Thiel, Jochen Mannhart, and Jeremy Levy. Oxide nanoelectronics on demand. *Science*, **323**(5917):1026–1030, 2009.

[44] U. Schwingenschlgl and C. Schuster. Surface effects on oxide heterostructures. *EPL (Europhysics Letters)*, **81**(1):17007, 2008.

[45] S. Thiel, G. Hammerl, A. Schmehl, C. W. Schneider, and J. Mannhart. Tunable quasi-two-dimensional electron gases in oxide heterostructures. *Science*, **313**(5795):1942–1945, 2006.

[46] A. Janotti, L. Bjaalie, L. Gordon, and C. G. Van de Walle. Controlling the density of the two-dimensional electron gas at the $SrTiO_3/LaAlO_3$ interface. *Phys. Rev. B*, **86**:241108, 2012.

[47] Wolter Siemons, Gertjan Koster, Hideki Yamamoto, Walter A. Harrison, Gerald Lucovsky, Theodore H. Geballe, Dave H. A. Blank, and Malcolm R. Beasley. Origin of charge density at $LaAlO_3$ on $SrTiO_3$ heterointerfaces: Possibility of intrinsic doping. *Phys. Rev. Lett.*, **98**:196802, 2007.

[48] H. Tampo, K. Matsubara, A. Yamada, H. Shibata, P. Fons, M. Yamagata, H. Kanie, and S. Niki. High electron mobility Zn polar ZnMgO/ZnO heterostructures grown by molecular beam epitaxy. *Journal of Crystal Growth*, **301302**(0):358 – 361, 2007.

[49] M.J. Vellekoop, C.C.O. Visser, P.M. Sarro, and A. Venema. Compatibility of zinc oxide with silicon processing. *Sensors and Actuators A: Physical*, **23**(13):1027 – 1030, 1990.

[50] ET Yu, XZ Dang, PM Asbeck, SS Lau, and GJ Sullivan. Spontaneous and piezoelectric polarization effects in III-V nitride heterostructures. *Journal of Vacuum Science & Technology B*, **17**(4):1742–1749, 1999.

[51] Y. Kasahara, Y. Oshima, J. Falson, Y. Kozuka, A. Tsukazaki, M. Kawasaki, and Y. Iwasa. Correlation-enhanced effective mass of two-dimensional electrons in $Mg_xZn_{1-x}O/ZnO$ heterostructures. *Phys. Rev. Lett.*, **109**:246401, 2012.

[52] Chennupati Jagadish and Stephen J Pearton. *Zinc oxide bulk, thin films and nanostructures: processing, properties, and applications*. Elsevier, 2011.

[53] A Tsukazaki, S Akasaka, K Nakahara, Y Ohno, H Ohno, D Maryenko, A Ohtomo, and M Kawasaki. Observation of the fractional quantum hall effect in an oxide. *Nature materials*, **9**(11):889–893, 2010.

[54] D. F. Kärcher, A. V. Shchepetilnikov, Yu. A. Nefyodov, J. Falson, I. A. Dmitriev, Y. Kozuka, D. Maryenko, A. Tsukazaki, S. I. Dorozhkin, I. V. Kukushkin, M. Kawasaki, and J. H. Smet. Observation of microwave induced resistance and photovoltage oscillations in MgZnO/ZnO heterostructures. *Phys. Rev. B*, **93**:041410, 2016.

[55] Joseph Falson, Denis Maryenko, Yusuke Kozuka, Atsushi Tsukazaki, and Masashi Kawasaki. Magnesium doping controlled density and mobility of two-dimensional electron gas in Mg_x Zn_{1-x} O/ZnO heterostructures. *Applied Physics Express*, **4**(9):091101, 2011.

[56] Y. Kozuka, J. Falson, Y. Segawa, T. Makino, A. Tsukazaki, and M. Kawasaki. Precise calibration of Mg concentration in $Mg_xZn_{1x}O$ thin films grown on ZnO substrates. *Journal of Applied Physics*, **112**(4):043515, 2012.

[57] Denis Maryenko, Joseph Falson, Yusuke Kozuka, Atsushi Tsukazaki, Masaru Onoda, Hideo Aoki, and Masashi Kawasaki. Temperature-dependent magnetotransport around $\nu = 1/2$ in ZnO heterostructures. *Physical review letters*, **108**(18):186803, 2012.

[58] H. Tampo, H. Shibata, K. Matsubara, A. Yamada, P. Fons, S. Niki, M. Yamagata, and H. Kanie. Two-dimensional electron gas in Zn polar ZnMgOZnO heterostructures grown by radical source molecular beam epitaxy. *Applied Physics Letters*, **89**(13):132113, 2006.

[59] J. D. Ye, S. Pannirselvam, S. T. Lim, J. F. Bi, X. W. Sun, G. Q. Lo, and K. L. Teo. Two-dimensional electron gas in Zn-polar ZnMgO/ZnO heterostructure grown by metal-organic vapor phase epitaxy. *Applied Physics Letters*, **97**(11):111908, 2010.

[60] Kazuto Koike, Ippei Nakashima, Kazuyuki Hashimoto, Shigehiko Sasa, Masataka Inoue, and Mitsuaki Yano. Characteristics of a $Zn_{0.7}Mg_{0.3}O$ZnO heterostructure field-effect transistor grown on sapphire substrate by molecular-beam epitaxy. *Applied Physics Letters*, **87**(11):112106, 2005.

[61] Arpana Agrawal, Tanveer Ahmad Dar, D. M. Phase, and Pratima Sen. Type I and type II band alignments in ZnO/MgZnO bilayer films. *Applied Physics Letters*, **105**(8):081603, 2014.

[62] H Tampo, H Shibata, K Maejima, T-W Chiu, H Itoh, A Yamada, K Matsubara, P Fons, Y Chiba, and T Wakamatsu. Band profiles of ZnMgO/ZnO heterostructures confirmed by kelvin probe force microscopy. *Applied Physics Letters*, **94**(24):242107, 2009.

[63] Jiandong Ye, Sze Ter Lim, Michel Bosman, Shulin Gu, Youdou Zheng, Hark Hoe Tan, Chennupati Jagadish, Xiaowei Sun, and Kie Leong Teo. Spin-polarized wide electron slabs in functionally graded polar oxide heterostructures. *Scientific reports*, **2**:533, 2012.

[64] Harold Y Hwang, Yoh Iwasa, Masashi Kawasaki, Bernhard Keimer, Naoto Nagaosa, and Yoshinori Tokura. Emergent phenomena at oxide interfaces. *Nature materials*, 11(2):103–113, 2012.

[65] Debdeep Jena, Sten Heikman, Daniel Green, Dario Buttari, Robert Coffie, Huili Xing, Stacia Keller, Steve DenBaars, James S. Speck, Umesh K. Mishra, and Ioulia Smorchkova. Realization of wide electron slabs by polarization bulk doping in graded III-V nitride semiconductor alloys. *Applied Physics Letters*, **81**(23):4395–4397, 2002.

[66] Jainendra K Jain and RK Kamilla. *Composite fermions*, volume **1**. Cambridge University Press Cambridge, 2007.

[67] J. M. Ziman. *Principles of the Theory of Solids*. Cambridge University Press, second edition, 1972. Cambridge Books Online.

[68] Ning Tang, Bo Shen, Chunmin Tao, Dunjun Chen, Yongsheng Gui, Chunping Jiang, Zhijun Qiu, Rong Zhang, Youdou Zheng, Shaoling Gu, and Junhao Chu. Magne-

tointersubband scattering oscillations of two-dimensional electron gas in alxga1-xn/gan heterostructures. In *Junction Technology, 2004. IWJT '04. The Fourth International Workshop on*, pages 198–201, 2004.

[69] D. C. Tsui, H. L. Stormer, and A. C. Gossard. Two-dimensional magnetotransport in the extreme quantum limit. *Phys. Rev. Lett.*, **48**:1559–1562, May 1982.

[70] R. B. Laughlin. Anomalous quantum Hall effect: An incompressible quantum fluid with fractionally charged excitations. *Phys. Rev. Lett.*, **50**:1395–1398, May 1983.

[71] H Kamerlingh Onnes. Further experiments with liquid helium. In *Proceedings of the KNAW*, volume **13**, pages 1910–1911, 1911.

[72] W. Meissner and R. Ochsenfeld. Ein neuer Effekt bei Eintritt der Supraleitfähigkeit. *Naturwissenschaften*, **21**(44):787–788, 1933.

[73] Francis B Silsbee. Note on electrical conduction in metals at low temperatures. *Journal of the Franklin Institute*, **184**(1):111, 1917.

[74] J. Bardeen, L. N. Cooper, and J. R. Schrieffer. Microscopic theory of superconductivity. *Phys. Rev.*, **106**:162–164, Apr 1957.

[75] Leon N. Cooper. Bound electron pairs in a degenerate Fermi gas. *Phys. Rev.*, **104**:1189–1190, Nov 1956.

[76] V. L. Ginzburg and L. D. Landau. On the Theory of superconductivity. *Zh. Eksp. Teor. Fiz.*, **20**:1064–1082, 1950.

[77] B.D. Josephson. Possible new effects in superconductive tunnelling. *Physics Letters*, **1**(7):251 – 253, 1962.

[78] P. W. Anderson and J. M. Rowell. Probable observation of the Josephson superconducting tunneling effect. *Phys. Rev. Lett.*, **10**:230–232, Mar 1963.

[79] R. C. Jaklevic, John Lambe, A. H. Silver, and J. E. Mercereau. Quantum interference effects in Josephson tunneling. *Phys. Rev. Lett.*, **12**:159–160, Feb 1964.

[80] Paul B Welander, Vladimir Bolkhovsky, Terence J Weir, Mark A Gouker, and William D Oliver. Shadow evaporation of epitaxial $Al/Al_2O_3/Al$ tunnel junctions on sapphire utilizing an inorganic bilayer mask. *arXiv preprint arXiv:1203.6007*, 2012.

[81] A. A. Istratov, C. Flink, H. Hieslmair, T. Heiser, and E. R. Weber. Influence of interstitial copper on diffusion length and lifetime of minority carriers in p-type silicon. *Applied Physics Letters*, **71**:2121–2123, 1997.

[82] M. B. Ketchen, D. Pearson, A. W. Kleinsasser, C.-K. Hu, M. Smyth, J. Logan, K. Stawiasz, E. Baran, M. Jaso, and T. Ross. Sub-micron, planarized, Nb-AlO_x-Nb Josephson process for 125 mm wafers developed in partnership with Si technology. *Applied Physics Letters*, **59**:2609–2611, 1991.

[83] S. Oh, K. Cicak, J. S. Kline, M. A. Sillanpää, K. D. Osborn, J. D. Whittaker, R. W. Simmonds, and D. P. Pappas. Elimination of two level fluctuators in superconducting quantum bits by an epitaxial tunnel barrier. *Physical Review B*, **74**(10):100502, 2006.

[84] Shin'ichi Morohashi and Shinya Hasuo. Experimental investigations and analysis for highquality Nb/AlAlO_x/ Nb Josephson junctions. *Journal of Applied Physics*, **61**(10):4835–4849, 1987.

[85] H. Kroger, L. N. Smith, and D. W. Jillie. Selective niobium anodization process for fabricating Josephson tunnel junctions. *Applied Physics Letters*, **39**(3):280–282, 1981.

[86] H. Kroger, L. Smith, D. Jillie, and J. Thaxter. Improved Nb-Si-Nb SNAP devices. *IEEE Transactions on Magnetics*, **19**(3):783–786, May 1983.

[87] M. Gurvitch, M. Washington, H. Huggins, and J. Rowell. Preparation and properties of Nb Josephson junctions with thin Al layers. *IEEE Transactions on Magnetics*, **19**(3):791–794, May 1983.

[88] Shin'ichi Morohashi, Fujitoshi Shinoki, Akira Shoji, Masahiro Aoyagi, and Hisao Hayakawa. High quality Nb/AlAlO_x/Nb Josephson junction. *Applied Physics Letters*, **46**(12):1179–1181, 1985.

[89] Shoji Iguchi, Soichi Kikkawa, Kentaro Teramura, Saburo Hosokawa, and Tsunehiro Tanaka. Investigation of the electrochemical and photoelectrochemical properties of Ni–Al LDH photocatalysts. *Physical Chemistry Chemical Physics*, **18**(20):13811–13819, 2016.

[90] SS Hullavarad, NV Hullavarad, DE Pugel, S Dhar, I Takeuchi, T Venkatesan, and RD Vispute. Homo-and hetero-epitaxial growth of hexagonal and cubic Mg_xZn_{1-x} O alloy thin films by pulsed laser deposition technique. *Journal of Physics D: Applied Physics*, **40**(16):4887, 2007.

[91] Hiroyuki Kato, Michihiro Sano, Kazuhiro Miyamoto, and Takafumi Yao. High-quality ZnO epilayers grown on Zn-face ZnO substrates by plasma-assisted molecular beam epitaxy. *Journal of Crystal Growth*, **265**(34):375 – 381, 2004.

[92] Kazuto Koike, Kenji Hama, Ippei Nakashima, Gen-you Takada, Masashi Ozaki, Ken-ichi Ogata, Shigehiko Sasa, Masataka Inoue, and Mitsuaki Yano. Piezoelectric carrier confinement by lattice mismatch at $ZnO/Zn_{0.6}Mg_{0.4}O$ heterointerface. *Japanese journal of applied physics*, **43**(10B):L1372, 2004.

[93] Hadis Morkoç and Ümit Özgür. *Zinc oxide: fundamentals, materials and device technology*. John Wiley & Sons, 2008.

[94] Fan Ren, GM Kale, A Waag, LC Chen, SP Lau, and ZL Wang. ZnO based thin films, nano-wires, and nano-belts for photonic and electronic devices and sensors. *The Electrochemical Society*, **16**, 2008.

[95] M. W. Allen, C. H. Swartz, T. H. Myers, T. D. Veal, C. F. McConville, and S. M. Durbin. Bulk transport measurements in ZnO: The effect of surface electron layers. *Phys. Rev. B*, **81**:075211, 2010.

[96] Claudine Noguera and Jacek Goniakowski. Polarity in oxide ultrathin films. *Journal of Physics: Condensed Matter*, **20**(26):264003, 2008.

[97] B. Meyer and Dominik Marx. Density-functional study of the structure and stability of ZnO surfaces. *Phys. Rev. B*, **67**:035403, Jan 2003.

[98] Raymond T. Tung. Recent advances in Schottky barrier concepts. *Materials Science and Engineering: R: Reports*, **35**(13):1 – 138, 2001.

[99] J.S. Song, Y.C. Choi, S.H. Seo, D.C. Oh, M.W. Cho, T. Yao, and M.H. Oh. Wet chemical cleaning process of GaAs substrate for ready-to-use. *Journal of Crystal Growth*, **264**(13):98 – 103, 2004.

[100] H. Angermann, J. Rappich, L. Korte, I. Sieber, E. Conrad, M. Schmidt, K. Hübener, J. Polte, and J. Hauschild. Wet-chemical passivation of atomically flat and structured silicon substrates for solar cell application. *Applied Surface Science*, **254**(12):3615 – 3625, 2008.

[101] Masashi Kawasaki, Kazuhiro Takahashi, Tatsuro Maeda, Ryuta Tsuchiya, et al. Atomic control of the $SrTiO_3$ crystal surface. *Science*, **266**(5190):1540, 1994.

[102] J T Yates Jr. Surface chemistry of silicon-the behaviour of dangling bonds. *Journal of Physics: Condensed Matter*, **3**(S):S143, 1991.

[103] Changle Wu, Xueliang Qiao, Jianguo Chen, Hongshui Wang, Fatang Tan, and Shitao Li. A novel chemical route to prepare ZnO nanoparticles. *Materials Letters*, **60**(15):1828 – 1832, 2006.

[104] M. Itano, T. Kezuka, M. Ishii, T. Unemoto, M. Kubo, and T. Ohmi. Minimization of particle contamination during wet processing of Si wafers. *Journal of The Electrochemical Society*, **142**(3):971–978, 1995.

[105] Shunsuke Akasaka, Ken Nakahara, Hiroyuki Yuji, Atsushi Tsukazaki, Akira Ohtomo, and Masashi Kawasaki. Preparation of an epitaxy-ready surface of a ZnO(0001) substrate. *Applied Physics Express*, **4**(3):035701, 2011.

[106] M W Cho, A Setiawan, H J Ko, S K Hong, and T Yao. ZnO epitaxial layers grown on c-sapphire substrate with MgO buffer by plasma-assisted molecular beam epitaxy (P-MBE). *Semiconductor Science and Technology*, **20**(4):S13, 2005.

[107] O.F. Schirmer and D. Zwingel. The yellow luminescence of zinc oxide. *Solid State Communications*, **8**(19):1559 – 1563, 1970.

[108] ED Kolb and RA Laudise. Hydrothermally grown ZnO crystals of low and intermediate resistivity. *Journal of the American Ceramic Society*, **49**(6):302–305, 1966.

[109] M.A. Reshchikov, H. Morko, B. Nemeth, J. Nause, J. Xie, B. Hertog, and A. Osinsky. Luminescence properties of defects in ZnO. *Physica B: Condensed Matter*, **401**:358 – 361, 2007.

[110] M.A. Reshchikov, V. Avrutin, N. Izyumskaya, R. Shimada, and H. Morko. Anomalous shifts of blue and yellow luminescence bands in MBE-grown ZnO films. *Physica B: Condensed Matter*, **401**:374 – 377, 2007.

[111] R. Dingle. Luminescent transitions associated with divalent copper impurities and the green emission from semiconducting zinc oxide. *Phys. Rev. Lett.*, **23**:579–581, Sep 1969.

[112] A. Ohtomo, M. Kawasaki, T. Koida, K. Masubuchi, H. Koinuma, Y. Sakurai, Y. Yoshida, T. Yasuda, and Y. Segawa. $Mg_xZn_{1x}O$ as a II-VI widegap semiconductor alloy. *Applied Physics Letters*, **72**(19):2466–2468, 1998.

[113] Y. Yao and T. Xie. *The Handbook of Physics and Chemistry*, volume 111. CRC Press,Boca Raton, FL,, 1985.

[114] M. J. Manfra, K. W. Baldwin, A. M. Sergent, R. J. Molnar, and J. Caissie. Electron mobility in very low density GaNAlGaNGaN heterostructures. *Applied Physics Letters*, **85**(10):1722–1724, 2004.

[115] Yuji Matsumoto, Makoto Murakami, Zhengwu Jin, Akira Ohtomo, Mikk Lippmaa, M. Kawasaki, and Hideomi Koinuma. Combinatorial laser molecular beam epitaxy

(MBE) growth of Mg–Zn–O alloy for band gap engineering. *Japanese Journal of Applied Physics*, **38**(Part 2, No. 6A/B):L603–L605, 1999.

[116] P. Bhattacharya, Rasmi R. Das, and Ram S. Katiyar. Comparative study of Mg doped ZnO and multilayer ZnO/MgO thin films. *Thin Solid Films*, **447**:564 – 567, 2004.

[117] W. I. Park, Gyu-Chul Yi, and H. M. Jang. Metalorganic vapor-phase epitaxial growth and photoluminescent properties of $Zn_{1x}Mg_xO$ ($0 \leq x \leq 0.49$) thin films. *Applied Physics Letters*, **79**(13):2022–2024, 2001.

[118] Charles Kittel and Herbert Kroemer. *Thermal Physics*. W. H. Freeman, 1980.

[119] Debdeep Jena, Sten Heikman, Daniel Green, Dario Buttari, Robert Coffie, Huili Xing, Stacia Keller, Steve DenBaars, James S. Speck, Umesh K. Mishra, and Ioulia Smorchkova. Realization of wide electron slabs by polarization bulk doping in graded III-V nitride semiconductor alloys. *Applied Physics Letters*, **81**(23):4395–4397, 2002.

[120] M. P. Lilly, J. L. Reno, J. A. Simmons, I. B. Spielman, J. P. Eisenstein, L. N. Pfeiffer, K. W. West, E. H. Hwang, and S. Das Sarma. Resistivity of dilute 2D electrons in an undoped GaAs heterostructure. *Phys. Rev. Lett.*, **90**:056806, Feb 2003.

[121] P Wagner and R Helbig. Halleffekt und Anisotropie der Beweglichkeit der Elektronen in ZnO. *Journal of Physics and Chemistry of Solids*, **35**(3):327–335, 1974.

[122] G. L. Snider, I.H. Tan, and E. L. Hu. Electron states in mesa-etched one-dimensional quantum well wires. *Journal of Applied Physics*, **68**(6):2849–2853, 1990.

[123] IH. Tan, G. L. Snider, L. D. Chang, and E. L. Hu. A selfconsistent solution of Schrödinger-Poisson equations using a nonuniform mesh. *Journal of Applied Physics*, **68**(8):4071–4076, 1990.

[124] A. Tsukazaki, A. Ohtomo, M. Kawasaki, S. Akasaka, H. Yuji, K. Tamura, K. Nakahara, T. Tanabe, A. Kamisawa, T. Gokmen, J. Shabani, and M. Shayegan. Spin susceptibility and effective mass of two-dimensional electrons in $Mg_xZn_{1-x}O$/ZnO heterostructures. *Phys. Rev. B*, **78**:233308, Dec 2008.

[125] David Shoenberg. *Magnetic oscillations in metals*. Cambridge University Press, 2009.

[126] P Paufler and Landolt-Börnstein. Numerical data and functional relationships in science and technology. *Crystal Research and Technology*, **23**(10-11):1360–1360, 1988.

[127] H. Köhler. Non-parabolicity of the highest valence band of Bi_2Te_3 from Shubnikov-de Haas Effect. *Physica Status Solidi (b)*, **74**(2):591–600, 1976.

[128] N. Tang, B. Shen, M. J. Wang, Z. J. Yang, K. Xu, G. Y. Zhang, T. Lin, B. Zhu, W. Z. Zhou, and J. H. Chu. Effective mass of the two-dimensional electron gas and band nonparabolicity in Al_xGa_{1-x}NGaN heterostructures. *Applied Physics Letters*, **88**(17), 2006.

[129] E. D. Palik, S. Teitler, and R. F. Wallis. Free carrier cyclotron resonance, faraday rotation, and Voigt double refraction in compound semiconductors. *Journal of Applied Physics*, **32**(10):2132–2136, 1961.

[130] W. S. Baer. Faraday rotation in ZnO: Determination of the electron effective mass. *Phys. Rev.*, **154**:785–789, 1967.

[131] Kenneth J. Button, Daniel R. Cohn, Michael von Ortenbert, Benjamin Lax, E. Mollwo, and R. Helbig. Zeeman splitting of anomalous shallow bound states in ZnO. *Phys. Rev. Lett.*, **28**:1637–1639, Jun 1972.

[132] Can Wang, Qinglin Xia, Yaozhuang Nie, Mavlanjan Rahman, and Guanghua Guo. Strain engineering band gap, effective mass and anisotropic Dirac-like cone in monolayer arsenene. *AIP Advances*, **6**(3):035204, 2016.

[133] Kuo-Feng Lin, Ching-Ju Pan, and Wen-Feng Hsieh. Calculations of electronic structure and density of states in the wurtzite structure of $Zn_{1-x}Mg_xO$ alloys using sp3 semi-empirical tight-binding model. *Applied Physics A*, **94**(1):167–171, 2009.

[134] Y.-W. Tan, J. Zhu, H. L. Stormer, L. N. Pfeiffer, K. W. Baldwin, and K. W. West. Measurements of the density-dependent many-body electron mass in two dimensional GaAs/AlGaAs heterostructures. *Phys. Rev. Lett.*, **94**:016405, Jan 2005.

[135] Medini Padmanabhan, T. Gokmen, N. C. Bishop, and M. Shayegan. Effective mass suppression in dilute, spin-polarized two-dimensional electron systems. *Phys. Rev. Lett.*, **101**:026402, 2008.

[136] D. Spirito, L. Di Gaspare, G. Frucci, F. Evangelisti, A. Di Gaspare, A. Notargiacomo, E. Giovine, S. Roddaro, and F. Beltram. Magnetotransport investigation of conducting channels and spin splitting in high-density AlGaN/AlN/GaN two-dimensional electron gas. *Phys. Rev. B*, **83**:155318, Apr 2011.

[137] M. A. Paalanen, D. C. Tsui, and J. C. M. Hwang. Parabolic magnetoresistance from the interaction effect in a two-dimensional electron gas. *Phys. Rev. Lett.*, **51**:2226–2229, Dec 1983.

[138] Patrick A. Lee and T. V. Ramakrishnan. Disordered electronic systems. *Rev. Mod. Phys.*, **57**:287–337, 1985.

[139] L. Li, Y. Y. Proskuryakov, A. K. Savchenko, E. H. Linfield, and D. A. Ritchie. Magnetoresistance of a 2D electron gas caused by electron interactions in the transition from the diffusive to the ballistic regime. *Phys. Rev. Lett.*, **90**:076802, Feb 2003.

[140] Boris L Altshuler and AG Aronov. *Electron-electron interaction in disordered conductors*. Elsevier, 1985.

[141] Xiuxun Han, Yoshio Honda, Tetsuo Narita, Masahito Yamaguchi, Nobuhiko Sawaki, Tooru Tanaka, Qixin Guo, and Mitsushiro Nishio. Scattering times in the two-dimensional electron gas of Al_xGa_{1x} N/AlN/GaN heterostructures. *Journal of Physics D: Applied Physics*, **42**(4):045112, 2009.

[142] L. Hsu and W. Walukiewicz. Transport-to-quantum lifetime ratios in AlGaN/GaN heterostructures. *Applied Physics Letters*, **80**(14):2508–2510, 2002.

[143] W. Walukiewicz, P. F. Hopkins, M. Sundaram, and A. C. Gossard. Size effect in parabolic GaAs/Al_xGa_{1-x}As quantum wells. *Phys. Rev. B*, **44**:10909–10912, Nov 1991.

[144] D. C. Look and J. R. Sizelove. Dislocation scattering in GaN. *Phys. Rev. Lett.*, **82**:1237–1240, 1999.

[145] Debdeep Jena and Umesh K. Mishra. Quantum and classical scattering times due to charged dislocations in an impure electron gas. *Phys. Rev. B*, **66**:241307, Dec 2002.

[146] Debdeep Jena and Umesh K Mishra. Quantum and classical scattering times due to charged dislocations in an impure electron gas. *Physical Review B*, **66**(24):241307, 2002.

[147] Laura M. Roth and Petros N. Argyres. Chapter 6 magnetic quantum effects. In R.K. Willardson and Albert C. Beer, editors, *Semiconductors and Semimetals*, volume 1 of *Semiconductors and Semimetals*, pages 159 – 202. Elsevier, 1966.

[148] SA Varchenya, A Simanovskis, and SV Stolyarova. Adhesion of thin metallic films to non-metallic substrates. *Thin Solid Films*, **164**:147–152, 1988.

[149] Ivan Isakov, Marina Panfilova, Marion J. L. Sourribes, and Paul A. Warburton. Growth of ZnO and ZnMgO nanowires by Au-catalysed molecular-beam epitaxy. *Physica Status Solidi (c)*, **10**(10):1308–1313, 2013.

[150] W. L. McMillan. Transition temperature of strong-coupled superconductors. *Phys. Rev.*, **167**:331–344, Mar 1968.

[151] James William Rohlf. *Modern Physics from a-alpha to Z0*. Wiley-VCH, 1994.

[152] Mingliang Tian, Nitesh Kumar, Shengyong Xu, Jinguo Wang, James S. Kurtz, and M. H. W. Chan. Suppression of superconductivity in zinc nanowires by bulk superconductors. *Phys. Rev. Lett.*, **95**:076802, Aug 2005.

[153] R. Kuzel, V. Valvoda, M. Chldek, J. Musil, and J. Matous. XRD microstructural study of Zn films deposited by unbalanced magnetron sputtering. *Thin Solid Films*, **263**(2):150 – 158, 1995.

[154] Hiroyuki Kato, Kazuhiro Miyamoto, Michihiro Sano, and Takafumi Yao. Polarity control of ZnO on sapphire by varying the MgO buffer layer thickness. *Applied Physics Letters*, **84**(22):4562–4564, 2004.

[155] Christian Weigand, Johannes Tveit, Cecile Ladam, Randi Holmestad, Jostein Grepstad, and Helge Weman. Epitaxial relationships of ZnO nanostructures grown by Au-assisted pulsed laser deposition on c- and a-plane sapphire. *Journal of Crystal Growth*, **355**(1):52 – 58, 2012.

[156] Gregory Snider. *http://www3.nd.edu/ gsnider/*, accessed 2017-01-11.

[157] Oliver Bierwagen, Tommy Ive, Chris G. Van de Walle, and James S. Speck. Causes of incorrect carrier-type identification in van der Pauw-Hall measurements. *Applied Physics Letters*, **93**(24):242108, 2008.

[158] Sukit Limpijumnong, Sergey N Rashkeev, and Walter RL Lambrecht. Electronic structure and optical properties of ZnGeN. In *MRS Proceedings*, volume **537**, pages G6–11. Cambridge Univ Press, 1998.

[159] N. Ashkenov, B. N. Mbenkum, C. Bundesmann, V. Riede, M. Lorenz, D. Spemann, E. M. Kaidashev, A. Kasic, M. Schubert, M. Grundmann, G. Wagner, H. Neumann, V. Darakchieva, H. Arwin, and B. Monemar. Infrared dielectric functions and phonon modes of high-quality ZnO films. *Journal of Applied Physics*, **93**(1):126–133, 2003.

[160] H. Tampo, H. Shibata, K. Maejima, A. Yamada, K. Matsubara, P. Fons, S. Kashiwaya, S. Niki, Y. Chiba, T. Wakamatsu, and H. Kanie. Polarization-induced two-dimensional electron gases in ZnMgO/ZnO heterostructures. *Applied Physics Letters*, **93**(20):202104, 2008.

[161] A. R. Hutson. Hall effect studies of doped zinc oxide single crystals. *Phys. Rev.*, **108**:222–230, Oct 1957.

[162] D. C. Look, D. C. Reynolds, C. W. Litton, R. L. Jones, D. B. Eason, and G. Cantwell. Characterization of homoepitaxial p-type ZnO grown by molecular beam epitaxy. *Applied Physics Letters*, **81**(10):1830–1832, 2002.

[163] Christian Franz, Marcel Giar, Markus Heinemann, Michael Czerner, and Christian

Heiliger. Band structure and effective masses of $Zn_{1-x}Mg_xO$. In *MRS Proceedings*, volume **1494**, pages 57–63. Cambridge Univ Press, 2013.

[164] JD Albrecht, PP Ruden, Sukit Limpijumnong, WRL Lambrecht, and KF Brennan. High field electron transport properties of bulk ZnO. *Journal of Applied Physics*, **86**(12):6864–6867, 1999.

[165] D.C. Reynolds, D.C. Look, and B. Jogai. Optically pumped ultraviolet lasing from ZnO. *Solid State Communications*, **99**(12):873 – 875, 1996.

[166] Z. Yarar. Steady-state electron transport and low-field mobility of wurtzite bulk ZnO and $Zn_{1-x}Mg_xO$. *Journal of Electronic Materials*, **40**(4):466–472, 2011.

[167] Andrei Malashevich and David Vanderbilt. First-principles study of polarization in $Zn_{1-x}Mg_xO$. *Phys. Rev. B*, **75**:045106, Jan 2007.

[168] OM Ozkendir, H Kavak, and Y Ufuktepe. Structural and optical properties of zinc oxide thin films prepared by spray pyrolysis method. *Journal of optoelectronics and advanced materials*, **8**(1):299, 2006.

[169] E Diler, S Rioual, B Lescop, D Thierry, and B Rouvellou. Stability of ZnMgO oxide in a weak alkaline solution. *Thin Solid Films*, **520**(7):2819–2823, 2012.